

[Intentionally blank]

AN ABSTRACT OF THE DISSERTATION OF

Kyle A. Rozman for the degree of Doctor of Philosophy in Materials Science presented on October 24, 2014

Title: Characterization of High Temperature Fatigue Mechanisms in Haynes 282 Nickel Based Superalloy

Abstract approved:

Jamie J. Kruzic

Electric power needs will only grow over the next decades as more humans ascend from poverty into the middle class. Currently, the majority of electric power is generated by burning fossil fuels. To help mitigate the undesirable effects of burning fossil fuels research is being done to increase the efficiency of power produced. In order to increase the efficiency of power production, the operating temperature of steam turbines must be increased, which presents a materials challenge. Haynes 282 is a nickel based superalloy which has been proposed as a potential rotor alloy for steam turbines operating at high temperature (760°C). Other authors have previously looked at creep, oxidation, low cycle fatigue and other properties of Haynes 282; however, lacking from the literature are studies on the fatigue crack growth mechanisms in Haynes 282. This project investigated Haynes 282 from a fatigue crack growth perspective with an aim to fill this literature gap and assess the utility of Haynes 282 as a steam turbine rotor alloy.

This dissertation has specifically evaluated the fatigue crack growth rates of Haynes 282 as functions of temperature and frequency. The testing method utilized was ASTM E647, "Standard test method for measuring fatigue crack growth rates." Temperatures investigated were 550°C, 650°C and 750°C. The loading frequencies were both 25 Hz and 0.25 Hz. In general increasing the test temperature increased fatigue crack growth rate.

Thermally activated cross-slip and dislocation annihilation were the primary mechanisms responsible for the increased fatigue crack growth rate. The noted activation energy for dislocation jog migration, which is related to dislocation annihilation, was about 12.5 kJ/mol. This value fit with the measured activation energy. The post-test microstructure showed greatly reduced dislocation density at the highest temperature. Fractography of the crack growth region showed transgranular crack growth at 550°C and 650°C with signs of isolated intergranular features at 750°C.

The effect of frequency on the fatigue crack growth rates was minor at 550°C but much more significant at 650°C and 750°C. For the temperatures investigated the effect of decreasing loading frequency was to increase the fatigue crack growth rate. At high loading frequency, the isolated intergranular features were present only at stress intensities below about $11 \text{ MPa}\sqrt{\text{m}}$. At 0.25 Hz loading frequency, isolated intergranular features persisted into the high stress intensity range.

While the isolated intergranular features are of some concern, the measured activation energy was well below published creep and/or oxidation activation energies. This means the crack path did not have enough energy to sustain an intergranular crack path.

In summary, the work discussed in this dissertation investigated the fine details of fatigue crack growth of Haynes 282. This study has closed some of the existing gap in the literature regarding the fatigue crack growth rates of Haynes 282. Previous studies have shown no adverse effects during low cycle fatigue and creep for Haynes 282 at temperatures up to and including 760°C. This study has shown no adverse effects in the fatigue crack growth of Haynes 282 up to 650°C. However, some isolated indications of intergranular crack propagation within the crack growth region were observed at 750°C. These isolated regions were observed to arrest, or to revert back to, transgranular crack propagation. This mechanistic aspect, i.e., change back to transgranular crack propagation, is a promising result.

©Copyright by Kyle A. Rozman

October 24, 2014

All Rights Reserved

Characterization of High Temperature Fatigue Mechanisms in Haynes 282 Nickel Based
Superalloy

by

Kyle A. Rozman

A DISSERTATION

submitted to

Oregon State University

in partial fulfillment of
the requirements for the
degree of

Doctor of Philosophy

Presented October 24, 2014

Commencement June 2015

Doctor of Philosophy dissertation of Kyle A. Rozman presented on October 24, 2014

APPROVED:

Major Professor, representing Materials Science

Director of the Materials Science Program

Dean of the Graduate School

I understand that my dissertation will become part of the permanent collection of Oregon State University libraries. My signature below authorizes release of my dissertation to any reader upon request.

Kyle A. Rozman, Author

ACKNOWLEDGEMENTS

The author expresses sincere appreciation to Dr. Jamie Kruzic and Dr. Jeff Hawk for their support and efforts in this thesis and project.

This research was supported in part by an appointment to the U.S. Department of Energy (DOE) Postgraduate Research Program at the National Energy Technology Laboratory administered by the Oak Ridge Institute for Science and Education.

The author would like to thank the following individuals from National Energy Technology Laboratory Albany for their help in various activities. Keith Collins for technical support on the scanning electron microscope. John Sears for technical support on the transmission electron microscope.

The author would like to thank the following individuals from Oregon State University for their help in various activities. Dr. Peter Eschbach at OSU EM facility for FIB milling and TEM sample preparation. Dr. Rawley Greene for experimental support and technical programming. Dr. Bill Warnes contributions to accuracy measurements and activation energy analysis. Dr. Brady Gibbons and Dr. Frank Tepley for their contributions as committee members.

TABLE OF CONTENTS

	<u>Page</u>
1. INTRODUCTION:	1
1.1 General information about NBSAs	2
1.2 Deformation mechanisms in NBSAs	4
1.2.1 FCC deformation mechanisms	6
1.2.1.1 Energy of dislocation disassociations	10
1.2.1.2 Nonconservative dislocation motion in FCC materials	10
1.2.2 Interactions of dislocations in FCC materials	11
1.2.3 Cyclic deformation in FCC material	15
1.3 NBSA deformation	15
1.3.1 Gamma prime deformation	17
1.3.2 Cross slip of NBSAs	19
1.3.3 Dislocation annihilation	20
1.3.4 Twinning of NBSAs.....	21
1.5 Linear elastic fracture mechanics	22
1.6 Fatigue crack growth	25
1.6.1 Grain size influence on FCG in NBSAs.....	27
1.6.2 Creep influence on FCG in NBSAs	28
1.6.3 Other influences on FCG in NBSAs	30
1.7 Activation energy	31
1.7.1 Mechanisms related to activation energy	32
1.7.2 Other effects of elevated temperature on NBSAs	33
1.8 Fractography	34
1.9 Transmission electron microscopy	35

TABLE OF CONTENTS (Continued)

	<u>Page</u>
2. LITERATURE REVIEW	37
2.1 Thermal exposure effects of Haynes 282	37
2.2 Low cycle fatigue of Haynes 282	44
2.3 Creep properties of Haynes 282	47
2.4 Fatigue crack growth of Haynes 282	51
2.5 Summary of literature regarding Haynes 282.	54
3. PROBLEM STATEMENT	55
4. MATERIAL AND METHODS	56
4.1 Haynes 282	56
4.2 Experimental Methods	57
4.2.1 Experimental method	58
4.2.1.1 Sample manufacturing procedure	58
4.2.1.2 Measuring crack length.....	59
4.2.1.3 Heating procedure.....	61
4.2.1.4 Precracking procedure	61
4.2.1.5 Fatigue crack growth procedure	63
4.2.2 Fractography procedure	65
4.2.3 TEM sample procedure	65
4.3 Uncertainty in FCG rates	66
4.4 Activation energy calculation	69

TABLE OF CONTENTS (Continued)

	<u>Page</u>
4.5 Uncertainty in activation energy	70
4.6 Uncertainty in calculating the activation energy	71
4.7 Calculating experimental uncertainty	71
4.8 Total activation energy uncertainty	73
5. EXPERIMENTAL RESULTS	74
5.1 Fatigue crack growth rates	74
5.1.1 Paris fit to FCG curves	76
5.1.2 FCG of Haynes 282 relative to other NBSAs	80
5.2 Fractography results	82
5.2.1 Fracture surfaces at 25 Hz loading frequency	82
5.2.2 Fracture surfaces at 0.25 Hz loading frequency	84
5.2.3 Secondary cracking	86
5.2.4 Note on intergranular features.....	87
5.3 Microstructure results	88
5.3.1 Initial peak aged microstructure	88
5.3.2 Observed active mechanisms	89
5.3.3 Microstructure of the plastic zones	90
5.3.4 Dark field microcopy of gamma prime	92
5.4 Activation energy	93
5.4.1 Activation energy of other NBSAs	95
5.4.2 Uncertainty in activation energy	96

TABLE OF CONTENTS (Continued)

	<u>Page</u>
6. DISCUSSION:	99
6.1 FCG of Haynes 282 from other authors	99
6.2 Verification of activation energy	103
6.3 Discussion of temperature effect on FCG curves	105
6.3.1 Effect of mechanical properties on FCG curves	105
6.3.2 The effect of environment effects on FCG.....	107
6.3.3 The effect of microstructural phases at high temperature	108
6.3.4 Temperature dependent shear	108
6.3.5 Temperature dependent dislocation cross slip and annihilation.....	110
6.3.6 Summary of temperature effects on FCG	111
6.4 Discussion of Frequency effects on FCG rates	112
6.4.1 The effect of creep on FCG rates	113
6.4.2 Steady state diffusion creep	115
6.4.3 Strain rate sensitivity in NBSAs	115
6.4.4 Summary of time dependence on FCG rates.....	119
6.5 Cracking mechanism transition	119
6.5.1 Duplex slip transition.....	120
6.5.2 Looping transition.....	121
7. CONCLUSION	125
APPENDIX I: SAMPLE PARAMETERS	130

TABLE OF CONTENTS (Continued)

Page

APPENDIX II: FRACTURE SURFACES AT 0.05 HZ LOADING FREQUENCY
..... **133**

LIST OF FIGURES

	<u>Page</u>
Figure 1 - Illustration of the geometry for the Schmid factor. Note, $\lambda + \phi \neq 90^\circ$. Reprinted from Hull, Bacon [13] with permission of Elsevier publishing.	5
Figure 2 - Schematic of the unit cell, highlighting the (111) plane in blue, and $\langle 110 \rangle$ directions in red.	6
Figure 3 – Schematic of a perfect edge and screw dislocations, a) Edge dislocation, b) screw dislocation. Reprinted from Hull, Bacon [13] with permission of Elsevier publishing.....	7
Figure 4 – Schematic of screw dislocation cross slip, a-c), progressive slip from (111) to 111 planes, d) Double cross slip back to the (111) plane. Reprinted from Hull, Bacon [13] with permission of Elsevier publishing.	7
Figure 5 - Potential atomic paths for dislocation motion on {111} planes. Reprinted from Hull, Bacon [13] with permission of Elsevier publishing.....	8
Figure 6 – Illustration of a stacking fault left between slip of Shockley partial dislocations (b_3 and b_2). from Hull, Bacon [13] with permission of Elsevier publishing.	9
Figure 7 – Illustration of climb process for edge dislocations, a) positive climb, b) original dislocation, c) negative climb. Reprinted from Hull, Bacon [13] with permission of Elsevier publishing.	11
Figure 8 – Arrangements of edge dislocations, a) like dislocations on the same plane, b) unlike dislocations on the same plane, c) unlike dislocations separated by a few planes. Reprinted from Hull, Bacon [13] with permission of Elsevier publishing.	12

LIST OF FIGURES (Continued)

	<u>Page</u>
Figure 9 – Schematic of Lomer-Cottrell lock, a) perfect dislocations, b) disassociation into Schockley partial dislocations, c) partial dislocations combine forming Lomer-Cottrell lock. Reprinted from Hull, Bacon [13] with permission of Elsevier publishing.	13
Figure 10 – Schematic of jogs in screw dislocations, a) two screw dislocations, b) two screw dislocations after they have passed each other, c) illustration of jog locking mechanism in screw dislocations. Reprinted from Hull, Bacon [13] with permission of Elsevier publishing.....	14
Figure 11 - Progression of Frank Reed dislocation multiplication source. a) locked dislocation between two obstacles b-d) bowing of dislocation back onto its self, e) dislocation loop formed and process repeats itself.	14
Figure 12 - Cyclic stress strain response for ductile single crystals. a) dislocation vein structure, composed of edge dipoles [25], b) persistent slip band structure, featuring the ladder and rung structure [25], c) labyrinth structure [26]. Reprinted with permission of Elsevier publishing [25] [26].	15
Figure 13 - Schematic of Orowan bypass mechanism (a-c) and cutting of precipitates (d-e), a) dislocation encounters precipitate, b) dislocation bows around precipitate, c) dislocation loops around precipitate, and breaks free, leaving a loop around the precipitate and a free dislocation, d) dislocation encounters a precipitate, e) dislocation shears precipitate, leaving a complex stacking fault.....	16
Figure 14 - Schematic of dislocation climb, a) dislocation encounters precipitate, b) dislocation climbs out of glide plane to bypass precipitate.....	17

LIST OF FIGURES (Continued)

	<u>Page</u>
Figure 15 - Schematic of L12 γ' structure, a) unit cell, b) super dislocation, c) super partial dislocation.....	18
Figure 16 - schematic of the Kear-Wiltsdorf lock. Reprinted from Hull, Bacon [13] with permission of Elsevier publishing.....	19
Figure 17 - Escaig model for cross slip, a) constriction of partial dislocations, b) cross slip on new plane, c) expansion of cross slip.....	20
Figure 18 - Schematic of dislocation annihilation by jog migration by Hirsch [42]	21
Figure 19 - Schematic of twin boundary.....	22
Figure 20 - Diagram showing the different modes of cracking in plane stress.....	24
Figure 21 - Diagram of the three phases of crack growth. Region 1 is the treshold region, Region to is the Paris region, and Region 3 is final fracture.....	26
Figure 22 - Micro-mechanisms of fatigue crack growth a) stage one crack growth, b) stage 2 crack growth, c) blunting and resharpening mechanism.	27
Figure 24 - Schematic of the influence of creep and LEFM plastic zone on FCG.	30
Figure 25 - Schematic illustrating activation energy, reprinted from [13].....	31
Figure 26 - Schematic illustrating temperature dependence of activation energy. Green dashed line represents a low a energy process activated at low temperature, where red solid line illustrates a higher energy process activated at a higher temperature. Blue dotted line illustrates a combination of both processes.....	32

LIST OF FIGURES (Continued)

	<u>Page</u>
Figure 27 - Images of a) fatigue striations, b) river marks, c) grain boundary cavitation.	35
Figure 28 - ThermoCalc phase diagram for Haynes 282 showing ideal mole fractions of γ , γ' , σ , μ [104]. For reference 750°F = 400°C, 1250°F = 677°C and 1750°F = 954°C	38
Figure 29 - Initial microstructures for Haynes 282, a) solution annealed (as received) showing small γ' precipitates approximately 10-20nm in diameter, b) peak aged showing γ' precipitates approximately 50 nm in diameter, c) over aged showing γ' precipitates slightly larger than 50 nm in diameter [104].....	39
Figure 30 - Yield stress of Haynes 282 in various heat treatments [104].	40
Figure 31 –Yield stress/elongation with respect to temperature of various NBSAs after 1000 hr of exposure, A) elongation, B) yield strength. Reprinted with permission of The Minerals, Metals & Materials Society [101].....	41
Figure 32 – Yield strength/elongation of Haynes 282 with respect to time, A) elongation, B) Yield strength. Reprinted with permission of The Minerals, Metals & Materials Society [101].....	43
Figure 33 – LCF of H282 from 871°C to 649°C [102].	45
Figure 34 – LCF of various NBSAs and their stress response at 816°C [102].	46
Figure 35 - Low cycle fatigue of Haynes 282 in various heat treatments at 760°C. Specimens were tested at Haynes international, Siemens and the National Energy Technology Laboratory [104].	47

LIST OF FIGURES (Continued)

	<u>Page</u>
Figure 36 – TEM results of crept samples. a) Short-term creep rupture tests showing partial shearing as deformation mechanism, b) Long-term creep rupture tests, showing particle bypass as the deformation mechanism [104].	49
Figure 37 - Larson-Miller curve for Haynes 282 showing data from Siemens, GE, and Hawk [104]. Note 100 MPa = 14.5 KSI.	50
Figure 38 – Larson-Miller curve for various NBSAs considered for rotor applications [104]. Note 100 MPa = 14.5 KSI.	51
Figure 39 - FCG rates of H282 found by Buckson and Ojo at 15 hz Reprinted with permission of Elsevier publishing [100].	53
Figure 40 - FCG rates of H282 found by Buckson and Ojo at 0.05 hz Reprinted with permission of Elsevier publishing [100].	53
Figure 41– Microstructure of Haynes 282 in peak aged state with ASTM grain size 4. Inset: TEM image of gamma prime also in peak age state, from deformed material.	57
Figure 42 – Schematic of samples cut in the S-T direction.	59
Figure 43 - Schematic of the DCPD setup on the C(T) sample. Sample width 'B' is 6.4 mm while sample width 'W' is 25.4 mm.	60
Figure 44 – Schematic of TEM sample extraction.	66
Figure 45 - Error sources accounted for via fit method.	71

LIST OF FIGURES (Continued)

	<u>Page</u>
Figure 46 - Error sources accounted for via Taylor method, Black represents fluctuations, red represents average measurements. A) Slope error from raw data B) fluctuations in temperature, C) fluctuations in voltage effecting α (assumed to be accounted for in A)..	72
Figure 47- FCG of Haynes 282 at 25 Hz at 550°C (blue diamonds, bottom), 650°C (red diamonds, middle), and 750°C (black diamonds, top). Load ratio 0.1, waveform: sinusoidal.	75
Figure 48- FCG of Haynes 282 0.25 Hz at 550°C (blue triangle, bottom), 650°C (red triangle, middle), and 750°C (black triangle, top). Load ratio 0.1, waveform: triangular.	76
Figure 49 - FCG rates at 550°C isolated by loading frequency, with exponential trend line fit. The 0.25 Hz is upper curve and 25 Hz is lower curve.....	77
Figure 50 - FCG rates at 650°C isolated by loading frequency, with exponential trend line fit. The 0.25 Hz is upper curve and 25 Hz is lower curve.....	78
Figure 51 - FCG rates at 750°C isolated by loading frequency, with exponential trend line fit. The 0.25 Hz is upper curve and 25 Hz is lower curve.....	79
Figure 52 – FCG rates of various superalloys in temperature ranges between 650-760°C and frequencies of 2-25 Hz. WSP = Waspaloy [113], U720li = Udimet 720 low interstitial [114].....	81
Figure 53 – FCG rates of various superalloys from 650-760°C at 0.05 to 0.33 Hz. IN718 = Inconel 718 [115], U720li = Udimet 720 low interstitial[8], WSP = Waspaloy at 760°C[116], IN100 = Inconel 100 at 700°C [117].	82

LIST OF FIGURES (Continued)

	<u>Page</u>
Figure 54 - Fracture surfaces of Haynes 282 tested at 25 Hz, at various temperatures and stress intensity ranges. Crack growth direction is bottom to top for all images A-I. A transition from stage one to stage two crack growth mechanism was observed at ΔK of 14 MPa \sqrt{m} for 650°C and below. Not shown is the delayed stage one to stage two cracking mechanism shift at 750°C at ΔK of 20 MPa \sqrt{m}	84
Figure 55 - Fracture surfaces of Haynes 282 tested at 0.25 Hz, at various temperatures and stress intensity ranges. Crack growth direction is bottom to top for all images. A transition from stage one to stage two crack growth mechanism was observed at ΔK of 14 MPa \sqrt{m} for 650°C and below, while this transition happened at ΔK of 19 MPa \sqrt{m} for 750°C.	85
Figure 56 - Secondary cracking at low stress intensity ranges. A-C) secondary cracking at 25 Hz loading frequency, D-F) secondary cracking at 0.25 Hz loading frequency.	86
Figure 57 - Secondary cracking at high stress intensity ranges. A-C) secondary cracking at 25 Hz loading frequency, D-F) secondary cracking at 0.25 Hz loading frequency.	87
Figure 58 - Lower magnification fracture surface illustrating transgranular crack growth.	88
Figure 59 – Initial microstructure after peak aged heat treatment. A) showing annealing twins, B) Showing individual dislocations and carbides, C) showing carbides along a boundary. [118].....	89

LIST OF FIGURES (Continued)

	<u>Page</u>
Figure 60 – Observed deformation mechanisms active in Haynes 282. A) shearing of gamma prime, B) Persistent slip bands, C) Orowan looping mechanism, D) shearing of gamma prime by partial dislocations.	90
Figure 61 – TEM images of samples selected in front of the crack tip, parallel to the crack. A, B,C Specimen cracked at ΔK of $9 \text{ MPa}\sqrt{\text{m}}$ at 25 Hz. D, E, F Specimen cracked at ΔK of $15 \text{ MPa}\sqrt{\text{m}}$ at 0.25 Hz.	91
Figure 62 - Dark field microscopy of gamma prime. A) at 650°C with 0.25 Hz waveform at of ΔK of $15 \text{ MPa}\sqrt{\text{m}}$ B) at 750°C with 0.25 Hz waveform at of ΔK of $9 \text{ MPa}\sqrt{\text{m}}$	92
Figure 63 - Activation energy of Haynes 282. Blue diamonds are activation energy in kJ/mol for 25 Hz, while red triangles is for 0.25 Hz. Error bars indicate uncertainty. Statistical analysis of the trendline at 25 Hz shows $P = 0.0004$ and at 0.25 Hz, $P = 0.0001$	94
Figure 64 - Activation energy of various NBSA. Vac = vacuum, 0.25 Hz = 0.25 Hz loading frequency with triangular waveform, 20 sec = trapezoidal waveform with 20 second hold time. Sources as follows: Udimet 720li [119][120], RR1000 [121], N18 [122][123]	96
Figure 65 - FCG data of Buckson and Ojo [100] against the author's at high frequency.	100
Figure 66 - Microstructure of Haynes 282, images resized to equal scales. A) reported by Buckson and Ojo[100], B) reported by the author.....	102

LIST OF FIGURES (Continued)

	<u>Page</u>
Figure 67 - FCG data of Buckson and Ojo [100] against the author's data at low frequency. The author used a triangular waveform, while Buckson and Ojo used a sinusoidal.	103
Figure 68 - Normalized FCG rates by activation energy of 25 kJ/mol for 25 Hz (lower group) and 35 kJ/mol for 0.25 Hz (upper group).	104
Figure 69 - FCG of Haynes 282 normalized by yield strength and Young's modulus changes with temperature.	106
Figure 70 - Schematic of visco-plastic creep damage zone. A) small creep zone at high frequency, B) larger creep zone at lower frequency, C) creep zone exceeds plastic zone with a time delay.	114
Figure 71 - Hayes and Hayes's proposed model for serrated flow, A) Dislocation glides as normal, B) Dislocation has picked up carbon, C) Dislocation bows around gamma prime, D) Carbon pipe diffuses and is captured by gamma prime, E) Dislocation bypasses gamma prime by Orowan mechanism, leaving carbon at gamma prime and dislocation is free to glide as normal.	117
Figure 72 - Dislocation shear bands at from the microstructure at 750°C, 25 Hz. A) showing a typical shear band, B) zoomed in from Figure 61F, p93. Potential partial dislocation pair in question is circled.	122
Figure 73- Fracture surfaces at 0.05 Hz with triangular waveform, R=0.1. Approximate stress intensity levels.	134

LIST OF TABLES

	<u>Page</u>
Table 1 - Common roles of alloying elements in NBSAs.....	2
Table 2 – Chemical composition for various NBSAs, Reprinted with permission of The Minerals, Metals & Materials Society [101].....	37
Table 3 - Heat treatment schedule for peak aging of various NBSAs [102]. AC = Air cool, RAC = Rapid air cool via fan.....	41
Table 4 – Mechanical properties of various NBSAs in peak aged state [102].....	42
Table 5 – Oxidation depth for various NBSAs [103].	44
Table 6 - composition of Haynes 282 [4].	56
Table 7 - Mechanical properties of Haynes 282 over 540°C to 750°C from[4].....	57
Table 9 - Paris constants at 0.25 Hz for each tested temperature.	80
Table 10 - Paris constants at 25 Hz for each tested temperature. Paris constants for 650°C and 750°C split at $\Delta K = 17 \text{ MPa}\sqrt{\text{m}}$	80
Table 11 - Activation energy and uncertainty for 25 Hz.	97
Table 12 - Activation energy and uncertainty for 0.25 Hz.	98
Table 13 - Oxidation depth in Haynes 282 as reported from Pike [4].	107
Table 14 - Strain rates for various levels of strain estimated in the C(T) sample.	118
Table 15 - Parameters for sample 24, measured at 750°C and 0.25 Hz.	130

LIST OF TABLES (Continued)

	<u>Page</u>
Table 16 - Parameters for sample 20, measured at 750°C and 25 Hz.	130
Table 17 - Parameters for sample 13, measured at 650°C and 0.25 Hz.	131
Table 18 - Parameters for sample 11, measured at 650°C and 0.25 Hz.	131
Table 19 - Parameters for sample 11, measured at 650°C and 25 Hz.	131
Table 20 - Parameters for sample 14, measured at 550°C and 0.25 Hz.	132
Table 21 - Parameters for sample 12, measured at 550°C and 25 Hz.	132

LIST OF EQUATIONS

	<u>Page</u>
Equation 1 - Typical carbide formation reaction.	4
Equation 2 - Schmid factor relation. Where: ' τ_{CRSS} ' is the resolved shear stress, ' σ ' is the applied stress, ' ϕ ' is the angle between the slip plane normal and applied stress, ' λ ' is the angle between the slip direction and the applied stress.....	6
Equation 3 - Shockley partial equation.....	9
Equation 4 - Formula to calculate the equilibrium spacing of partial dislocations. Where ' d_{SP} ' is the equilibrium spacing between Shockley partials, ' G ' is the shear modulus, ' b ' is the Burger's vector, ' γ_{SFE} ' is the stacking fault energy.....	9
Equation 5 – Computation of Franks rule for perfect and partial dislocations.	10
Equation 6 - Lomer-Cottrell locking mechanism	13
Equation 7 - Formula for stress intensity - Where: ' K_I ' is the mode I stress intensity, ' Y ' is the dimensionless constant dependent on loading mode and geometry, ' σ ' is the applied stress, ' a ' is the applied crack length.	23
Equation 8 - Stress ahead of crack tip. Where: ' r ' is the distance from the crack tip	24
Equation 9 - Plastic zone size formula. Where: ' r_p ' is the plastic zone size, ' K_I ' is the mode one stress intensity, ' σ_y ' is the yield strength of the material.....	25
Equation 10 - Where: ' da/dN ' is the crack growth rate per cycle, ' C_p ' is the Paris constant, ' m ' is the Paris exponent, ' ΔK ' is the stress intensity range	26

LIST OF EQUATIONS (Continued)

	<u>Page</u>
Equation 11 - Larson-Miller parameter equation. Where: 'LMP' is the Larson-Miller parameter, 'T' is the temperature in Kelvin, 'C _{imp} ' is a constant in the range of 20-22, 't' is the time in hours.	50
Equation 12 – Voltage to α relations. A) Voltage to alpha relation B) Alpha to voltage relation. Where: ' α ' is the instantaneous crack length divided by W, the sample width and 'V' is the instantaneous voltage, in milivolts.	61
Equation 13 - Stress intensity calculation as a function of α . Where, 'P' is the load, 'B' is the C(T) sample thickness, 'W' is the C(T) sample width, ' α ' is the instantaneous crack length divided by W.....	61
Equation 14 - Formula for load shedding constant calculation. Where: 'C' is the load shedding constant, 'K _i ' is the initial stress intensity, 'dK' is the change in stress intensity, 'da' is the change in crack length.....	62
Equation 15 - Crack length correction equation. Where: ' $a_{initial}$ ' is the initial crack length measured by microscope, ' $b_{instant}$ ' is the instantaneous crack length measured by the computer, ' $b_{initial}$ ' is the initial crack length measured by computer, ' a_{final} ' is the final crack length measured by microscope, ' b_{final} ' is the final crack length measured by computer. .	65
Equation 16 – Activation energy relation. Where: 'da/dN' is the rate of transformation, 'kf(a)' is a function containing all terms independent of 'T', 'Q' is the activation energy, 'R _g ' is the gas constant and 'T' is the temperature.	69
Equation 17 - Linearization of Equation 16.....	69
Equation 18 – Uncertainty in a function of several variables as found by Taylor [111]. .	72

LIST OF EQUATIONS (Continued)

	<u>Page</u>
Equation 19 - Equation 17 solved for Q	72
Equation 20 – Partial derivative of activation energy with respect to temperature.	73
Equation 21 - Partial derivative of activation energy with respect to crack growth rate. .	73
Equation 22 - Equation used to sum uncertainty. Where: ' ΔQ_{tot} ' is the total uncertainty, ' ΔQ_{Taylor} ' is the experimental uncertainty, and ' ΔQ_{fit} ' is the uncertainty in the fit to the activation energy calculation.	73
Equation 23 - Normalization factor applied to the FCG rates.	103
Equation 24 – Mechanical normalization factor. Where: ' ΔK ' is the stress intensity range, ' σ_y ' is the yield stress, 'E' is Young's modulus.....	105

LIST OF ACRONYMS

AUSC - Advanced Ultra Supercritical steam turbine

FCG - fatigue crack growth

C(T) - Compact tension specimen

SEM - scanning electron microscope

TEM - Transmission electron microscopy

NBSA -Nickel based super alloy

FCC - face centered cubic materials

FIB – focused ion beam

BCT - body centered tetragonal

TCP - tetragonal close packed

LCF - low cycle fatigue

LEFM - linear elastic fracture mechanics

DCPD - Direct current potential difference

LMP - Larson-Miller parameter

LIST OF SYMBOLS

b - Burger's vector

a - lattice parameter

d_{sp} - equilibrium spacing between partial dislocations

E - Young's modulus

G - shear modulus

γ_{SFE} - stacking fault energy

τ_{CRSS} - critical resolved shear stress

σ - stress

σ_y - yield stress

ϕ - angle between applied force and slip plane normal vector

λ - angle between applied force and slip vector

K - stress intensity

K_I - mode 1 stress intensity

r - radial distance from crack tip

r_p - plastic zone radius

da/dN - crack growth rate

P - applied load

Y - geometric factor

C_p - Paris constant

LIST OF SYMBOLS (Continued)

m - Paris exponent

T - temperature

C_{LMP} - Larson-Miller parameter constant

t - time

α - ratio of crack length to sample width

V - voltage

B - sample height

W - sample width

$k_f(a)$ - term independent of temperature

Q - activation energy

R_g - universal gas constant

N - Zener-Holoman factor

C_{LS} - load shedding constant

R - load ratio

b_{instant} - instantaneous crack length measured by the computer

a_{final} - final crack length measured by microscope

a_{initial} - initial crack length measured by microscope

b_{final} - final crack length measured by computer

b_{initial} - initial crack length measured by computer

LIST OF SYMBOLS (Continued)

C - constant

1. Introduction:

The majority of worldwide electricity generation involves boiling water to turn steam turbines. State-of-the-art ultra-super critical steam turbines are forced to operate below 675°C due to material constraints [1]. Nickel based superalloys (NBSAs) are being investigated in order to raise inlet pressure and temperatures of super critical steam turbines. The National Energy Technology Laboratory is in an industry-government partnership to develop the next generation advanced ultra-supercritical steam turbine (AUSC). The goal is for AUSC steam turbines to operate at 760°C and 35 MPa and increase efficiencies to 50%, up from 37% efficiency for the ultra-supercritical plants of 2014 [2]. If successful, this effort will reduce carbon dioxide emissions on a per kilowatt hour basis.

NBSAs are a high temperature class of alloys strengthened by precipitation or solid solution. With steam turbine rotor design requirements of 400 MPa yield strength and 100 MPa creep rupture strength at 100,000 hours, both at 760°C [3], solid solution nickel alloys do not meet the yield strength requirement for rotor applications. Thus, precipitation strengthened alloys strengthened by Ni₃Al gamma prime (γ') precipitates are under primary consideration.

Haynes 282 offers a unique chemistry enabling high yield strength and creep resistance with a lower volume fraction of γ' (~30%) relative to high volume fraction alloys such as Rene 41 (~80%). The lower volume fraction of γ' enables good fabricability, ductility and strain age cracking resistance. Fabrication, ductility and strain age cracking are known problems in other NBSAs alloys such as Rene-41 and Waspaloy [4]. Strain age cracking is a problem in NBSAs where the post welding heat treatment causes cracks.

Welds on NBSAs are done with a different NBSA than the base alloy. After the weld is completed a stress relieving heat treat is applied to precipitate and grow gamma prime. For high volume fraction gamma prime alloys such as Rene-41 there is nowhere for the gamma prime precipitates to grow. Subsequently, the growth of new gamma prime

causes internal stresses on the magnitude of the ultimate tensile stress, leading to rupture/cracking.

With a design life requirement of 100,000 hours, it is critical steam turbine rotor alloys will not fatigue to cause catastrophic failure. Service conditions such as frequency, temperature and environment are known to affect fatigue crack growth (FCG) rates [5]. Different cracking mechanisms may be active under varying conditions. For example, at high temperatures thermally activated mechanisms such as creep or oxidation may be active and one may see intergranular crack growth. Similarly, at lower frequencies more time is available near the peak load promoting time dependent mechanisms. Alloys N18 [6], IN100 [7] and U720 [8] have shown a shift in cracking mechanism from transgranular to intergranular crack growth by decreasing the loading frequency in an oxidizing environment. It is important to investigate FCG at various temperatures and frequencies in order to understand where potential shifts in fatigue mechanism may have an adverse effect on lifetime.

1.1 General information about NBSAs

NBSAs are primarily nickel with chromium, aluminum, titanium, molybdenum and cobalt as the major alloying elements. Typical roles of alloying elements are presented in Table 1.

Element	Role
Al	γ' [9]
Ti	γ' , also lowers stacking fault energy in γ' [9]
Cr	Oxidation resistance [9]
Mo	Solid solution strengthening, also increases mismatch of γ/γ' [9]
C	Precipitation of carbides to reduce grain boundary sliding [9]
Ta	Solid solution strengthening [9]
Hf	Aids in stability and carbide geometry [9]
B	Assists grain boundary cohesiveness [10]
P	Assists grain boundary cohesiveness [11]

Table 1 - Common roles of alloying elements in NBSAs.

NBSAs are strengthened either by solid solution or precipitation strengthening mechanisms. Examples of solid solution strengthened alloys are Hastelloy alloys X and S. Examples of precipitation strengthened alloys are Waspalloy and Rene 41. Solid solution alloys are generally more corrosion resistant but lower in strength when compared to precipitation strengthened alloys.

Solid solution strengthened alloys primarily derive their strength from solute atoms altering the local stress field in the matrix, which impedes dislocation glide and concurrently increases the flow stress of the matrix [12]. Precipitate strengthened alloys primarily derive their strength by precipitates hindering dislocation motion and/or by multiplying dislocations via Frank Reed sources [12] [13] [14]. The major strengthening precipitate is coherent and referred to as the gamma prime (γ') phase, with the gamma (γ) phase being the base matrix of nickel solid solution. Gamma prime is a face centered cubic (FCC) based superlattice structure ($L1_2$) of the nominal chemical composition Ni_3Al and has the desirable property of increasing flow stress with increasing temperature [12] [14] [15]. The gamma prime precipitates also possess ductility and are not initiation sources for brittle fracture at high temperatures [12]. The disorder transition for pure gamma prime is $1375^\circ C$ [12] [14] which is near the melting point of most NBSA and far above service temperatures for such alloys.

Titanium and other elements may be substituted for aluminum. While gamma prime composed of Ni_3Al is thermodynamically stable, Ni_3Ti is not thermodynamically stable and will decompose over time when exposed over $650^\circ C$ [12].

Other phases observed in NBSAs are sigma (σ), eta (η), gamma double prime (γ'') and delta (δ). For alloys with high Ti:Al ratios (i.e. >3) gamma prime tends to transform to platelike hexagonal eta phase at higher temperatures. This is observed in A-286 and Incoloy 901 [16].

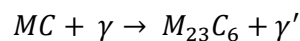
The sigma phase is a body centered tetragonal (BCT) structure of chemical morphology $(Cr,Mo)_2(Ni,Co)$ [12] [14]. Sigma phase has a platelike morphology and depletes the local gamma matrix of refractory elements. The refractory elements tend to aid in solid

solution strengthening; therefore, excessive sigma phase is undesirable. Sigma phase has been reported to be detrimental to creep rupture strength [17] [18] [19] [20] [21].

The mu phase is a rhombohedral type structure with chemical morphology $(\text{Mo, W})_6\text{Co}_7$ [12] [14]. Alloys with M_6C carbides present like Rene 41 and M-252 tend to contain mu phase. Mu phase has not been shown to be detrimental to mechanical properties in M-252 [22]. However, the depletion of refractory elements can lead to loss of solid solution strength [18].

The gamma double prime phase is a D0_{22} structure with chemical morphology of Ni_3Nb . Alloys IN718 and IN706 are strengthened by gamma prime and gamma double prime [14]. Gamma double prime has a disk shape, ~ 10 nm thick x 50 nm diameter. Overaging gamma double prime yields orthorhombic delta (δ) phase [23] [24]. Delta phase is incoherent with gamma and forms at temperatures of 650-980°C [14].

The last strengthening mechanism in NBSAs is carbides. Carbides tend to precipitate along the grain boundaries and they tend to resist grain boundary sliding and enhance the creep strength, particularly the M_{23}C_6 type carbides [14]. Carbides form from a reaction of carbon with metallic alloying elements to form M_{23}C_6 , MC, and/or M_6C type carbides [12] [14]. See Equation 1 for the typical reaction forming M_{23}C_6 type carbide. The M_{23}C_6 type carbides are known to form at or above 750°C [14].



Equation 1 - Typical carbide formation reaction.

1.2 Deformation mechanisms in NBSAs

Metals owe their ductility to dislocation motion. The Von Mises criterion states that a minimum of five independent slip systems must be present for ductile behavior. Under sufficient stress (critical resolved shear stress, τ_{CRSS}), dislocation motion occurs on slip planes. When the dislocation moves in the plane which contains both its Burger's vector and line vector, slip is referred to as 'conservative'. Nonconservative motion occurs

when the dislocation moves out of its glide surface. For dislocations to move out of their glide planes, an empty lattice site (vacancy) must diffuse to the dislocation front.

Static dislocations are 'sessile' while gliding dislocations are 'glissile'. To determine the active dislocation system consider that, the crystal orientation is random relative to the applied stress field (exceptions being manufacturing processes which induce a long range crystallographic texture). Schmid [13] developed a formula (Equation 2) to help figure out which slip system is active in a randomly oriented crystal, which is schematically drawn in Figure 1. The plane with the highest Schmid factor ($\cos \phi \cdot \sin \lambda$) will undergo slip, assuming the stress is greater than the critical resolved shear stress. Under high stress situations (such as a crack tip), multiple slip systems may be active as long as each system meets or exceeds the critical resolved shear stress.

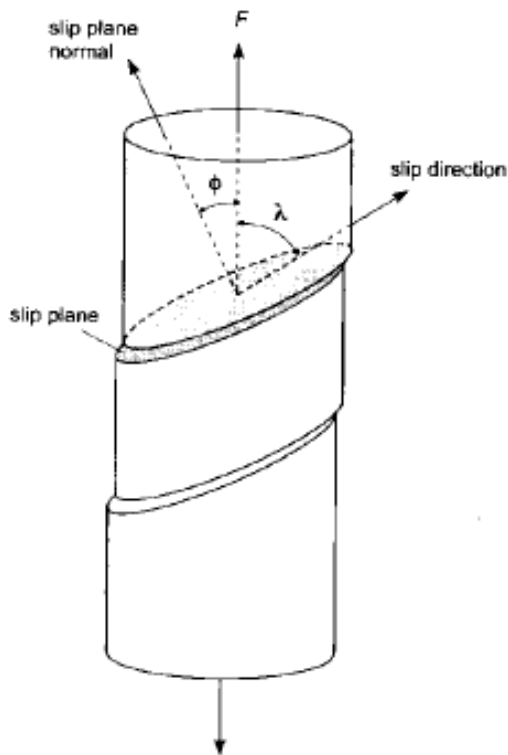


Figure 1 - Illustration of the geometry for the Schmid factor. Note, $\lambda + \phi \neq 90^\circ$. Reprinted from Hull, Bacon [13] with permission of Elsevier publishing.

$$\tau_{CRSS} = \sigma \cos \phi \sin \lambda$$

Equation 2 - Schmid factor relation. Where: ' τ_{CRSS} ' is the resolved shear stress, ' σ ' is the applied stress, ' ϕ ' is the angle between the slip plane normal and applied stress, ' λ ' is the angle between the slip direction and the applied stress.

1.2.1 FCC deformation mechanisms

For FCC materials such as NBSAs typical dislocation glide planes are $\{111\}$ with the glide directions $\langle 110 \rangle$. Glide can occur in other planes such as $\{100\}$ and $\{211\}$ less frequently and typically under higher stress for the $\{100\}$ glide. The typical glide planes in FCC material are illustrated in Figure 2.

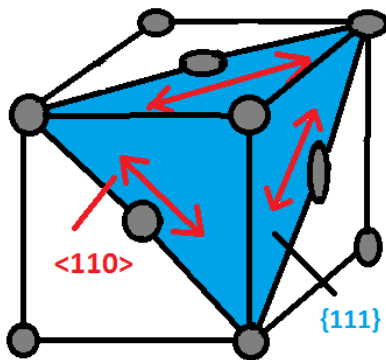


Figure 2 - Schematic of the unit cell, highlighting the (111) plane in blue, and $\langle 110 \rangle$ directions in red.

Dislocations can be of two general types. The first type of dislocation is an edge dislocation. Edge dislocations are an extrinsic crystallographic defect in that an extra atomic plane is inserted into the matrix, see Figure 3a. Screw dislocations create a helical defect as illustrated in Figure 3b. For edge dislocations the Burger's vector is normal to the line direction, while for screw dislocations the Burger's vector is parallel to the line direction. Dislocations may bow around obstacles, becoming a mix of screw and edge dislocations.

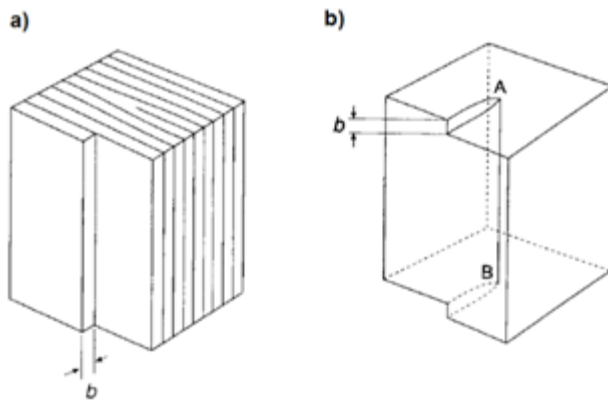


Figure 3 – Schematic of a perfect edge and screw dislocations, a) Edge dislocation, b) screw dislocation. Reprinted from Hull, Bacon [13] with permission of Elsevier publishing.

If a screw dislocation's Burger's vector is $\mathbf{b} = \frac{a_{lattice}}{2} [\bar{1} 0 1]$, then the Burger's vector is contained on both the $(1 1 1)$ and $(1 \bar{1} 1)$ planes. Because the Burger's vector is contained in both planes, the screw dislocation may slip onto the alternate plane. This slipping onto an alternate plane is referred to as 'cross slip' and is illustrated in Figure 4. Cross slip is exclusive to screw dislocations.

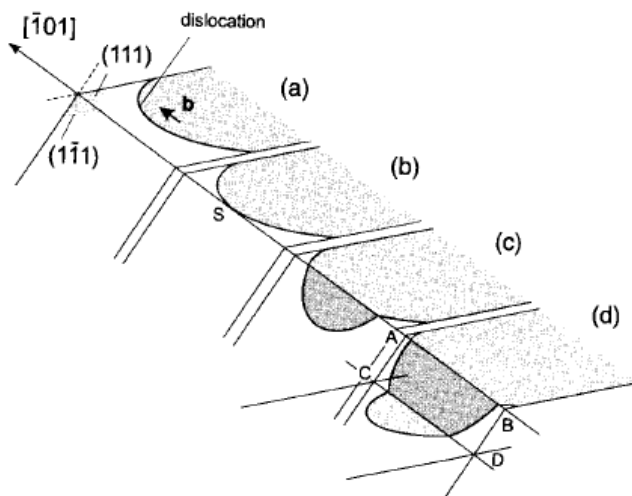


Figure 4 – Schematic of screw dislocation cross slip, a-c), progressive slip from (111) to $(1\bar{1}\bar{1})$ planes, d) Double cross slip back to the (111) plane. Reprinted from Hull, Bacon [13] with permission of Elsevier publishing.

When atoms are stacked in a cubic fashion in the FCC lattice, there are two lattice sites the atoms may fall onto denoted "B" and "C" in Figure 5. The (111) planes of the FCC lattice are stacked in an ABCABCABC fashion. Should the order become displaced so the stacking is imperfect such as ABCA'C'BCABC a stacking fault has occurred.

When a $\langle 110 \rangle \{111\}$ type dislocations pass from location 1 to location 2 (line b_1 in Figure 5), the atoms must push through the upper (stacking layer 'C') and lower atoms (stacking layer 'A') cross sections, causing a large energy barrier. A more energetically favorable process is to pass the slipping atoms across the gaps between the atomic layers as shown in Figure 5 (line b_2 to b_3 in Figure 5). For this to happen, the dislocation must first split into partial dislocations. This process is commonly referred to as Shockley partial dislocation motion.

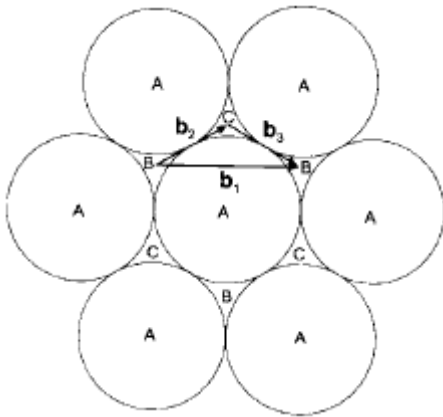


Figure 5 - Potential atomic paths for dislocation motion on {111} planes. Reprinted from Hull, Bacon [13] with permission of Elsevier publishing.

The disassociation of the dislocation leaves a stacking fault behind the leading partial dislocation, and the trailing partial dislocation corrects this stacking fault [13]. See Figure 6 for an illustration of a stacking fault left by Shockley partials.

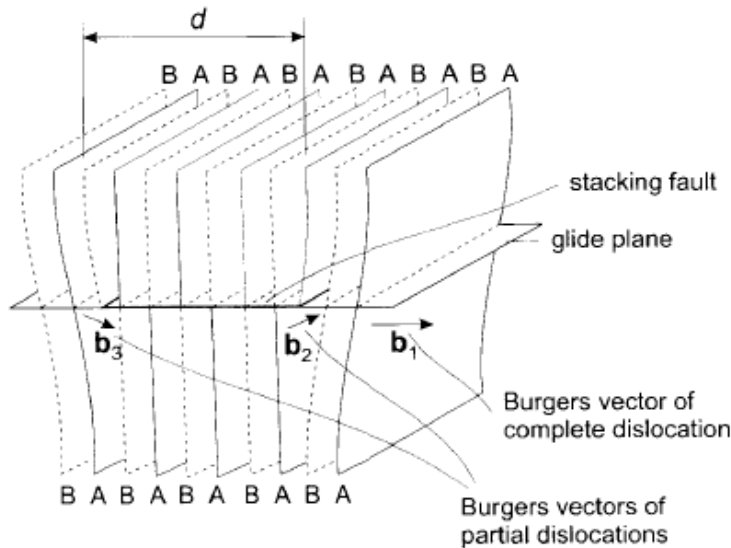


Figure 6 – Illustration of a stacking fault left between slip of Shockley partial dislocations (b_3 and b_2). from Hull, Bacon [13] with permission of Elsevier publishing.

Separation of a perfect dislocation into Shockley partials occurs frequently in FCC metals [13]. An example of Shockley partials in FCC material is formulated in Equation 3.

$$\frac{1}{2}\langle 110 \rangle \rightarrow \frac{1}{6}\langle 211 \rangle + \frac{1}{6}\langle 12\bar{1} \rangle$$

Equation 3 - Shockley partial equation

The equilibrium spacing between the partial dislocations is inversely proportional to the stacking fault energy [13], see Equation 4 . Larger stacking fault energies lead to shorter separation of partial dislocations. Partial dislocation motion also plays a role in formation of twin boundaries.

$$d_{SP} = \frac{Gb^2}{4\pi\gamma_{SFE}}$$

Equation 4 - Formula to calculate the equilibrium spacing of partial dislocations. Where ' d_{SP} ' is the equilibrium spacing between Shockley partials, ' G ' is the shear modulus, ' b ' is the Burger's vector, ' γ_{SFE} ' is the stacking fault energy.

For partial dislocations to cross slip, the partial must first be collapsed to a perfect dislocation as only one $\{111\}$ plane contains the $1/6\langle 112 \rangle$ slip vector. Since there is a

stacking fault between the partial dislocations, an energy barrier must be overcome to collapse the partial dislocation into a perfect dislocation. The farther the partial dislocations have separated, the larger the energy barrier is to collapse the partial dislocation. This energy barrier may be assisted by thermal activation; hence, cross slip for partial dislocations are more frequent at higher temperature.

1.2.1.1 Energy of dislocation disassociations

The elastic energy of a dislocation is proportional to the square of the Burger's vector as denoted by Frank's rule [13]; therefore, it follows one could sum the energies of the partial dislocations by adding the squares of each partial dislocation's Burger's vector. One could then compare the energy of the partials to the original Burger's vector and if the sum of the energies of the partial dislocation is less than the original Burger's vector separation into partials is energetically favorable, as shown in Equation 5.

$$\text{Perfect dislocation: } \mathbf{b} = \frac{1}{2} \langle 1 \ 1 \ 0 \rangle : b^2 = \frac{a^2}{4} (1^2 + 1^2 + 0^2) = \frac{a^2}{2}$$

$$\text{Partial dislocation: } \mathbf{b} = \frac{1}{6} \langle 2 \ 1 \ 1 \rangle : b^2 = \frac{a^2}{36} (2^2 + 1^2 + 1^2) = \frac{a^2}{6}$$

$$\text{Partial dislocation: } \mathbf{b} = \frac{1}{6} \langle 1 \ 2 \ \bar{1} \rangle : b^2 = \frac{a^2}{36} (1^2 + -2^2 + 1^2) = \frac{a^2}{6}$$

$$\frac{a^2}{2} > \frac{a^2}{6} + \frac{a^2}{6}$$

Equation 5 – Computation of Franks rule for perfect and partial dislocations.

1.2.1.2 Nonconservative dislocation motion in FCC materials

Nonconservative dislocation motion involves dislocation movement out of the glide plane. For a dislocation to move out of its glide plane a vacancy must diffuse to the dislocation front as illustrated in Figure 7. Because generation and diffusion of vacancies is a thermally activated process climb happens at higher temperatures. Climb is exclusive

to edge dislocations. Deformation processes requiring climb are typically strain rate sensitive as time is needed for the diffusion of vacancies.

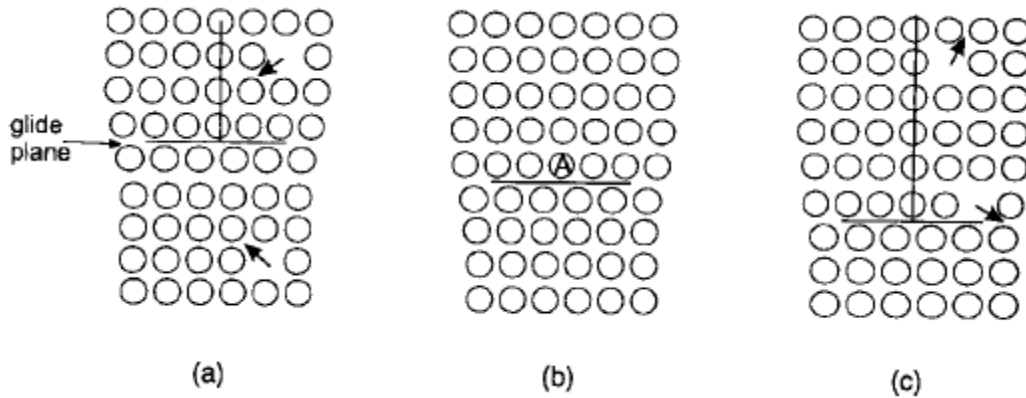


Figure 7 – Illustration of climb process for edge dislocations, a) positive climb, b) original dislocation, c) negative climb. Reprinted from Hull, Bacon [13] with permission of Elsevier publishing.

1.2.2 Interactions of dislocations in FCC materials

As noted previously in Figure 3 p6, dislocations have a displacement and stress field around them. Should these dislocations encounter one another, they will react in a way that reduces the overall energy. For the two edge dislocations on gliding on the same plane as depicted in Figure 8a the dislocations will tend to repel each other as if they were right next to each other with an energy of $2b^2$. The two edge dislocations of the opposite sign as in Figure 8b would annihilate as the energy would be $0b^2$. The two dislocations separated by a few atomic planes in Figure 8c would tend to align vertically as it would reduce the total energy. The dislocations may also climb to annihilate. For edge dislocations these interactions tend to couple the dislocations into a 'dipole'. For screw dislocations, interactions tend to be annihilation type interactions since they readily cross slip.

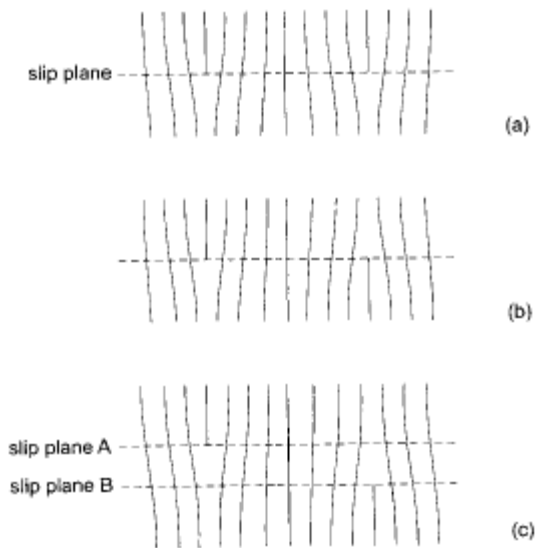


Figure 8 – Arrangements of edge dislocations, a) like dislocations on the same plane, b) unlike dislocations on the same plane, c) unlike dislocations separated by a few planes. Reprinted from Hull, Bacon [13] with permission of Elsevier publishing.

The situation in Figure 8a may commonly arise when dislocations encounter an obstacle such as a coherent precipitate. The precipitate may arrest the dislocation at the interface between the precipitate and the matrix. Further dislocations will act to amplify the local stress, until the dislocation can either penetrate the precipitate or bow around the precipitate. Should the dislocation bow around the precipitate, the dislocation will leave a loop around the precipitate, freeing the dislocation for further glide. This looping bypass mechanism is referred to as 'Orowan looping'.

Should dislocations cross each other a lock may form. Dislocation locks arrest or impede further dislocation motion causing an increase in applied stress for further dislocation glide and mechanical deformation. This increase in applied stress required for deformation is a process referred to as 'strain hardening'.

One such lock involves partial dislocations. When two partial dislocations cross paths such as depicted in Figure 9, the Lomer-Cottrell lock will form. The Burger's vector of the two gliding partial dislocations will combine into a $1/6[011]$ type dislocation as

calculated in Equation 6, which will lock dislocation motion as the Burger's vector does not glide on the $\{111\}$ planes [13].

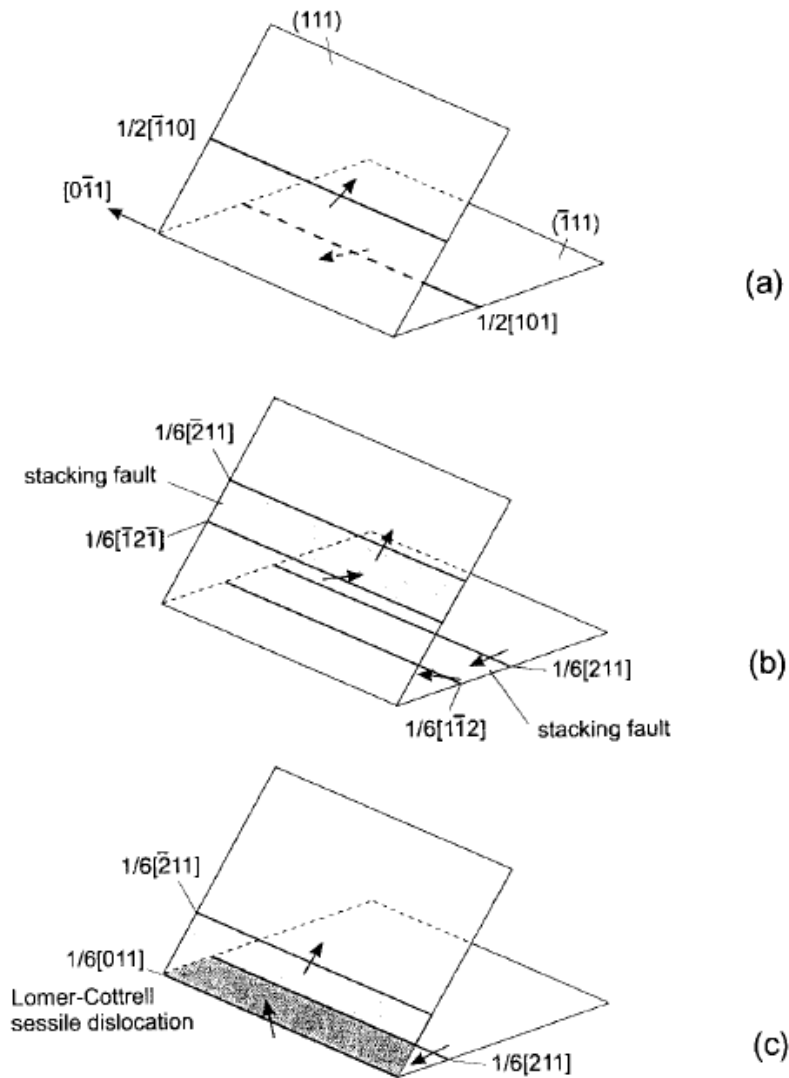


Figure 9 – Schematic of Lomer-Cottrell lock, a) perfect dislocations, b) disassociation into Schockley partial dislocations, c) partial dislocations combine forming Lomer-Cottrell lock. Reprinted from Hull, Bacon [13] with permission of Elsevier publishing.

$$\frac{1}{6}\langle \bar{2} 1 1 \rangle + \frac{1}{6}\langle 2 1 1 \rangle \rightarrow \frac{1}{6}\langle 0 1 1 \rangle$$

Equation 6 - Lomer-Cottrell locking mechanism

Another such lock involves perfect dislocations. Dislocations may cross with another glissile or sessile dislocation leaving a jog which may lock one or both of the dislocations. The jog segment (illustrated in Figure 10) will have the same Burger's vector, but a perpendicular line vector. For edge dislocations, the Burger's vector is still in the slip plane, and no lock will form. However, for screw dislocations, the Burger's vector is not contained in the slip plane and a lock will form.

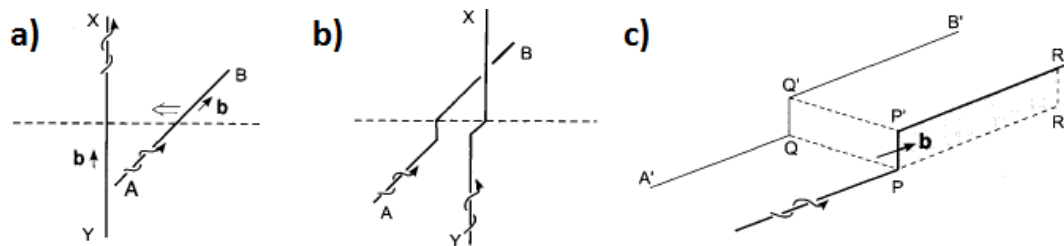


Figure 10 – Schematic of jogs in screw dislocations, a) two screw dislocations, b) two screw dislocations after they have passed each other, c) illustration of jog locking mechanism in screw dislocations. Reprinted from Hull, Bacon [13] with permission of Elsevier publishing.

As dislocations continue to glide and lock, a situation where a dislocation has double cross slipped or two jogs has pinned a small section. This small line segment may under sufficient stress, bow out and around back in on its self, forming a Frank-Reed source as depicted in Figure 11.

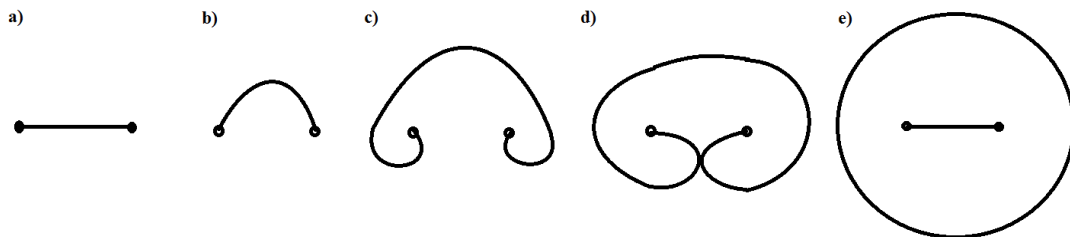


Figure 11 - Progression of Frank Reed dislocation multiplication source. a) locked dislocation between two obstacles b-d) bowing of dislocation back onto its self, e) dislocation loop formed and process repeats itself.

Other dislocation multiplication mechanisms exist and are explained in more detail in Hull and Bacon [13].

1.2.3 Cyclic deformation in FCC material

As materials are cyclically stressed dislocations will accommodate the stress by gliding. During cyclic deformation in single crystals, dislocation dipoles will tend to gather forming a vein structure as shown in Figure 12a. The dipoles are a low energy configuration for edge dislocations as each acts on each other's stress field to partially cancel it out. Dislocation dipoles tend to be exclusively edge dislocations, as dipole screw dislocations will cross slip and annihilate [5]. Upon further stress the persistent slip bands are formed as shown in Figure 12b, and under further stress a labyrinth and/or cell structure is formed as in Figure 12c.

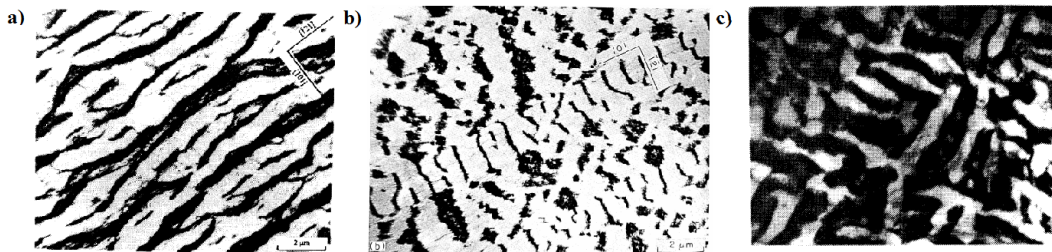


Figure 12 - Cyclic stress strain response for ductile single crystals. a) Dislocation vein structure, composed of edge dipoles [25], b) persistent slip band structure, featuring the ladder and rung structure [25], c) labyrinth structure [26]. Reprinted with permission of Elsevier publishing [25] [26].

Polycrystalline materials behave similar to single crystal alloys in that hardening mechanism such as veins, persistent slip bands, and labyrinth/cell structures are observed for various alloys [5], especially under low strains [12]. However, the stress strain cyclic response observes no plateau, a variety of slip orientations means some grains may be undergoing deformation processes while others are not, and the incompatibility of elastic and plastic deformation between grains promotes multiple slip.

1.3 NBSA deformation

NBSA are composed of a gamma base matrix (Ni, FCC) and a precipitated gamma prime (Ni_3Al , L1_2). Deformation processes in γ are the same as FCC type deformations, until they encounter the gamma prime precipitate. Depending on the stress, temperature and geometry of the precipitate, dislocation motion may cut through the precipitate or bow

around the precipitate via Orowan looping [13] [9]. Small precipitates tend to be sheared by dislocations, while large precipitates are looped by Orowan mechanism [12]. When dislocations shear a gamma prime precipitate they leave behind complex stacking faults (both antiphase boundaries and stacking faults) in the gamma prime.

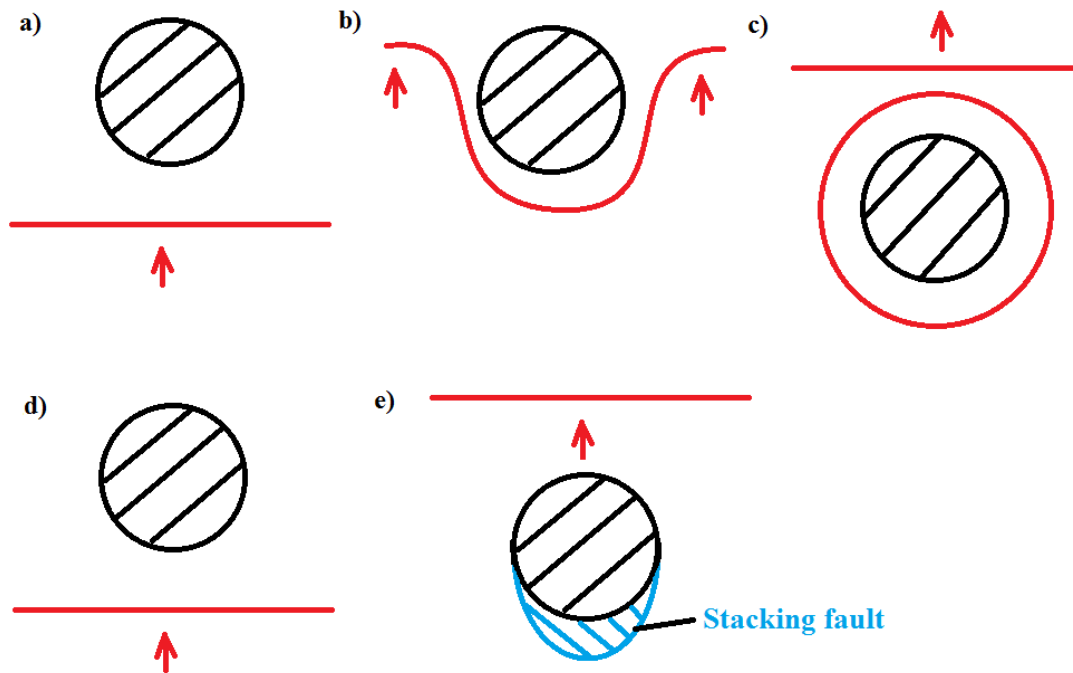


Figure 13 - Schematic of Orowan bypass mechanism (a-c) and cutting of precipitates (d-e), a) dislocation encounters precipitate, b) dislocation bows around precipitate, c) dislocation loops around precipitate, and breaks free, leaving a loop around the precipitate and a free dislocation, d) dislocation encounters a precipitate, e) dislocation shears precipitate, leaving a complex stacking fault.

Dislocations are also known to climb around precipitates as shown in Figure 14. Recall jogs left in edge dislocations are glissile, if the Burger's vector is left in the glide plane. Such is the case for edge climb around a gamma prime; therefore, climb alone will not contribute to hardening. Note screw dislocations do not climb; therefore, any evidence of climb will be from edge dislocations.

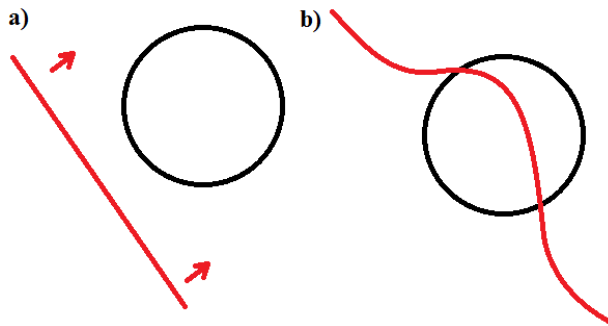


Figure 14 - Schematic of dislocation climb, a) dislocation encounters precipitate, b) dislocation climbs out of glide plane to bypass precipitate.

1.3.1 Gamma prime deformation

The gamma prime has a $L1_2$ structure shown in Figure 15a. The $L1_2$ structure is similar to FCC; however, it is a dual atom ordered structure with nickel on the faces and aluminum on the cube edges. The ordered $L1_2$ structure of gamma prime undergoes a disorder transition near the melting temperature of NBSAs [12] meaning for practical purposes, one need not worry about a disorder transition. The gamma prime shears by super dislocations and super partial dislocations. Super dislocations are for practical purposes, the regular FCC dislocations with double the Burger's vector. Super dislocations are $a\langle 110 \rangle\{111\}$ type (see Figure 15b) and super partial dislocations are $a/2\langle 110 \rangle\{111\}$ type (see Figure 15c) dislocations in gamma prime. Because the $a\langle 110 \rangle\{111\}$ type super dislocations have such a high energy associated with the dislocation (full edge diagonal displacement) the dislocation typically splits into a leading and trailing super partial dislocation as this is a lower energy configuration. The super partials leave an antiphase boundary between the leading and trailing superpartial dislocations as the Ni atoms are now on Al sites. The antiphase boundaries have similar energies to stacking faults [13].

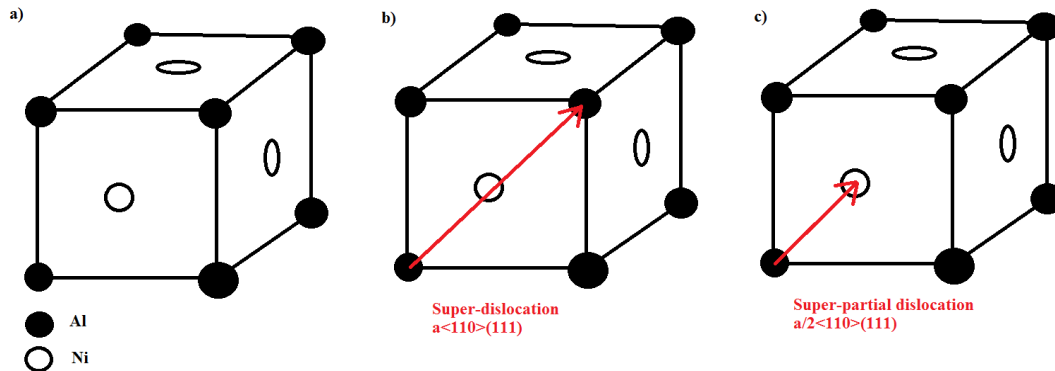


Figure 15 - Schematic of L12 γ' structure, a) unit cell, b) super dislocation, c) super partial dislocation

For dislocations to shear the gamma prime two $a/2\langle 110 \rangle_{\{111\}}$ dislocations must merge at the gamma/ gamma prime interface [14], the super dislocation then immediately separates into super partial dislocations with an antiphase boundary between the leading and trailing partial dislocations. As gamma prime is deformed a certain amount of these partial dislocations will cross slip from the $\{111\}$ planes to the $\{100\}$ planes (Figure 16) as the antiphase boundary energy is lower on the $\{100\}$ planes [14]. This cross slip from the $\{111\}$ to $\{100\}$ plane is called a Kear-Wilks lock and explains the "yield stress anomaly" where NBSAs are observed to have constant yield stress, or increasing yield stress with temperature until around 800°C [12] [13] [14]. As temperature increases, the cross slip is thermally assisted. Therefore yield stress in NBSA's is typically constant or increases with respect to temperature. The reason the yield stress drops around 800°C is because slip is activated on the $\{100\}$ planes at high temperatures, unlocking the Kear-Wilks lock [12].

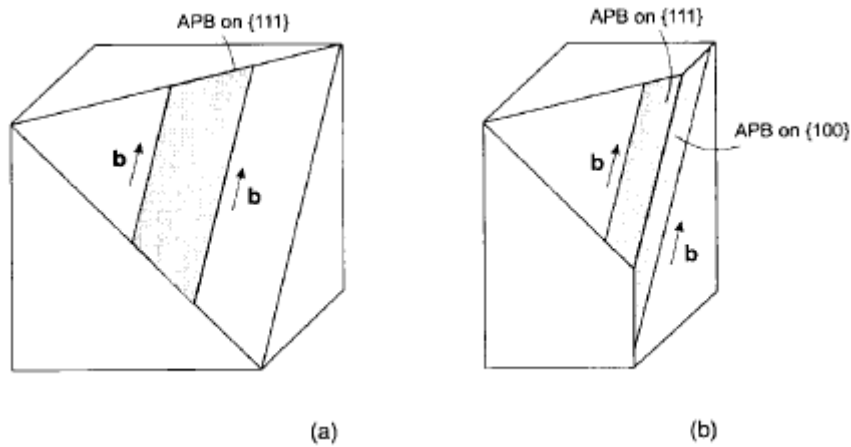


Figure 16 - schematic of the Kear-Wilford lock. Reprinted from Hull, Bacon [13] with permission of Elsevier publishing.

1.3.2 Cross slip of NBSAs

Cross slip is when the dislocation slips from its current $\{111\}$ plane to an alternate $\{111\}$ plane. If the dislocation is separated into partial dislocations the partials must collapse to a perfect dislocation before cross slipping [27]; hence, there is an activation energy associated with cross slip. If an energy intensive stair rod dislocation is formed, collapse of the partial dislocations is unnecessary for cross slip [28].

Escaig [29] proposed a model of cross slip where partial dislocations (of the screw nature) constrict and subsequently switch glide planes as shown in Figure 17. The driving stress for cross slip in Escaig's model is primarily mechanical orientation with respect to stress. The stress orientation effect has been verified in other NBSAs by Vitek et.al. [30].

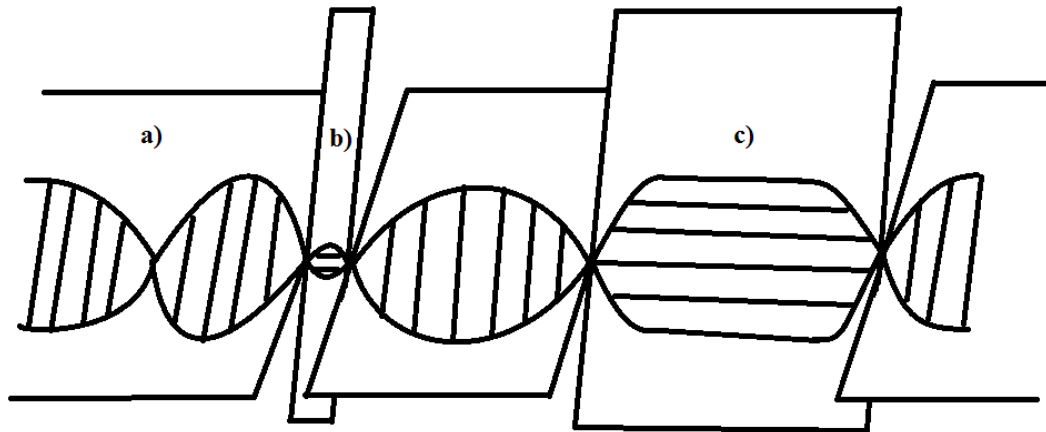


Figure 17 - Escaig model for cross slip, a) constriction of partial dislocations, b) cross slip on new plane, c) expansion of cross slip.

Cross slip is typically dependent on orientation and stress in FCC metals for pure screw dislocations [27] [28]. Cross slip of partial dislocations without a flaw in the dislocation line is rather energy intensive with energies for pure copper being estimated around 290 kJ/mol [31] [32], and 223 kJ/mol in pure nickel [33]. The activation energy decreases to between 83-65 kJ/mol in copper where the dislocation intersects a forest dislocation [34] [35].

1.3.3 Dislocation annihilation

Dislocation annihilation happens when dislocations exit the crystal surface, or dislocation of the opposite sign glide into one another. For polycrystalline materials dislocations do not typically exit the grains as plastic constraint limits the amount of deformation. Therefore, dislocation annihilation typically happens due to opposite sign dislocations gliding into one another.

Recall that dislocation vein structures are formed from cyclic loading. These vein structures contain dislocation pairs of opposite sign, separated by a few atomic planes. For edge dislocations to annihilate in this dislocation pair, they must climb. For screw dislocations to annihilate they must cross slip. Qi et al. [36] used the QM-Sutton-Chen many-body potential model [37] [38] [39] to find a screw dislocation pair separated by 8 angstroms will cross slip and annihilate. Paus et al. [40] have found the minimum

separation distance for screw dislocations to cross slip and annihilate increase from 51 nm at room temperature to 116 nm at 477°C.

Another way screw dislocations may annihilate is by jog migration. The jogs help to lower the distance between the screw dislocations, until they are close enough to annihilate (Figure 18). For pure nickel Brown [41] found that activation energy for jog migration was 12.5 kJ/mol.

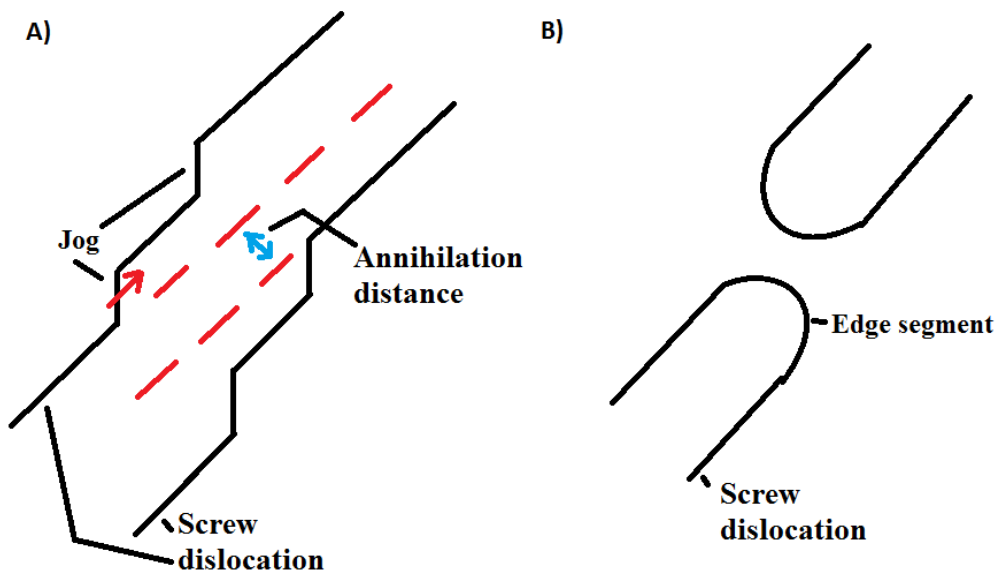


Figure 18 - Schematic of dislocation annihilation by jog migration by Hirsch [42]

1.3.4 Twinning of NBSAs

Twinning is a known deformation mechanism in nickel. High stacking fault energy metals like aluminum do not twin. However, for nickel the lower stacking fault energy allows for twin formations. Generally twinning can be classified into deformation twins, transformation twins and annealing twins. Most of the early theories of twin formation in FCC metals depend on the formation of Lomer-Cottrell locks [43] [44] [45]. Chin et al. [46] analyzed the Venables [47], Cohen and Weertman [48], Fujita and Mori [49] models finding prismatic sources of twinning inconsistent with activated slip directions, suggesting twinning originates from glide type sources rather than prismatic sources.

Theories on the origin of twinning which depend on duplex slip include the primary and coplanar [50] and primary and cross slip [51] theories. For NBSAs twinning was found to originate by pinning of partial dislocations [52] [53]. The origin of twinning mechanism is still inconclusive and argued in the literature. See Figure 19 for a schematic of twins in gamma.

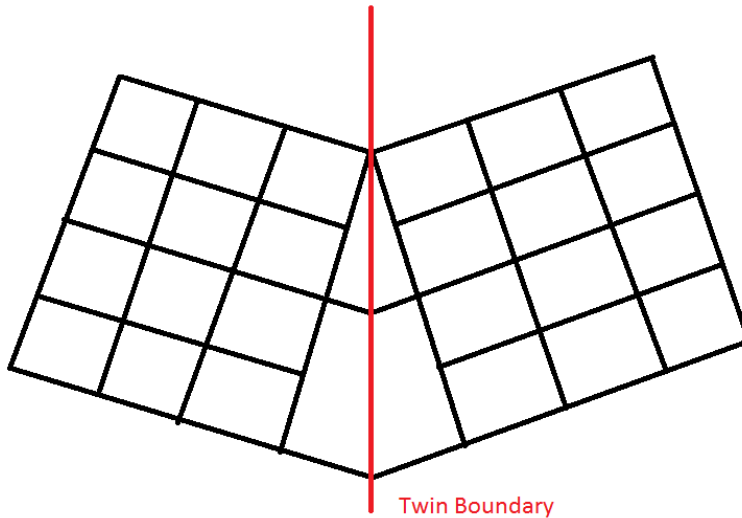


Figure 19 - Schematic of twin boundary.

For alloys Rene 104 and Rene 88DT [54], twin formation was found to be thermally activated. Similar to findings reported by Christian [55], twins precipitated by the continued motion of the leading Shockley partial [52] [53]. In gamma this mechanism forms a twin; however, in gamma prime this mechanism forms a high energy pseudotwin. Pseudotwins have both antiphase boundary and stacking faults, forming a complex stacking fault. The pseudotwin may then reorder to form a true twin by a diffusion mechanism [56] [57].

1.5 Linear elastic fracture mechanics

Linear Elastic Fracture Mechanics (LEFM) was developed to help explain why glass fibers were breaking at three orders of magnitude less than what they theoretically should have calculated from the bond strength. It was postulated that microscopic defects were

responsible for this discrepancy. LEFM does not describe how cracks initiate, but describes how cracks grow and provides estimates on the expected lifetimes of materials containing defects.

There are two main theories of LEFM. The energy criterion approach and the stress intensity approach [58]. The energy criterion states that fracture occurs when the energy available for crack growth exceeds the energy to create a new surface and the energy lost to plastic deformation [58].

The stress intensity approach states that fracture occurs when the stress-intensity factor is equal to an empirically found stress-intensity material constant. The stress intensity method measures a fracture constant, K_{Ic} , and defines this as the material toughness. Generally, a form of Equation 7 is then used to calculate the K_I value. The K_I is then compared to an empirically found material constant K_{Ic} . If K_{Ic} is met or exceeded fracture will occur [58].

$$K_I = Y\sigma\sqrt{\pi a}$$

Equation 7 - Formula for stress intensity - Where: ' K_I ' is the mode I stress intensity, ' Y ' is the dimensionless constant dependent on loading mode and geometry, ' σ ' is the applied stress, ' a ' is the applied crack length.

LEFM only applies to cases where there is limited plastic behavior experienced by the material. LEFM can be used to approximate real behavior in metals assuming the yield stress is not met or exceeded, except for a small region near the crack tip.

The stress intensity factor is unique to a geometry. Mode I (K_I) is representative of tension, while Mode II (K_{II}) is representative of in plane shear. Mode III (K_{III}) is representative of out of plane shear. See Figure 20 for a diagram of the different modes of cracking [58].

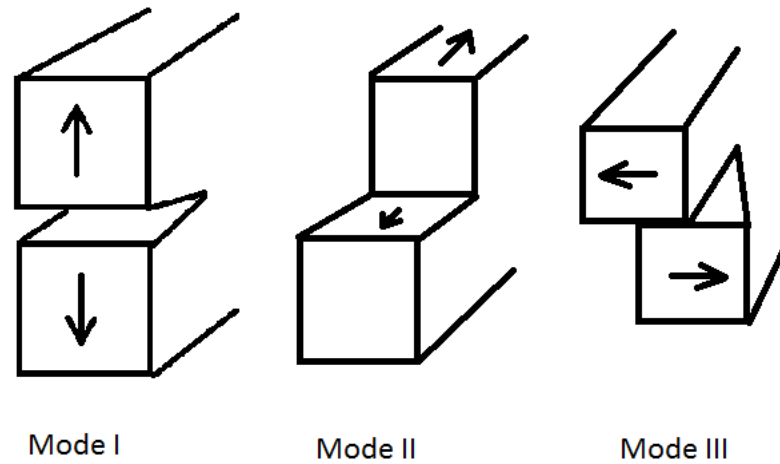


Figure 20 - Diagram showing the different modes of cracking in plane stress.

The stress ahead of the crack tip in the growth direction for mode I is:

$$\sigma = \frac{K_I}{\sqrt{2\pi r}}$$

Equation 8 - Stress ahead of crack tip. Where: 'r' is the distance from the crack tip

The major flaw with the stress intensity approach is that infinite stresses are predicted at the crack tip [58]. However, plastic deformation causes the stresses to remain finite. The size of this plastic zone is proportional to the stress intensity range. See Equation 9 for the plastic zone size for plane stress [58].

$$r_p = \frac{1}{\pi} \left(\frac{K_I}{\sigma_y} \right)^2$$

Equation 9 - Plastic zone size formula. Where: ' r_p ' is the plastic zone size, ' K_I ' is the mode one stress intensity, ' σ_y ' is the yield strength of the material.

1.6 Fatigue crack growth

As materials are cycled, irreversible damage is accumulated in the crystal structure. As this damage is accumulated, a crack will eventually form at the surface or sometimes subsurface at an internal flaw. This crack will grow if the stress intensity is below the fracture stress intensity (K_c) and above the threshold fatigue crack growth stress intensity (K_{th}).

Crack growth rates are plotted with the stress intensity against the growth per cycle as seen in Figure 21. Both axis are on a log scale. When crack growth is plotted this way three phases of crack growth are observed. In the first region of Figure 21 crack growth is not observed until a threshold stress intensity (ΔK_{th}) is reached. In the second region of Figure 21 crack growth by a power law is observed. The second region of crack growth is often referred to as the Paris region as Paris and Erdogan [59] were the first to discover the power law relationship, Equation 10, in the second region of Figure 21. In the third region on Figure 21 crack growth is seen to accelerate until final fracture.

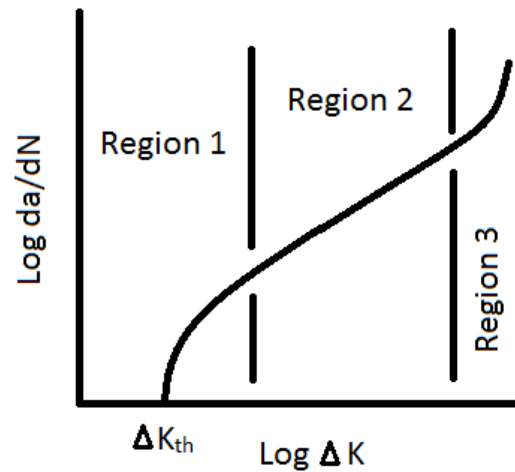


Figure 21 - Diagram of the three phases of crack growth. Region 1 is the threshold region, Region 2 is the Paris region, and Region 3 is final fracture.

$$da/dN = C_p \Delta K^m$$

Equation 10 - Where: 'da/dN' is the crack growth rate per cycle, 'C_p' is the Paris constant, 'm' is the Paris exponent, 'ΔK' is the stress intensity range

It should be noted that the stress intensity range, ΔK, is the difference between the maximum and minimum stress intensities as calculated in Equation 7.

The mechanism for crack growth involves dislocation glide. As dislocations glide to the crack tip, the crack will advance as dislocations exit the surface leaving a slip step. When the plastic zone is smaller than the average grain size, dislocation motion is limited to single slip, and cracks tend to grow in a wavy fashion see Figure 22a, referred to as stage one [5]. When the plastic zone encompasses multiple grains dislocation motion transitions from single slip to duplex slip see Figure 22b, referred to as stage 2 growth. Duplex slip is more complicated than single slip and leads to a planar crack growth which may show fatigue striations on the fracture surface for some alloys [5]. Stage 2 crack growth occurs by blunting and resharping of the crack tip, see Figure 22b [5], [60], [61].

7

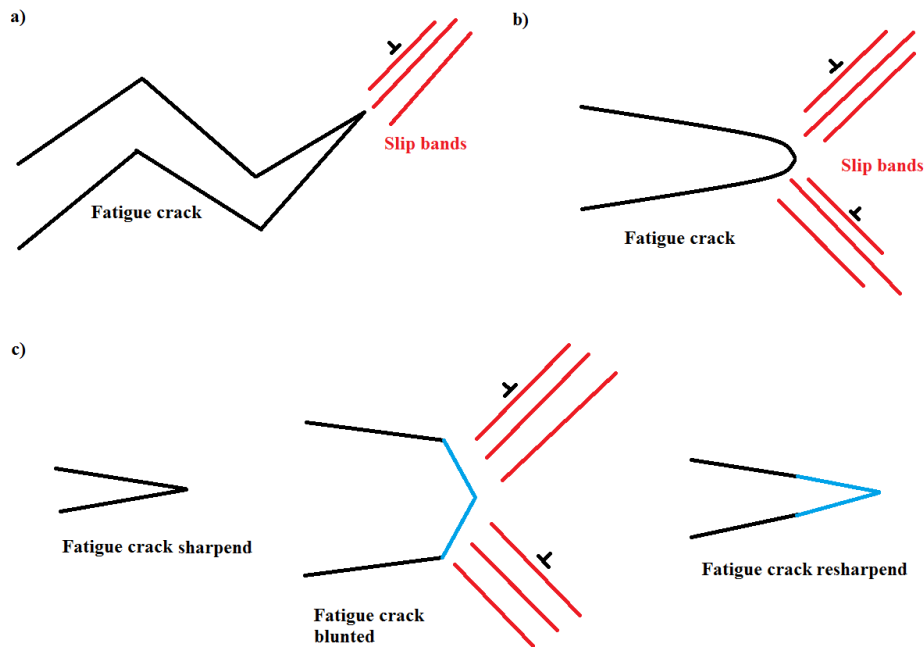


Figure 22 - Micro-mechanisms of fatigue crack growth a) stage one crack growth, b) stage 2 crack growth, c) blunting and resharpening mechanism.

1.6.1 Grain size influence on FCG in NBSAs

Microstructure greatly affects FCG and other mechanical properties of materials.

Subsolvus heat treatments which grow gamma prime tended to increase FCG rates [14].

The best yield and low cycle fatigue (LCF) resistance happens at fine grain sizes while the best FCG resistance and creep resistance happens at large grains [62].

Slip mode and environment are important factors controlling deformation in NBSAs.

Bowman tested the FCG of four unknown NBSAs (composition ranging from, Al 1.24 to 4.92, Ti, 0.01 to 3.71, Mo 0 or 9.91, Cr 9.39 to 14.18, B 0.04 to 0.06, Ni: balance in weight percent) at room temperature at 10 Hz [63]. The four alloys were chosen to control the antiphase boundary and volume fraction of gamma prime. Bowman controlled for factors such as antiphase boundary energy, precipitate size and grain size.

Bowman found in his Ph.D. thesis: i) slip mode has pronounced effects on the FCG rates at low and high ΔK , ii) low FCG rates were associated with precipitate shearing and

planar reversible slip (low antiphase boundary energy, stacking fault energy, low strain mismatch and large grains promote single shear), iii) microstructural and slip mode effects persisted at high R ratios, iv) crack closure was negligible at low R ratios. Thus it appears that FCG rates are lowered with the promotion of planar, reversible slip, which may be controlled by the composition and microstructure of the NBSA.

Waspaloy is a NBSA with low lattice mismatch and spherical precipitates. Lawless et al. [64] manipulated the grain size and precipitate size of Waspaloy while keeping the yield strength constant, and found that the slowest FCG rates were associated with largest grains and smallest precipitates (promoting precipitate shearing) while the fastest FCG rates were associated with small grains and large precipitates (promoting Orowan looping). Similar results were found from Reed [65], where Udimet 720 Li-Lg, a variant of u720 with low interstitial and large grains, showed to have the slowest FCG. Rene 88 also showed grain size effects where large grains and small precipitates were found to decrease fatigue crack growth rates by enabling precipitate shear [66].

Other FCG studies on NBSAs [67] at intermediate temperatures (427°C) with frequency of 10 Hz show that factors which promote planar reversible slip lower FCG rates. These factors include large grain size, low stacking fault and low antiphase boundary energies. Other authors have also shown an increase in FCG as grain size is reduced [68] [69] [70] [71] [72] [73].

King points out that the transition from stage one to two crack growth is delayed by increasing the grain size [74]. King also points out that under stage two crack growth multiple slip systems are active, which may intersect and cause rapid hardening.

1.6.2 Creep influence on FCG in NBSAs

At elevated temperatures, typically greater than 0.3 homologous temperature, creep may affect crack growth [75]. Creep is a time dependent process. Typical NBSAs exhibit small scale creep during fatigue tests as hold times are short and loading is relatively minor [76]. Creep processes generally involve self-diffusion. Diffusion is a slow process requiring some time to pass. Therefore, for FCG tests done at higher frequencies creep is

not expected to influence FCG as inadequate time is allotted in the loading waveform for creep processes, even at higher temperatures.

Creep mechanisms in NBSAs include (but are not limited to) cavitation, grain boundary sliding, and strain aging behavior. Cavitation is the formation of voids in the material, typically at grain boundaries. Creep cavitation can be greatly enhanced by gas diffusion or oxidation of carbides forming high pressure CO₂ gas [77] [78]. Grain boundary sliding contributes to intergranular crack path and can be suppressed by the precipitation of M₂₃C₆ type carbides and boride compounds, which tend to precipitate on grain boundaries [12] [14] [79]. Larger grain size can reduce grain boundary sliding as there is less grain boundary area. Strain aging is a phenomenon observed where decreasing the strain rate increases the dislocation flow stress. Strain aging is observed in several NBSAs [80] [81] [82] [83]. Strain rate sensitivity is typically caused either by deformation rate limited by climb or by dislocations dragging interstitial atoms.

Other mechanisms of creep include Nabarro-Herring (bulk diffusion) , Cobel (grain boundary), and climb assisted dislocation glide. Nabarro-Herring creep involves diffusion through the bulk of the lattice, while Cobel creep involves diffusion only along grain boundaries. Climb assisted dislocation glide is where dislocations climb out of their glide plane by thermal activation. The out of plane motion allows the dislocation to glide around obstacles. Specific creep mechanisms are usually determined from an Ashby map [84]. Creep will have the effect of increasing the FCG rates.

For creep to have an influence in FCG the creep damage zone must be comparable to the LEFM plastic zone (Figure 23). If creep is much smaller than the LEFM plastic zone, then creep will not affect the FCG mechanism. However, if the creep damage zone exceeds the LEFM plastic zone (as shown in Figure 23) then creep will have large effects on FCG rates.

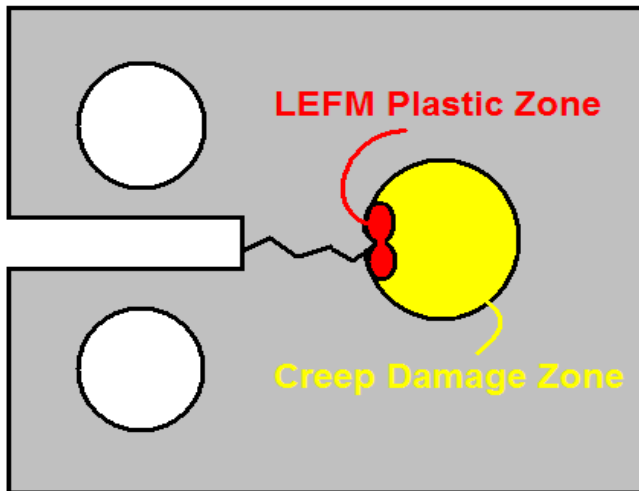


Figure 23 - Schematic of the influence of creep and LEFM plastic zone on FCG.

1.6.3 Other influences on FCG in NBSAs

Oxygen is known to accelerate FCG in Inconel 718 (IN718) [85]. Mollins et.al. [85] studied this oxygen effect in IN718 and found FeO and NiO type spinels were responsible for the increased FCG rates. Mollins et.al. found that if Cr_2O_3 type oxide could be promoted (shielding oxide formation), or rapid stress relaxation (by creep), environmental effects could be mitigated.

For Inconel 718 (IN718) and Udimet 720 (U720) oxygen is attributed to a transition from transgranular stage 2 crack growth to intergranular growth after the crack has grown a few grains in size [9] [65]. Crack oxides forming wedges [86], long range diffusion causing embrittlement effects [87] [88], or carbon oxidation to form CO gas have all been proposed mechanisms to transfer cracking mode from transgranular to intergranular. However, oxidation is also reported to slow FCG by oxide induced crack closure as shown in IN718 by Yuen et.al. [89]. Oxidation seems to have two competing roles: one is to intrinsically increase the FCG rates, and the other is to increase the fracture surface roughness and reduce the FCG rates [67].

Precipitate phases also contribute to FCG rates. Hunt et.al [90] observed a considerable increase in FCG rates for the alloy RR1000 when aged to precipitate the sigma phase.

1.7 Activation energy

Activation energy is the minimum energy required for a transformation process to take place. Some processes may be chemical in nature, like oxidation, while others are diffusion related. Still other processes may be enhanced by thermal activation, such as cross slip or dislocation velocities.

Slip in metals is known to be temperature dependent [13]. Some barriers to dislocation slip can be overcome by the addition of thermal energy into the system, which increases the vibration amplitudes of the crystal. The increased lattice vibrations assist dislocations to slip over a barrier they could not overcome by the applied force alone (Figure 24).

Typical barriers in NBSAs can be solute atoms, dislocation jogs, antiphase boundaries, grain boundaries, or precipitates, all of which tend to impede dislocation motion.

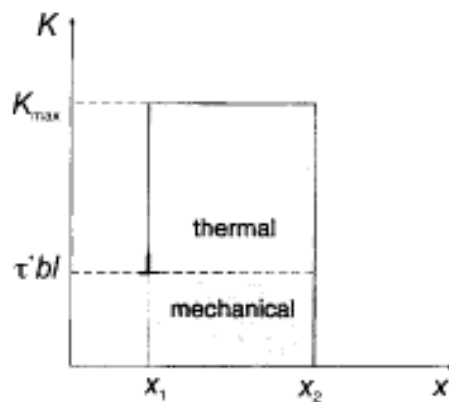


Figure 24 - Schematic illustrating activation energy, reprinted from [13].

Chemical phase changes such as oxidation also require an energy barrier to break chemical bonds and form new ones. Oxidation is a well known phenomenon in NBSAs which can be responsible for transitions from transgranular crack growth to intergranular [7] [6] [8].

Calculating the activation energy is a useful analysis tool to help identify the active cracking mechanisms. Typical mechanisms responsible for thermal activation energy are: a) environmental effects such as oxidation, b) creep c) changes in temperature

dependent mechanical properties such as yield strength and Young's modulus and d) thermally enhanced slip [91].

1.7.1 Mechanisms related to activation energy

Certain processes such as dislocation climb require vacancy diffusion [13]. Vacancy diffusion is a thermally activated process and increases with temperature. There is a threshold temperature where dislocation climb occurs as a minimum number of vacancies must diffuse to the dislocation front before climb can occur. For this reason activation energy may appear null until a certain threshold temperature is reached, see Figure 25. Creep related activation energies for NBSAs are around 150 kJ/mol [91].

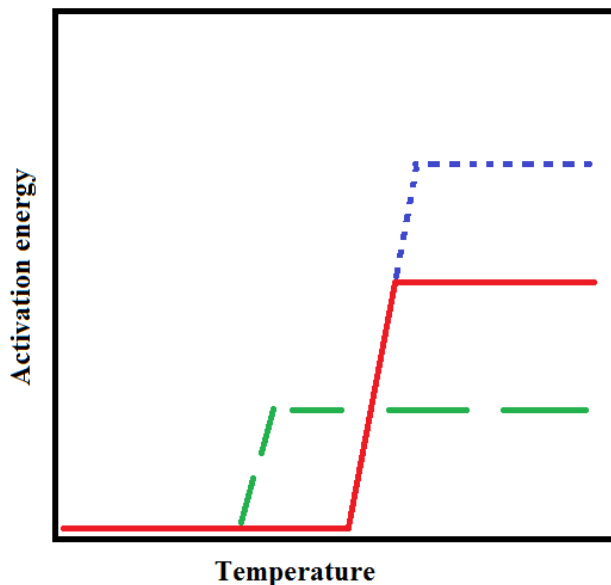


Figure 25 - Schematic illustrating temperature dependence of activation energy. Green dashed line represents a low energy process activated at low temperature, where red solid line illustrates a higher energy process activated at a higher temperature. Blue dotted line illustrates a combination of both processes.

Oxidation is also a detrimental process which requires a threshold activation energy.

Further details on oxidation were discussed prior, see 1.6.3 Other influences on FCG in NBSAs. The activation energy for oxidation related mechanisms is around 250 kJ/mol [91], but can be lower depending on alloy chemistry.

Mechanical properties such as yield strength and Young's modulus change with temperature. Activation energy associated with temperature dependent mechanical properties is estimated from Starink to be 0-60 kJ/mol [91].

Dislocation motion may be thermally assisted. Yokobori et.al. [92] [93] [94] proposed fatigue crack growth rates were thermally activated. Yokobori claimed the probability of the crack tip extension followed an Arrhenius type relation. Yokobori calculated the dislocation velocity of an isolated dislocation in [93] which contained an Arrhenius type relation, showing that at higher temperatures, dislocations velocities increase, and are more likely to exit the surface, advancing the crack by one Burger's vector per dislocation leaving the crystal. Yokobori theorized that while there is sufficient mechanical stress for dislocation glide, the velocity of the glide is thermally enhanced. The theory is that crack extension per cycle is equivalent to the mathematical product of the absolute crack extension and the probability of extension.

Other processes related to activation energy include dislocation climb and cross slip. These processes were discussed prior in Reprinted from Hull, Bacon with permission of Elsevier publishing.

1.3.2 Cross slip of NBSAs, p19 and 1.6.2 Creep influence on FCG in NBSAs, p28.

1.7.2 Other effects of elevated temperature on NBSAs

At elevated temperatures microstructural changes may occur. These changes may include grain, gamma prime or carbide growth. Dynamic recrystallization or precipitation of alternate phases may also occur at elevated temperatures.

Grain boundary growth and dynamic recrystallization do not occur until temperatures above 1000°C for NBSAs [95] [96]. Growth of gamma prime is largely dependent on gamma/gamma prime mismatch and solute distributions [97]. Activation energy for gamma prime growth is ~288 kJ/mol which is correlates with the diffusion activation energies of Al, Ti and Nb in the nickel matrix. Carbide growth is observed at temperatures as low as 600°C in some NBSAs [95].

Lastly, synergistic effects were observed between creep and fatigue in Waspaloy. Unexpectedly accelerated growth of gamma prime precipitates was observed in Waspaloy at 800°C [98].

1.8 Fractography

Fracture surfaces are commonly investigated optically or by a scanning electron microscope (SEM). The SEM is more popular as the SEM has a larger depth of field than the optical microscope. The SEM works by accelerating electrons, impacting them at the desired surface and imaging from the scattered electrons. The three most important signals for the SEM include, secondary electrons, backscattered electrons and X-rays [99]. Secondary electrons are low energy electrons produced near the surface of the material imaged. Backscattered electrons come from deeper in interaction volume, yielding electron energies near that of the incident beam and contain information such as the relative atomic density of the material. X-rays contain specific information on the atomic elements present.

Fatigue crack paths are known to be transgranular (through the grains) or intergranular (between the grains). The intergranular crack path will appear faceted, while the transgranular crack path will be planar. For alloys Inconel 100 [7], Udimet 720 [8], N18 [6], LSHR [6] the fatigue crack path is observed to be intergranular at low frequencies (typically lower than 1 Hz), high temperature (typically higher than 500°C) and in oxygen environment.

Along with intergranular and transgranular fracture surfaces, commonly observed features include river markings, fatigue striations and grain boundary cavitation. Fatigue striations (illustrated Figure 26a) are explained in more detail above in, section 1.6 . River markings are common in brittle materials when the crack path crosses high angle grain boundaries [99]. River markings appear like converging steps (illustrated Figure 26b). Grain boundary cavitation (illustrated Figure 26c) is where grain boundaries pull apart leaving a void in the material where a crack may initiate.

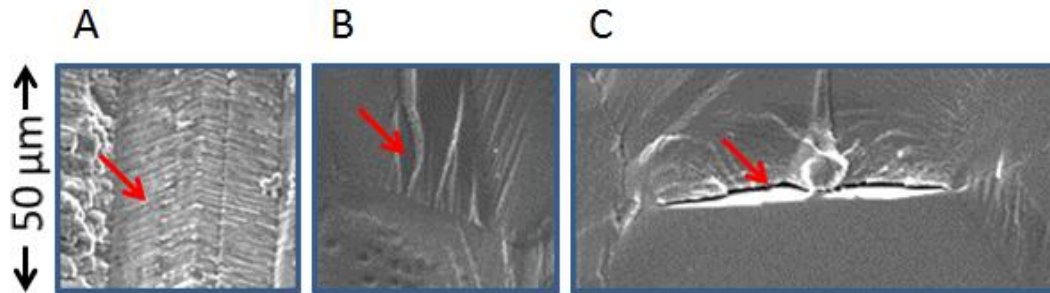


Figure 26 - Images of a) fatigue striations, b) river marks, c) grain boundary cavitation.

1.9 Transmission electron microscopy

Louis de Broglie theorized that electrons had wave like characteristics in 1925. Soon after the first transmission electron microscope (TEM) was used to image materials. Electrons have the advantage of a smaller wavelength than photons in the visible light range, allowing near atomic resolution in modern TEMs. For metallography, the TEM is a useful tool for revealing microstructural components such as dislocations, slip systems, and precipitates such as carbides and gamma prime.

Sample preparation for the TEM is more involved than for the SEM. Because electrons are being transmitted through the sample, the sample must be thinned such that electrons are able to transmit through the sample thickness. When studying the microstructure of the sample it is imperative mechanical damage is not introduced in the sample preparation.

Typically two methods are used to prepare TEM samples. Prior to the invention of the dual beam FIB/SEM samples were cut and thinned to 200 μm thick. The 200 μm thick foil would then be placed in a punch where a 3mm disk would be extruded from the foil. The 3mm disk would then be chemically or electrochemically polished until electron transparent. This punch and polish method is historic and well developed. However, the punch can introduce mechanical damage and the thinning process is somewhat random, meaning the user is unable to select a specific region of interest to investigate.

After the invention of the dual beam FIB/SEM one may use an ionic current to mill away and subsequently polish a TEM sample, commonly referred to as focused ion beam (FIB) method. The FIB uses gallium ions to image sample surfaces. Due to the bombardment of the sample with heavy ions, surfaces are slowly eroded away. The FIB method of producing TEM samples uses this to its advantage, selectively eroding a sample from the surface.

Typical sample preparation involves finding a location of interest, (for example a crack tip) and milling out trenches with a gallium beam above and below the sample. The sample is then tilted, cut free and welded to a copper grid. Typical sample sizes are approximately $10 \times 10 \times 1 \mu\text{m}^3$. After it is welded to the copper grid, the sample is tilted and thinned on both sides to an electron transparent thickness. The FIB method offers the advantage of selecting a specific place to extract a TEM sample; however, the FIB method introduces mechanical heat damage and implantation from the ionic bombardment.

While TEMs offer valuable microstructural information, one must be careful interpreting images. Firstly, the user is looking at a 2 dimensional projection of a 3 dimensional specimen. One must be careful that what is observed is not in fact a projection of two items of interest projected on top of one another. It is also possible for the transmitted beam to be diffracted multiple times as it encounters the sample, leaving a double image. Other artifacts of the TEM process include thickness and bending fringes, where fringes are projected on the image due to changes in thickness or planarity. Crystallographic strain can also cause diffraction of the beam, leading to false interpretations.

2. Literature review

Haynes 282 is a relatively new alloy, developed in 2004. Little information is available on Haynes 282 in the literature. The author has found FCG and low cycle fatigue (LCF) data from Buckson and Ojo [100]. Pike has published LCF, creep and oxidation behavior of the alloy [4] [101] [102] [103]. Hawk et al. has reported on thermal conductivity, LCF and yield strength at various microstructures and developed a Larson-Miller creep curve for Haynes 282 [104]. Referenced throughout this section are the alloys Haynes 282 (H282), Waspaloy (WSP), Rene 41 (R41), Haynes 263 (263) with chemical compositions listed in Table 2.

Alloy	Ni	Cr	Co	Mo	Ti	Al	Fe	Mn	Si	C	B	Other
282	57 ^a	20	10	8.5	2.1	1.5	1.5*	0.3*	0.15*	0.06	0.005	--
Waspaloy	58 ^a	19	13.5	4.3	3	1.5	2*	0.1*	0.15*	0.08	0.006	Zr-0.05
R-41	52 ^a	19	11	10	3.1	1.5	5*	0.1*	0.5*	0.09	0.006	--
263	52 ^a	20	20	6	2.4*	0.6*	0.7*	0.4	0.2	0.06	0.005	Al+Ti-2.6

^aAs Balance *Maximum

Table 2 – Chemical composition for various NBSAs, Reprinted with permission of The Minerals, Metals & Materials Society [101].

2.1 Thermal exposure effects of Haynes 282

With a desired service life of 100,000 hours for steam turbine rotor alloys, it is important to know the potential long term effects of thermal exposure. For example long term exposure to high temperatures may change the microstructure by overaging or precipitating detrimental phases, leading to a drop in mechanical properties.

Hawk et al. [104] ran some preliminary testing on Haynes 282. To predict the phases present in Haynes 282 at thermodynamic equilibrium a software package, Thermo-Calc, was utilized. Thermo-Calc results are graphically displayed in Figure 27 showing the predicted microstructural phases in Haynes 282 for temperatures from 400 to 1600°C.

Important results include:

- a) The gamma prime phase resolutionizes just above 954°C and service temperature (760°C/1400°F) expected to contain ~20% mole fraction gamma prime.

b) The sigma phase forms around 677°C (1250°F), peaking around 800°C (1475°F), and resolutionizing around 843°C (1550°F). Recall from section 1.1 General information about NBSAs, sigma is a plate like BCT phase which is known to cause premature creep rupture. With peak sigma around 5% mole fraction, it is not expected to cause detrimental effects, as no such effects are experimentally observed after 16000 hours in creep samples (results shown later in this section).

c) The mu phase (not observed to be detrimental) resolutionizes around 800°C (1475°F)

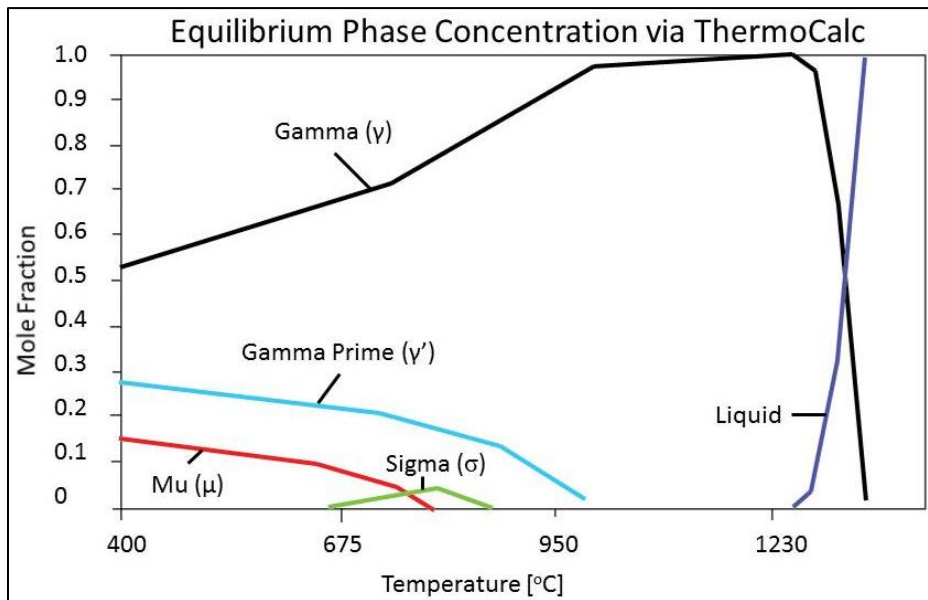


Figure 27 - ThermoCalc phase diagram for Haynes 282 showing ideal mole fractions of γ , γ' , σ , μ . Adapted from, [104].

To determine the effect of aging on Haynes 282, Hawk et al. performed various mechanical testing in the as received (solution annealed), peak aged and over aged microstructural states. Hawk et al. received a 1016 x254x35 mm³ plate from Haynes international, which was cut into thirds. The first third had no heat treatment (solution annealed). The 2nd third was peak aged by heating the plate to 1010°C for 2 hours, air cooling below 788°C, reheating to 788°C for 8 hours, and air cooling to room temperature. The last third was over aged. The plate was peak aged, followed by an

additional heating at 774°C for 250 hours. These three heat treatments give an idea of the "robustness" of the alloy properties with respect to the peak aged treatment intended to show peak strength. The solution annealed is intended to show the factory conditions and over ageing intending to artificially show the effects of long term exposure to heat. See Figure 28 for the microstructure of each heat treatment.

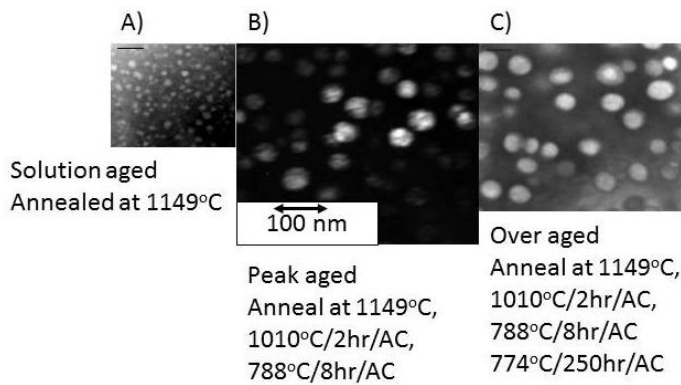


Figure 28 - Initial microstructures for Haynes 282. All images are scaled to the same scale bar. A) solution annealed (as received) showing small γ' precipitates approximately 10-20nm in diameter, B) peak aged showing γ' precipitates approximately 50 nm in diameter, C) over aged showing γ' precipitates slightly larger than 50 nm in diameter, adapted from, [104].

Tensile test results from Hawk are plotted in Figure 29. Tensile tests were done at General Electric, in accordance to ASTM E8 and ASTM E21, with strain rates of 0.003-0.007 inches/inch of gauge length per minute. After 0.2% yielding the cross head was programmed to sustain a strain rate of 0.04-0.06 inches/inch of gauge length per minute until fracture. Two important conclusions are formed from the yield stress data. Firstly, the yield stress is relatively constant at high temperatures up to about 760°C. Secondly, over aging the material does not induce detrimental effects to the yield stress.

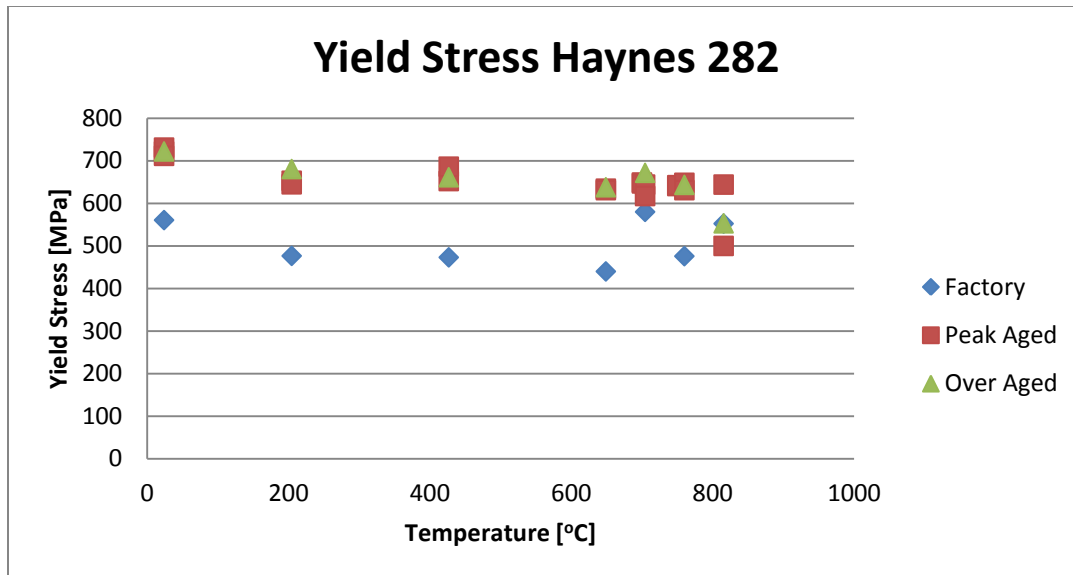


Figure 29 - Yield stress of Haynes 282 in various heat treatments [104].

Pike [101] studied effects of long term thermal exposure on the yield strength of Haynes 282 and three other NBSAs (Table 3). Pike took 1.6mm thick sheet and peak aged the sheet from each alloy according to each alloys specific peak aging recipe (see Table 3). Samples were exposed at 650, 760, 816, 871°C for 1000 hr in static air. Yield stress was measured at the temperature of the 1000 hr exposures. Samples were cut transverse to the sheet rolling direction. Yield stress at temperature is presented in Figure 30 and Table 4. At 760°C yield stress ranked from highest to lowest is: R-41, H282, WSP and 263.

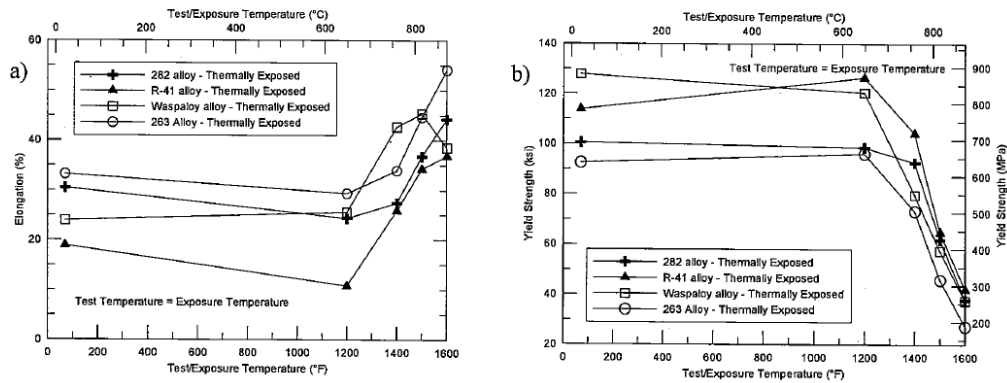


Figure 30 –Yield stress/elongation with respect to temperature of various NBSAs after 1000 hr of exposure, A) elongation, B) yield strength. Reprinted Reprinted with permission of The Minerals, Metals & Materials Society [101].

Alloy	282	Waspaloy
Annealing Temperature	2100°F (1149°C)	1975°F(1079°C)
Age-Hardening Heat Treatment	1850 °F (1010 °C)/2hr/AC + 1450 °F(788 °C)/8hr/AC	1825 °F(996°C)/2hr/AC + 1550 °F (843°C)/4hr/AC + 1400 °F(760°C)/16hr/AC
ASTM Grain Size	4.5	5

Alloy	R-41	263
Annealing Temperature	1975 °F (1079 °C)	2100 °F (1149 °C)
Age-Hardening Heat Treatment	2050 °F (1121°C)/0.5hz/RAC + 1650 °F (899 °C)/4hr/AC	1472 °F (800 °C)/8hr/AC
ASTM Grain Size	5	4

Table 3 - Heat treatment schedule for peak aging of various NBSAs [102]. AC = Air cool, RAC = Rapid air cool via fan.

1200°F(649°C)		H282	Waspaloy	R-41	263
Tensile	0.2% Offset Yield Strength, (MPa)	635	785	737	540
	Ultimate Tensile Strength, (MPa)	1042	1140	1183	897
	% Elongation	30.8	32.1	17.5	36.2
Creep	1000-Hour 1% Creep Strength, (MPa)	552	462	579	400
	1000-Hour Rupture Strength, (MPa)	558	552	621	441

1400°F(760°C)		H282	Waspaloy	R-41	263
Tensile	0.2% Offset Yield Strength, (MPa)	614	692	792	556
	Ultimate Tensile Strength, (MPa)	834	821	971	697
	% Elongation	24.8	34.9	26.9	26.4
Creep	1000-Hour 1% Creep Strength, (MPa)	241	193	234	172
	1000-Hour Rupture Strength, (MPa)	262	248	296	193

1500°F(816°C)		H282	Waspaloy	R-41	263
Tensile	0.2% Offset Yield Strength, (MPa)	570	512	730	501
	Ultimate Tensile Strength, (MPa)	688	636	805	540
	% Elongation	24.9	39.3	27.9	33.1
Creep	1000-Hour 1% Creep Strength, (MPa)	145	110	124	83
	1000-Hour Rupture Strength, (MPa)	159	138	165	103

1600°F(871°C)		H282	Waspaloy	R-41	263
Tensile	0.2% Offset Yield Strength, (MPa)	504	351	578	286
	Ultimate Tensile Strength, (MPa)	554	456	629	347
	% Elongation	35.3	50.8	29.4	62.3
Creep	1000-Hour 1% Creep Strength, (MPa)	69	48	62	41
	1000-Hour Rupture Strength, (MPa)	90	69	90	48

Table 4 – Mechanical properties of various NBSAs in peak aged state [102].

Pike also studied H282 at longer timeframes. Round samples were cut from a 12.7mm thick plate (peak aged) in the transverse rolling direction. Samples were cut out of the plate after thermal exposure ensuring the oxidized surface was machined away. Samples were subjected to 100, 1000, 4000, 8000, 16000 hr exposures at 650, 760, 816, 871°C. Yield strength at temperature is shown in Figure 31. Results of long term exposure are

promising as yield strength does not appear to drop after 16000 hours of exposure. However, at 760°C yield strength is observed to drop slightly, ~630 to 620 MPa from 8000 to 16000 hours. This is not concerning as design requirements call for yield strength of 400 MPa.

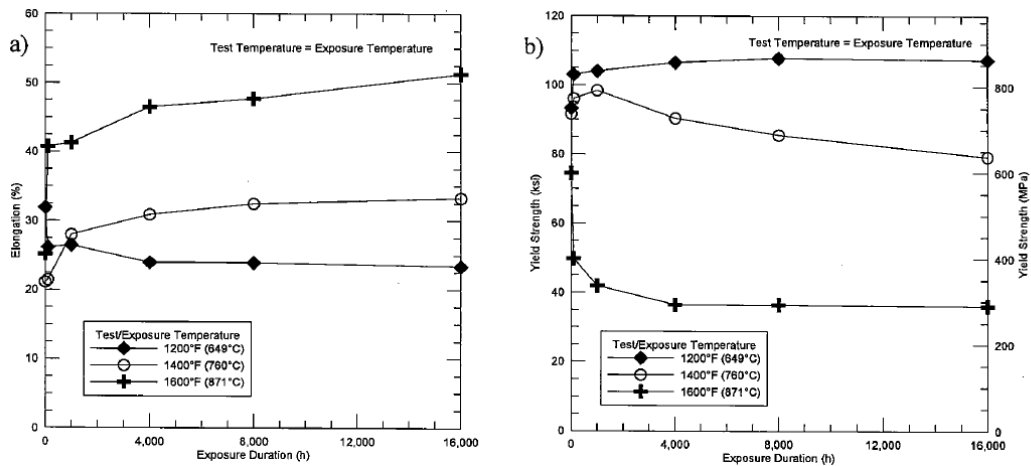


Figure 31 – Yield strength/elongation of Haynes 282 with respect to time, A) elongation, B) Yield strength. Reprinted with permission of The Minerals, Metals & Materials Society [101].

Lastly to determine the effects of oxidation at high temperature, Pike and Srivastava [103] studied oxidation properties of various NBSAs. Pike and Srivastava's results are presented in Table 5. Pike cut cold rolled commercial available sheet 1.3 to 1.9 mm thick into coupons 22 mm square. Coupons were hung in tube furnaces with air flowing at 0.2 m³/hr. Testing temperatures were at 871, 927 and 982°C. Testing time was six 168 hour cycles for a total 1008 hours exposure at each temperature. An activation energy analysis of Table 5 yielded an activation energy for oxidation over 871 to 982°C of ~120 kJ/mol for H282.

Alloy	Average metal affected		
	871°C	927°C	982°C
H282	35	46	58
R-41	35	46	84
Wasp	44	97	147
263	46	79	150

Table 5 – Oxidation depth for various NBSAs [103].

While the low oxidation energy calculated for H282 is concerning, it is only valid for temperatures in excess of 817°C. The excellent microstructural stability suggests Haynes 282 as a great alloy for long term high temperature applications.

2.2 Low cycle fatigue of Haynes 282

As turbines are started up and cooled down a complex state of stress involving thermal gradients, thermal expansion and centrifugal force may induce triaxial stress states into the rotor. Laboratory conditions do not adequately model this complex state of stress. Thermomechanical fatigue tests have attempted to simulate this complex stress state during rotor startup. However, there is much debate about accuracy, methodology and application of thermomechanical testing. Low cycle fatigue is the industry standard to simulate the worst case scenario of the complex start up and cool down state of stress experienced by rotors.

Pike [102] studied the low cycle fatigue (LCF) of H282 and other NBSAs. Sheet material 3.2mm thick was obtained for experiments. Each sheet was aged hardened according to each alloy's specific heat treatment schedule for peak aging Table 3. Fully reversed (R=-1) axial LCF was carried out at 650, 760, 816, and 871°C using a triangular waveform at 0.33 Hz. Samples were of dogbone shape oriented transverse to the rolling direction. The LCF results of H282 are presented in Figure 32 while the other NBSA's LCF data is presented in Figure 33. Relative to the other alloys tested by Pike, Haynes 282 underperforms relative to R-41, is on par with Waspaloy, and overperforms relative to 263.

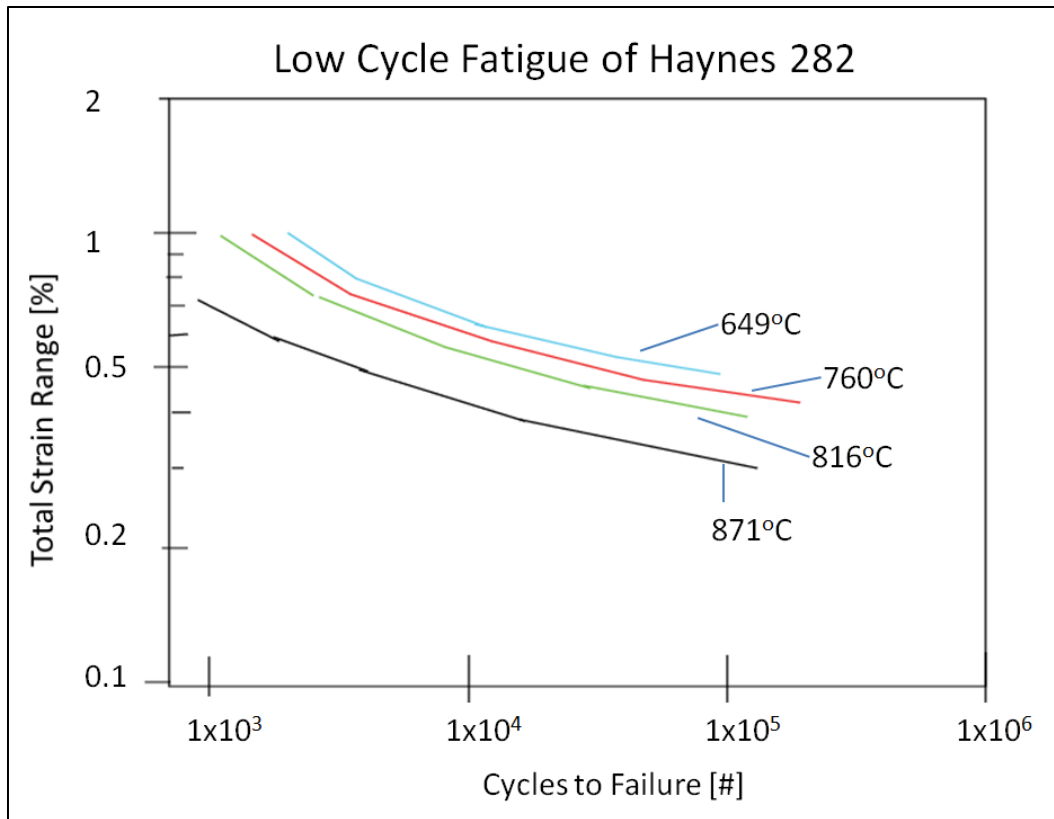


Figure 32 – LCF of H282 from 871°C to 649°C. Adapted from [102].

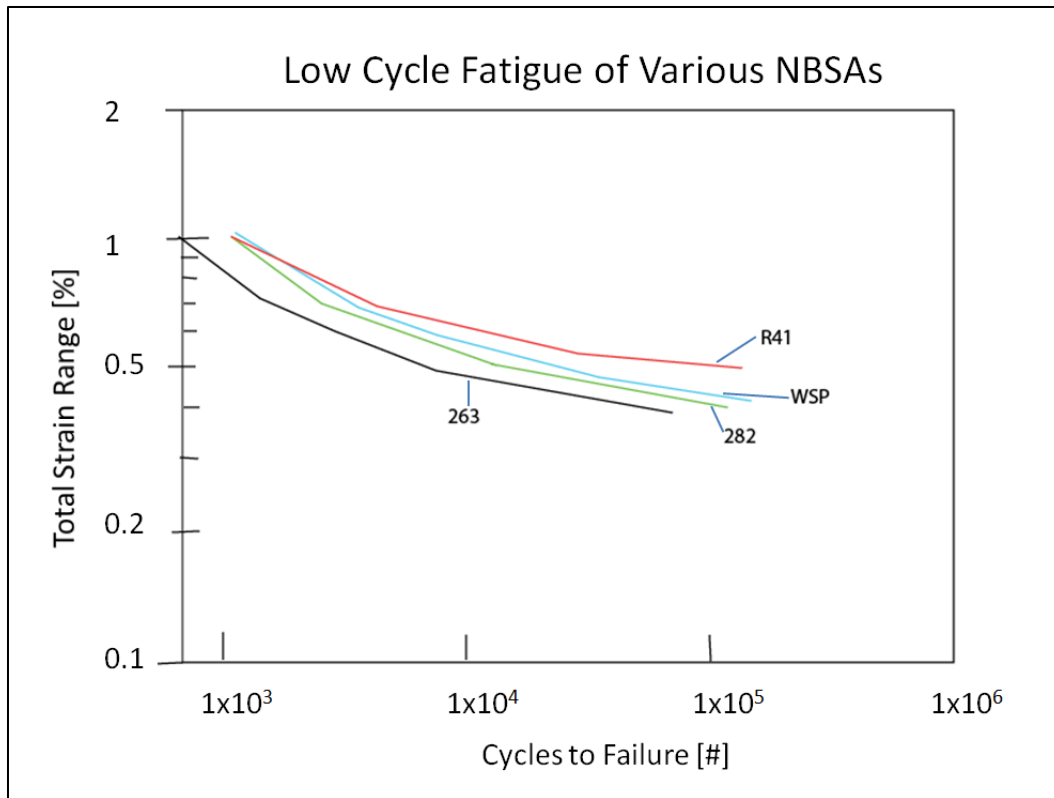


Figure 33 – LCF of various NBSAs and their stress response at 816°C. Adapted from [102].

Low cycle fatigue (LCF) was also performed on Haynes 282 by Hawk et al. [104]. Specimens were taken from the three sections of plate described prior (2.1 Thermal exposure effects of Haynes 282). Hawk's data was run at 760°C, at a load ratio of 0 at a frequency of 0.33 Hz and a triangular waveform. Hawk combined low cycle fatigue data gathered from Siemens AG and Pike (also 0.33Hz with a triangular waveform) with his own and is displayed below in Figure 34. Excellent agreement between Hawk, Siemens AG and Pike is observed for LCF.

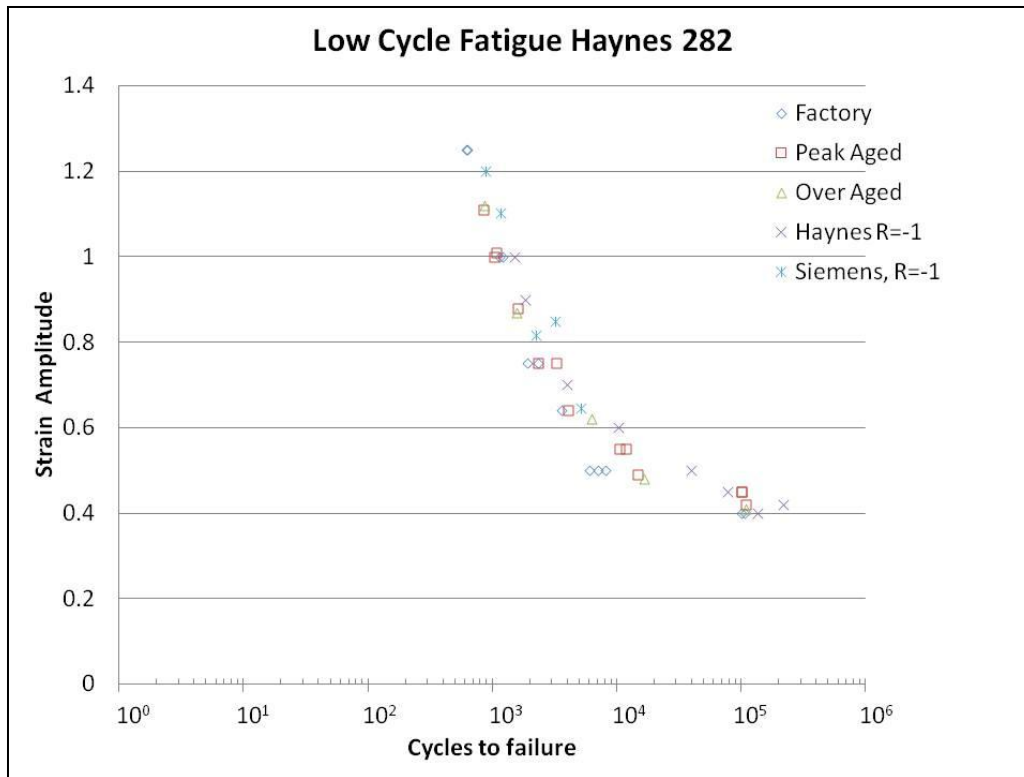


Figure 34 - Low cycle fatigue of Haynes 282 in various heat treatments at 760°C. Specimens were tested at Haynes international, Siemens and the National Energy Technology Laboratory [104].

The LCF behavior of Haynes 282 appears to be microstructurally insensitive for the measured range. From Figure 29 and Figure 34 over aging seems to have insignificant effects on the mechanical properties of the alloy.

2.3 Creep properties of Haynes 282

Creep is the time dependent plastic flow of materials at stresses below the yield stress. Creep happens at elevated temperatures where dislocation motion and vacancy diffusion are thermally assisted or activated. Creep is important to understand as rupture of a steam turbine rotor would be catastrophic, causing millions of dollars of damage and possibly loss of life.

Boehlert and Longanbach [105] studied creep and creep fatigue of Haynes 282. Boehlert and Longanbach's heat treated schedule for Haynes 282 was the same as other authors (reprinted for convenience): i) 1094°C for 20 min then water quench, ii) 1010°C for 2 hr, then cool to 788°C for 8hr, then air cool. Creep specimens had a gauge width of 12.5 mm, gauge length of 37 mm, and were cold rolled with 20% reduction in thickness to 6.5mm. Creep specimens were wire electro-discharged machined parallel to the rolling direction. Creep temperatures and stresses were 700 and 815°C and 25 and 225 MPa respectively. Creep exponents of 5-6 suggest dislocation creep, based on creep theory for pure metals [106] [107]. Measured activation energy was around 725 kJ/mol also indicating dislocation creep by lattice self-diffusion was the controlling creep mechanism. The microstructure after 70hrs at 815°C with 7.5% strain showed excessive intergranular type cracking. Creep fatigue testing at 815°C at 175 MPa stress (0.3% strain total strain) with a load ratio $R=0.1$ revealed minor grain boundary cavitation after 57 hours.

Hawk et al. studied the microstructure of Haynes 282 samples under creep. Creep was done at 37.5 Ksi (258 Mpa) and 20 Ksi (138 MPa). Creep samples were ended once specified final strain was met. For high stress creep was stopped at ~19% strain, and for low stress samples were stopped at ~0.2% strain. TEM specimens were cut and electropolished from crept samples. The TEM investigations revealed dislocation climb, super dislocation shearing of gamma prime, partial dislocation shearing of gamma prime, and microtwinning shearing of gamma prime as active mechanism in creep samples. At high strain (>18% Figure 35a) precipitates were cut by dislocation shear. At lower strain (<4%, Figure 35b) precipitates were looped via the Orowan mechanism. The Orowan mechanism causes two effects. Firstly, dislocation loops around the precipitates increase the effective size of the precipitates by placing a dislocation repelling barrier around the precipitate. Secondly, the looping decreases the effective mean particle spacing. Hawk attributed these effects as the reason why Haynes 282, with a low volume fraction of gamma prime, has similar creep resistance to higher volume fraction alloys such as IN740.

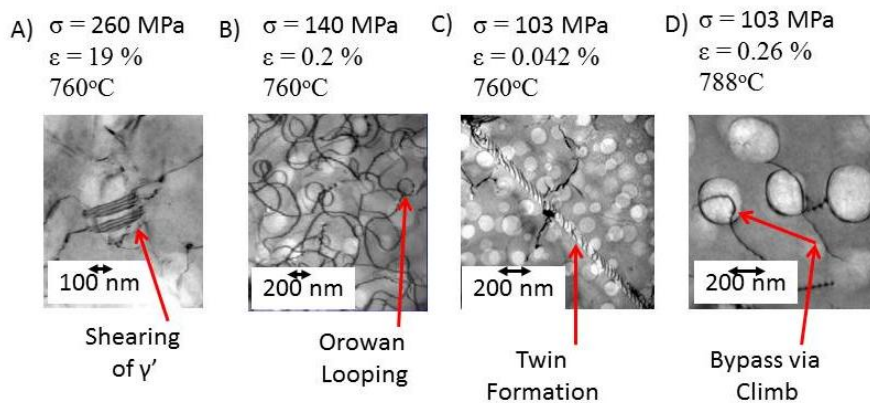


Figure 35 – TEM results of crept samples. a) Short-term creep rupture tests showing partial shearing as deformation mechanism, b) Long-term creep rupture tests, showing particle bypass as the deformation mechanism, C) Long-term creep rupture tests, twinning as the deformation mechanism, D) Long-term creep rupture tests, showing dislocation climb bypass as the deformation mechanism. Adapted from [104].

At low strain Hawk noted that creep testing seemed to be microstructurally independent. Hawk noted that initial coarsening of the precipitates was accomplished in the first few hundred hours (of 16,000 hour lifetimes), with subsequent coarsening being retarded by the depletion of solute species needed for the gamma prime. This leads to a similar final microstructure, even though the initial microstructures had varying sizes of gamma prime.

A Larson-Miller type creep curve was developed for Haynes 282 by Hawk. Larson-Miller curves show the creep rupture time compared to a Larson-Miller parameter. The Larson-Miller parameter combines temperature and time via Equation 11. See Figure 36 for the Larson-Miller curve generated by Hawk. See Figure 37 for a comparison of Haynes 282 to other rotor candidate NBSAs, note due to imperial units, 100 MPa at 760°C correlates to a LMP of 46.5. From Figure 37, U720Li does not meet minimum creep rupture requirements and IN740 is borderline.

$$LMP = T * (C_{LMP} + \log(t))$$

Equation 11 - Larson-Miller parameter equation. Where: 'LMP' is the Larson-Miller parameter, 'T' is the temperature in Kelvin, ' C_{lmp} ' is a constant in the range of 20-22, 't' is the time in hours.

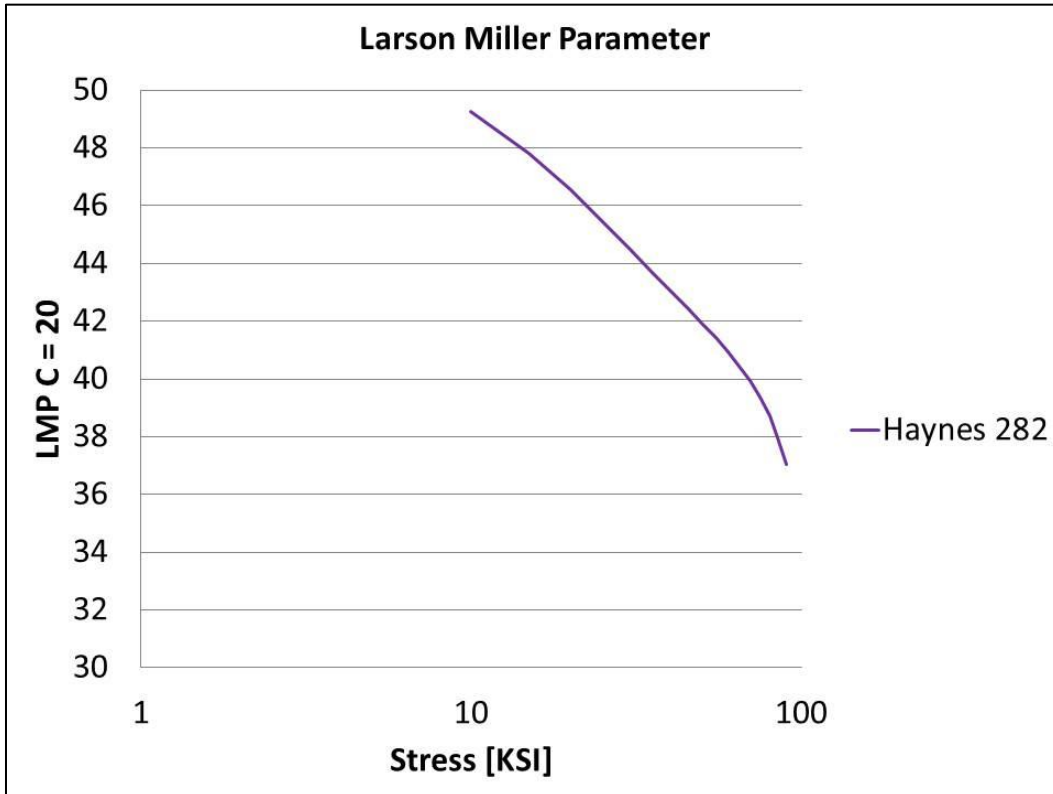


Figure 36 - Larson-Miller curve for Haynes 282 showing data from Siemens, GE, and Hawk [104]. Note 100 MPa = 14.5 KSI. Adapted from [104].

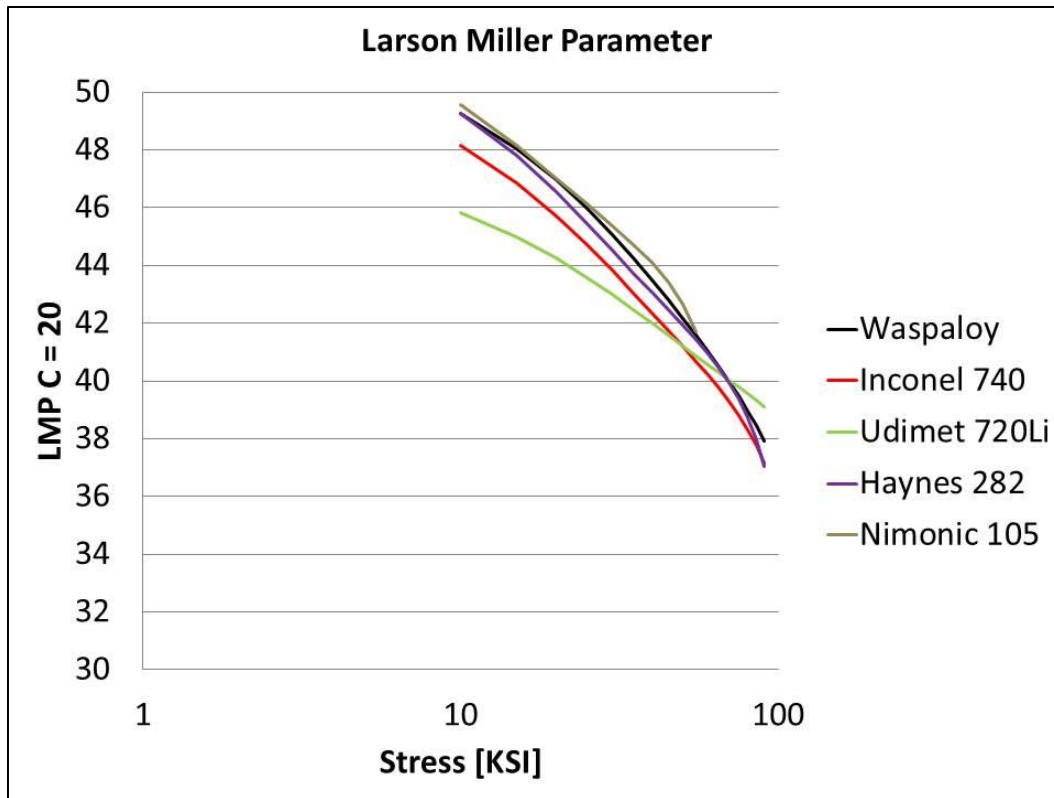


Figure 37 – Larson-Miller curve for various NBSAs considered for rotor applications [104]. Note 100 MPa = 14.5 KSI. Adapted from [104].

Hawk noted that the creep results were promising, with no detrimental phases or deformation mechanisms present at low stresses (<20ksi) and long timeframes (16,000 hours).

2.4 Fatigue crack growth of Haynes 282

When parts are designed typically one of two models is chosen. For the fail-safe model parts are designed with redundancies such that should a member fail the final product will not catastrophically fail. A classic example of this would be a truss and girder bridge where multiple trusses carry the applied load such that if one truss had a crack and failed, the whole bridge would not come down.

The other design criterion is the damage tolerant approach. For parts designed using the damage tolerant approach, parts are assumed to have flaws smaller than the detectable limit. Services intervals are then designed based on this initial detectable flaw size. To calculate the service interval one would integrate the Paris law (Equation 10, p26); hence, the need to study fatigue.

Buckson and Ojo [100] reported on the FCG behavior of Haynes 282 at ambient and 600°C while cycling at at 15 Hz and 0.05 Hz using stress ratios of 0.1 and 0.7. Buckson and Ojo used sinusoidal waveforms for all frequencies and load ratios. It was found that increasing the loading ratio increased the FCG rates. Furthermore, decreasing the loading frequency also increased the FCG rates, which was attributed to a strain rate effect.

Buckson and Ojo postulated that higher frequencies would lead to higher strain rates at the crack tip. Higher strain rates would lead to accumulation of dislocations which may lock, increasing the local yield stress. As the dislocation motion is hindered via locks, the fatigue crack growth rate would slow as more time is needed for dislocations to unlock and advance to the crack tip. Shown in Figure 38 is the FCG data gathered by Buckson and Ojo at 15 Hz, while Figure 39 features the FCG data at 0.05 Hz

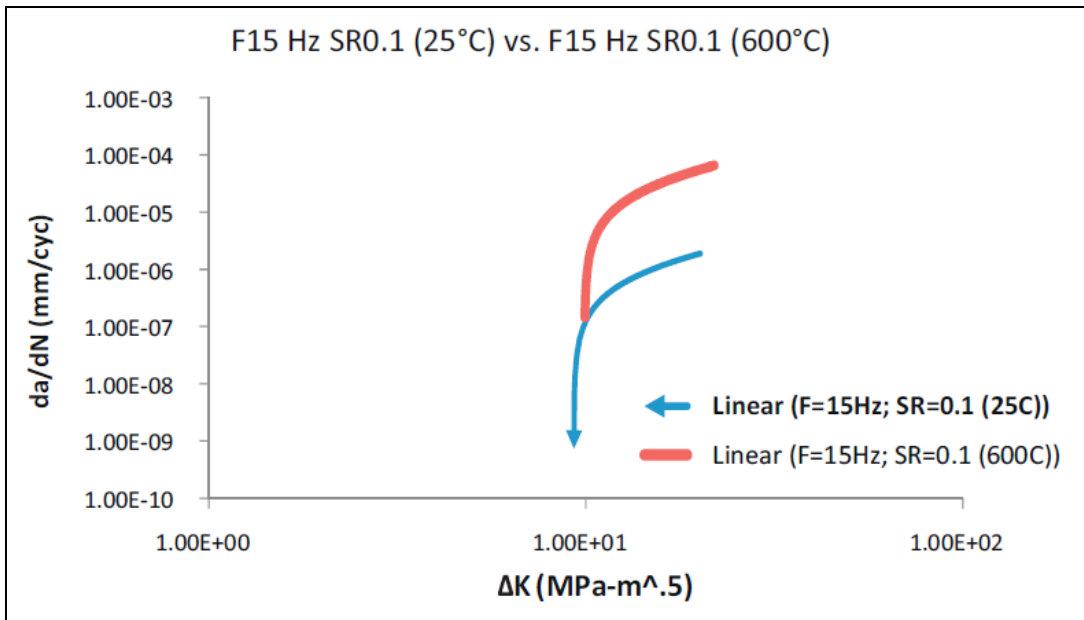


Figure 38 - FCG rates of H282 found by Buckson and Ojo at 15 hz Reprinted with permission of Elsevier publishing [100].

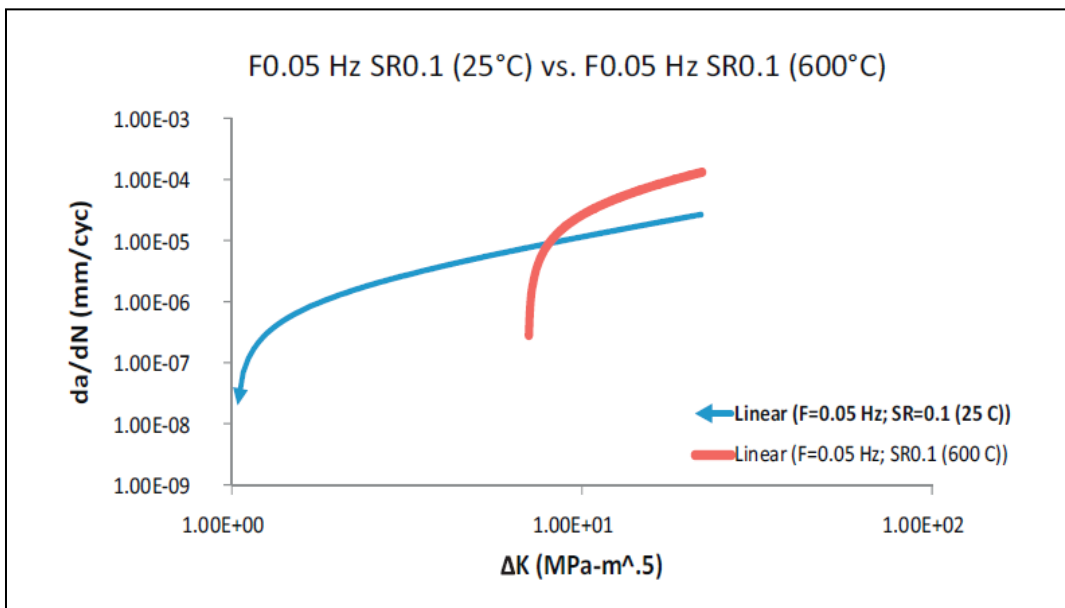


Figure 39 - FCG rates of H282 found by Buckson and Ojo at 0.05 hz Reprinted with permission of Elsevier publishing [100].

Fracture surfaces shown by Buckson and Ojo are intergranular at room temperature, and transgranular at 600°C. Buckson and Ojo did not give stress intensity ranges associated with the fracture surfaces and offered no explanation as to why the fracture surfaces change with temperature.

2.5 Summary of literature regarding Haynes 282.

The literature review has shown the following:

- a) Thermo-Calc results show a small predicted presence of detrimental sigma phase
- b) Yield strength is insensitive to over aging
- c) LCF is also insensitive to over aging
- d) Long term creep is insensitive to microstructure as the majority of aging is completed in 200 hours
- e) Oxidation activation energy was estimated near 120 kJ/mol for temperatures higher than 817°C

Microstructural insensitivity is desirable as turbine alloys are subject to 100,000 hour service life near ageing temperatures. This indicates Haynes 282 as a good candidate for rotor alloys. However, lacking in the literature is a study on the fatigue crack growth and fatigue mechanisms active in Haynes 282 at temperatures greater than 600°C.

3. Problem statement

In order to raise steam inlet temperature and pressure for land based steam turbine power plants, nickel base super alloys are being investigated for usage in said power plants. Design requirements dictate the material to have a minimum yield strength of 400 MPa and minimum creep rupture strength of 100 MPa after 100,000 hours of service, both at 760°C. Due to the long timeframe these alloys must endure, it is imperative to understand the alloy from multiple angles such as microstructural stability, deformation mechanism, creep behavior and fatigue behavior. Hawk, et al. [104], Pike [4] [102] [101] [103], Buckson and Ojo [100], and Boehlert and Loganbach [105] have gathered information on Haynes 282 regarding microstructural stability, low cycle fatigue, thermal conductivity, and creep deformation.

This thesis aims to compliment other author's work on Haynes 282 and add a perspective on the elevated temperature fatigue crack growth behavior of Haynes 282, for use in a steam turbine rotor. Areas explored will be fatigue crack growth rates, thermal activation energy, fractography, and active deformation mechanisms at or near the target service temperatures for advanced ultra-supercritical steam turbine rotors of 760°C.

4. Material and methods

In this section discussed is the chosen material and experimental procedure to gather FCG curves, images of the fracture surfaces, images of the microstructure ahead of the crack tip, activation energy and uncertainty related to the activation energy.

4.1 Haynes 282

The chosen alloy of investigation was Haynes 282 which is a NBSA developed at Haynes International with intention for use in A-USC steam turbine generators. Haynes 282 is a precipitate hardened nickel based superalloy, developed for high temperature structural applications such as turbine rotors [4].

Haynes 282 has the following chemistry, see Table 6.

Alloy (weight %)	Ni	Cr	Co	Mo	Ti	Al	Fe	Mn	Si	C	B
Haynes 282	57	19.5	10	8.5	2.1	1.5	1.5	0.3	0.15	0.06	0.005

Table 6 - composition of Haynes 282 [4].

The microstructure of Haynes 282 has ASTM grain size 4 (~91 μm in size), and gamma prime precipitates ~20 to 50 nm in diameter, in the peak aged state, see Figure 40. No secondary or tertiary gamma prime is present in Haynes 282.

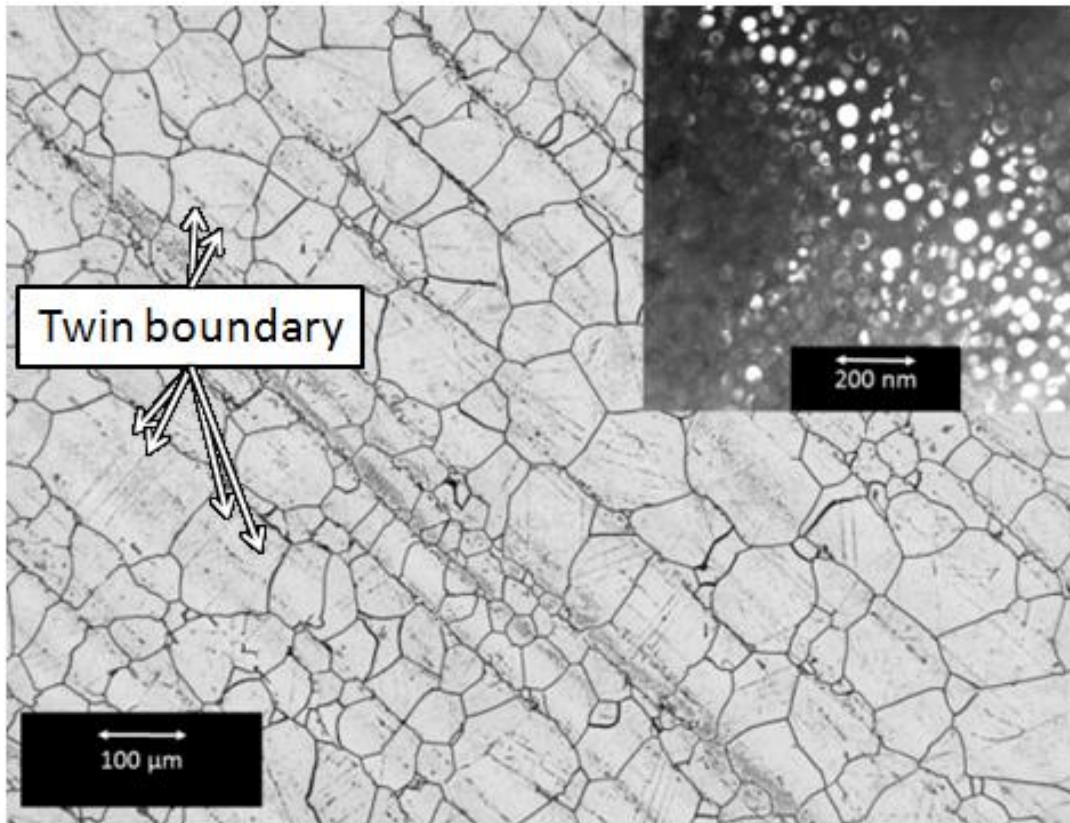


Figure 40– Microstructure of Haynes 282 in peak aged state with ASTM grain size 4. Inset: TEM image of gamma prime also in peak age state, from deformed material.

Mechanical properties of Haynes 282 are presented in Table 7 [4]. As typical of gamma prime precipitate hardened NBSAs Haynes 282 has a flat yield stress curve with respect to temperature up to around 760°C, where yield stress drops sharply.

T [°C]	E [GPa]	σ_y [MPa]
538	188	649
649	180	643
705	176	650
760	171	629

Table 7 - Mechanical properties of Haynes 282 over 540°C to 750°C from [4].

4.2 Experimental Methods

The following section outlines the specific details of experimentation.

4.2.1 Experimental method

The chosen experimental method was ASTM standard E647 “Standard Test Method for Measurement of Fatigue Crack Growth Rates” [108] as it is the industry and scientific standard for studying fatigue crack growth in materials. Any solid material may be tested by this method, and it is limited only by yield strength and buckling.

ASTM E647 covers the determination of FCG rates from near-threshold to K_{\max} controlled instability. Results are expressed in terms of crack-tip stress intensity factor range. Plotting in this way provides data that is independent of geometry, thus enabling direct comparison of data from a variety of specimen configurations and loading conditions.

Some thickness effects have been reported in the literature. However, the influence of thickness is mixed, with some studies claiming FCG is increased while others claim it is lowered, still others claim no effect on FCG as sample thickness is increased [108].

Some other potential error sources arising from this method are residual stress, crack closure and crack bridging. Residual stresses occur from plastic deformation. Residual stresses may cause increased or decreased stress intensity at the crack tip. Crack closure is the phenomenon where the crack remains in the closed position even though an external tensile force is applied to the specimen. Crack closure is typically caused by an oxide flake or a very tortuous crack path. Crack bridging is where ligaments span the crack behind the crack tip, frequently happening in fiber reinforced materials. Crack bridging and crack closure act to reduce the stress intensity felt at the crack tip.

4.2.1.1 Sample manufacturing procedure

FCG samples were machined from the peak aged plate received by Hawk (as described in 2.1 Thermal exposure effects of Haynes 282), in the short transverse (S-T) direction, see Figure 41. The C(T) specimen nominal dimensions were: width of $W = 25.4\text{mm}$ and nominal thickness of $B = 6.4\text{mm}$, see Figure 42.

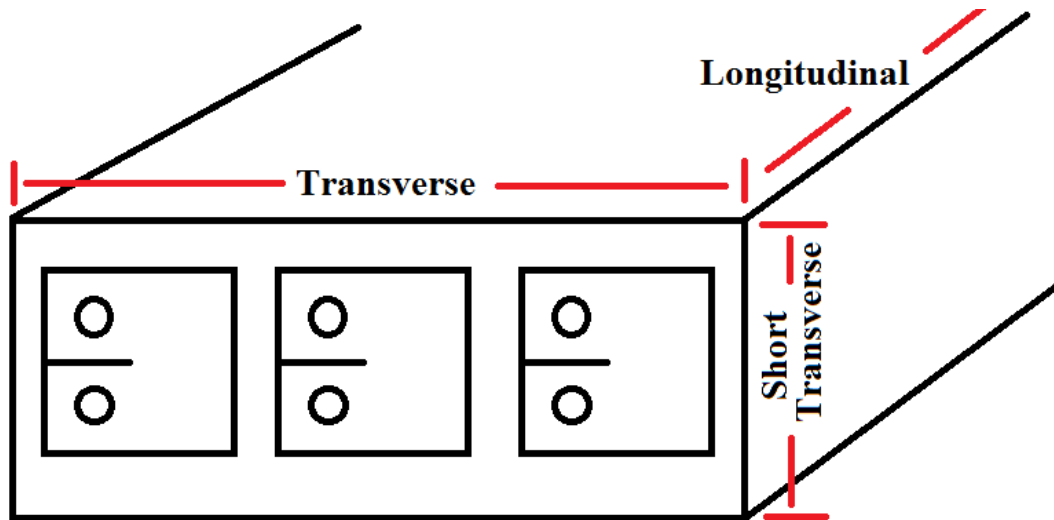


Figure 41 – Schematic of samples cut in the S-T direction.

4.2.1.2 Measuring crack length

There are many ways to measure crack length. One may glue a strain gauge to the back of a sample and measure strain. Or one may machine notches on the front of the sample to insert an extensometer, to measure the crack tip opening displacement. Lastly one may pass electric current through the sample and measure the change in voltage as the crack propagates through the sample.

At high temperature crack measurement methods are more limited. Strain gauges will burn off at high temperatures. This limits crack measurement methods to extensometer and voltage potential difference methods.

Direct current potential drop (DCPD) methodology was used to monitor crack length. The DCPD method was chosen because it is the simplest way to measure crack length at high temperature. Current leads were attached by screws at the geometric center of the sample on top and bottom faces while voltage leads were screwed into the front face above and below the notch (Figure 42). Screw size was 6x32 ANSI, with material of stainless steel.

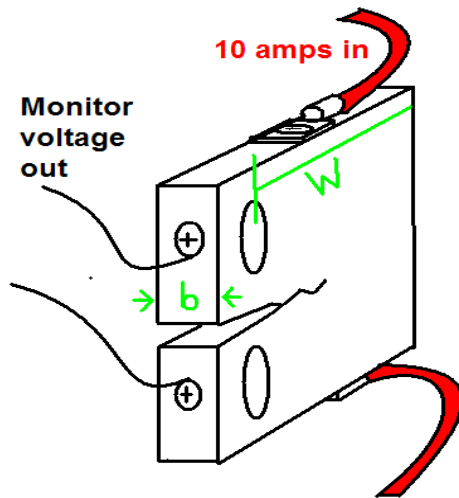


Figure 42 - Schematic of the DCPD setup on the C(T) sample. Sample width 'B' is 6.4 mm while sample width 'W' is 25.4 mm.

All electrical surfaces (including sample faces) were polished to 240 grit and wiped with acetone soaked cloth prior to testing. Current leads were observed to last for ~ 15 heat cycles, and were subsequently cut and remounted to the ring type washer current lead. Voltage leads lasted ~10 heat cycles, and were subsequently cut to a length where they were uncorroded. Thermocouples lasted ~10 heat cycles as well, and were subsequently and rewelded together in an area without corrosion damage.

A constant current DC power supply was used to supply 10 amps of current to the sample. Pure nickel wires ~0.06 mm diameter were chosen as the voltage leads. Stranded gauge 10 copper wire insulated for high temperature application was chosen as current leads. A ring and spade type connector was used to attach the current lead to the sample.

Crack length was acquired in real time by relating the voltage to the crack length by Equation 12. As current and voltage leads were not at ASTM E647 standard positions, a custom relation to a/w to voltage was generated. The a/w to voltage relation was gathered by cracking a sacrificial sample to various crack lengths and measuring the voltage at those crack lengths.

$$\text{A) } \alpha = 3.446 * 10^{-3}V^3 - 6.149 * 10^{-2}V^2 + 4.543 * 10^{-1}V - 4.629 * 10^{-1}$$

$$\text{B) } V = 2.219 * 10^{-1} \alpha^3 + 6.966\alpha^2 - 4.216 * 10^{-1} \alpha + 1.784$$

Equation 12 – Voltage to α relations. A) Voltage to alpha relation B) Alpha to voltage relation. Where: ' α ' is the instantaneous crack length divided by W , the sample width and ' V ' is the instantaneous voltage, in millivolts.

Crack length was correlated to stress intensity via Equation 13 from ASTM E647 [109].

$$\Delta K = \frac{\Delta P}{B\sqrt{W}} \frac{2 + \alpha}{(1 - \alpha)^{3/2}} (0.866 + 4.64\alpha - 13.32\alpha^2 + 14.72\alpha^3 - 5.6\alpha^4)$$

Equation 13 - Stress intensity calculation as a function of α . Where, ' P ' is the load, ' B ' is the C(T) sample thickness, ' W ' is the C(T) sample width, ' α ' is the instantaneous crack length divided by W .

The uncertainty of ΔK was determined to be 0.1 MPa \sqrt{m} by calculating the standard deviation of the stress intensity range over the 250 μm increment of crack growth that corresponded to the amount of growth used to calculate each crack growth rate.

4.2.1.3 Heating procedure

Heating was accomplished via an induction furnace in laboratory air. A K-type thermocouple was attached to the rear face away from stress zones, monitoring temperature. Selected temperatures were 550°C, 650°C and 750°C maintained to $\pm 3^\circ\text{C}$. To verify the induction coil design provided uniform heating, a separate dummy sample was utilized with three thermocouples spaced along the crack path at α of 0.25, 0.5 and 0.75.

4.2.1.4 Precracking procedure

Specimens were notched to 6 mm in two stages, i) 1mm thick abrasive cut off wheel was used to 5.5 mm in depth ii) 0.06 mm thick diamond blade was used to cut to the final depth of 6 mm.

Prior to fatigue testing and precracking, each sample was polished from 120 grit down to 1200 grit. Polishing assisted visual crack inspection, which was done before and after each test.

Specimens were precracked in two stages. I) At room temperature a stress intensity of $18.5 \text{ MPa}\sqrt{\text{m}}$ was applied until the crack was grown 0.5 mm from the machined notch. II) Sample temperature was raised to 650°C or 550°C and a decreasing ΔK (load shedding) experiment was conducted using a constant normalized ΔK gradient of $C_{LS} = -0.240 \text{ mm}^{-1}$ (See Equation 14 for definition of load shedding constant) with an initial stress intensity range of $14 \text{ MPa}\sqrt{\text{m}}$ and final stress intensity range of about $7 \text{ MPa}\sqrt{\text{m}}$. Final precracking crack length varied from about 8 to 11 mm. A sinusoidal waveform at 25 Hz was selected for both stages of precracking. Data was collected in increments of 1×10^{-5} m of crack extension.

$$C_{LS} = \left(1/K_i\right) \left(dK/da\right)$$

Equation 14 - Formula for load shedding constant calculation. Where: 'C' is the load shedding constant, 'K_i' is the initial stress intensity, 'dK' is the change in stress intensity, 'da' is the change in crack length.

Short cracks are well known to grow at faster rates than long cracks [5] [109] [110]. Note that samples were notched to an initial crack length ~ 6 mm. Subsequent room temperature precracking was stopped at a crack length ~ 6.5 to 7 mm. It is important to grow cracks at least twice the distance of the thickness of the blade to avoid influence from the blade thickness. With a blade thickness of 0.06 mm no influence from the blade is expected, as samples were grown a minimum of eight times the blade thickness. High temperature precracking ($C_{LS} = -240 \text{ mm}^{-1}$) ended between 8 and 11 mm. With a grain size of 0.1 mm, cracks are microstructurally long and no influence from short cracks are expected.

The two stage precracking procedure was necessary as cracks were not observed to grow at high temperatures and low stress intensity ranges with a room temperature precrack created using a ΔK value of $18.5 \text{ MPa}\sqrt{\text{m}}$.

4.2.1.5 Fatigue crack growth procedure

Fatigue crack growth experiments were done in general accordance with ASTM standard E647 [108]. Compact tension, C(T) specimens were selected to minimize the amount of physical material needed for experimentation.

A 250 kN capacity servo-hydraulic MTS load frame was used with a 25 kN load cell. The selected loading frequencies were 25 Hz and 0.25 Hz. At 0.25 Hz a triangular waveform was used to keep strain rates constant, while at 25 Hz a sinusoidal waveform was selected as a triangular waveform was not obtainable at 25 Hz. The selected ratio of minimum to maximum load, $R = P_{\min}/P_{\max}$, was 0.1. Load control was selected as the loading method because constant position control leads to a drop in the applied stress intensity range as the crack advances.

Prior to high temperature experiments (both precracking and data collection), samples were held at the testing temperature for 24 hours. During this 24 hour period, samples were loaded to cyclic stress intensity range of 2-3 MPa \sqrt{m} . This was done to minimize voltage drift and thermocouple effects and temperature fluctuations. Typically the voltage drift waned after ~ 12 hours and sample temperature stopped drifting after 4 hours. After 4 hours, the nanovolt meter was zeroed to mitigate the thermocouple effect at the voltage leads.

FCG data was collected via constant load amplitude and load shedding tests. Regarding the constant load amplitude tests, for tests done at 25 Hz the stress intensity range began around ΔK of 9 MPa \sqrt{m} and concluded around ΔK of 25 MPa \sqrt{m} . At 0.25 Hz the stress intensity range began around ΔK of 11 MPa \sqrt{m} and concluded around ΔK of 37 MPa \sqrt{m} . Cycle number, instantaneous crack length, peak load, minimum load, stress intensity, load ratio, frequency, reference voltage, instantaneous voltage, and time stamp was collected in increments of 1×10^{-5} m of crack extension. The first 250 μm of crack growth were discarded from analysis for each experiment due to the influence of the precrack.

Due to the prior stress influence, testing of da/dN below 10^{-8} m/cycle is recommended via load shedding technique with a load shedding constant of $C_{LS} = -0.08 \text{ mm}^{-1}$. A load

shedding experiment was done both at 650 and 550°C at 25 Hz with a load shedding constant of -0.08 mm^{-1} . A comparison with the precracking data ($C=-0.240 \text{ mm}^{-1}$) showed data overlapping from ΔK of $6.5 \text{ MPa}\sqrt{\text{m}}$ to ΔK of $14 \text{ MPa}\sqrt{\text{m}}$ for 650°C and ΔK of $10 \text{ MPa}\sqrt{\text{m}}$ to ΔK of $14 \text{ MPa}\sqrt{\text{m}}$ for 550°C, both at 25 Hz loading frequency. Therefore, it was determined the data collected under a C_{LS} of -0.240 mm^{-1} was equivalent to C_{LS} of -0.08 mm^{-1} and all further data was gathered with a C_{LS} of -0.240 mm^{-1} . The FCG curves were gathered in the following manner:

25 Hz:

$\Delta K > 10 \text{ MPa}\sqrt{\text{m}}$, constant load

$\Delta K < 10 \text{ MPa}\sqrt{\text{m}}$, load shedding, $C_{LS} = -0.240 \text{ mm}^{-1}$

0.25 Hz:

$\Delta K > 12 \text{ MPa}\sqrt{\text{m}}$, constant load

$\Delta K < 12 \text{ MPa}\sqrt{\text{m}}$, load shedding, $C_{LS} = -0.240 \text{ mm}^{-1}$

After FCG experiments were completed, unbroken samples were cracked in half for analysis. Cracking procedure varied from cycling at constant load at room temperature at 25 hz, to cycling at high temperatures and low frequencies. A final crack length was measured at $1/4$, $1/2$ and $3/4$ of the sample thickness, B, and averaged, from the broken samples. It is important to measure the final crack length through the sample thickness as the crack front may bow. Any differences between the final computer interpreted crack length and the actual crack length were corrected by assuming the error accumulated linearly with crack extension (Equation 15). Each crack growth rate data point (da/dN), was determined from a fit of $250\mu\text{m}$ of crack growth, with each data point (plotted) having 50% overlap of the neighboring growth increment.

$$a_{corrected} = a_{initial} + \frac{(b_{instant} - b_{initial})(a_{final} - a_{initial})}{b_{final} - b_{initial}}$$

Equation 15 - Crack length correction equation. Where: 'a_{initial}' is the initial crack length measured by microscope, 'b_{instant}' is the instantaneous crack length measured by the computer, 'b_{initial}' is the initial crack length measured by computer, 'a_{final}' is the final crack length measured by microscope, 'b_{final}' is the final crack length measured by computer.

A few samples fractured unexpectedly and the final crack length was investigated in the SEM. An approximate final crack length was calculated based off measurements of where the onset of ductile fracture mechanism was observed at 1/4, 1/2 and 3/4 thickness.

4.2.2 Fractography procedure

Fracture surfaces were investigated in a standard SEM from FEI Company. Compressed air was used to dust off fracture surfaces. Images were taken using secondary electrons. Stress intensities for each observed location were determined based off the coordinates of the images and the crack length data file.

Image locations were selected periodically, with an approximate interval of 0.5mm between images. Image magnification was selected at 100x, 400x, 1600x and 6000x. The author has selectively presented images to show specific features relevant to crack growth mechanisms.

4.2.3 TEM sample procedure

Samples for the TEM analysis were cracked at a constant ΔK for a minimum of 3 mm at 550°C, 650°C and 750°C at both 25 Hz and 0.25 Hz. A constant ΔK for multiple millimeters was necessary to achieve a uniform deformation pattern representative of the selected stress intensity range.

Samples at 25 Hz were cracked at ΔK of 9 ±1 MPa√m, while samples at 0.25 Hz were cracked at ΔK of 15 ±1 MPa√m. To achieve a consistent sample surface, both sides of the C(T) sample were polished at 240, 400, 600, 800 and 1200 grit papers, under wet conditions. Samples for the TEM were milled using the gallium focused ion beam (FIB) in a dual beam FIB/SEM. Samples approximately 10 μm by 5 μm and 1 μm thick were

cut inside the plastic zone just ahead of the crack tip, parallel to the crack tip (Figure 43). Thinning was done at 30 KV, with a final polish at 5KV. Final samples were electron transparent at around 100 nm thickness.

The FIB method for TEM samples was selected to guarantee TEM images in the plastic zone. The alternate method of cutting 3 mm disk will not provide sufficient geometric accuracy for TEM samples, as target plastic zone sizes were as small as 60 μm .

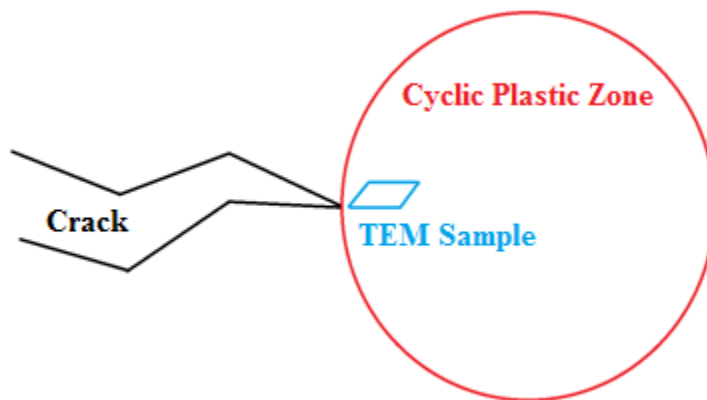


Figure 43 – Schematic of TEM sample extraction.

4.3 Uncertainty in FCG rates

The FCG curves were calculated by plotting the change in crack length (over 250 μm of crack length) per accumulated cycles against the stress intensity (which is a function of crack length). There is an uncertainty in the crack length but not in cycle count as cycle count is absolute. Crack length was calculated from the voltage via Equation 12, p61. Uncertainty in the crack length will be related to measuring the instantaneous voltage. Stress intensity range was calculated from Equation 13, p61. The uncertainty of the stress intensity will be related to the uncertainty in measuring the voltage and load.

Uncertainty will arise from a variety of sources. The uncertainty arising in calculating the crack length is as follows:

- 1) The power supply will have some intrinsic drift or fluctuation. Voltage drift can give false crack length input to software. Also at low crack growth rates, voltage

drift over time is faster than the FCG rate. This will lead to false crack growth rates. Also the Nanovolt meter has an associated uncertainty.

2) The thermocouple effect between dissimilar metals may cause temperature fluctuations to artificially increase or decrease the measured voltage, which will induce errors in crack length. Voltage leads were 99.5% nickel wire, while Haynes 282 is 57% nickel.

3) There is uncertainty in the a to voltage relation.

4) The final crack length measured off the fractured sample deviated from the final crack length calculated from Equation 12, p61.

Points 1 to 4 are accounted for below:

Regarding point 1, FCG rates were measured above where such an influence would introduce uncertainty. For 0.25 Hz this was 10^{-8} m/cycle and for 25 Hz minimum FCG rate was 10^{-10} m/cycle. The minimum cycle rates were based on a measured average voltage drift of 0.2 mV/hr. Uncertainty in the nanovolt meter is 100×10^{-9} V. This leads to a crack length uncertainty of $\sim 0.01\%$. The uncertainty in the power supply is $\pm 0.1\%$. This leads to an uncertainty in crack length of 0.23%. With crack length uncertainty averaging around 3% the uncertainty due to the nanovolt meter and power supply can be ignored. The uncertainty in the crack length was found from the 'linest' function in excel when gathering the linear fit over the 250 μm crack length interval.

Regarding point 2, any small fluctuations in temperature which would cause scatter in the crack length (due to thermocouple effect) would be included in the uncertainty of the growth rate described below (point 3).

Regarding point 3, this uncertainty is assumed to be averaged out over the 250 μm of crack length used to fit a crack growth rate. The combined furnace, power supply and nanovolt uncertainty was measured at 8.6 μV over all samples. Propagation of this error using realistic values of raw voltage (2.3 to 7.5 mV) and crack lengths (8mm to 21mm), are calculated to produce a maximum 1% uncertainty in crack length for $a < 8\text{mm}$ and for

a=20mm uncertainty in crack length was 0.2%. With crack length uncertainty averaged at ~3% the uncertainty due to the polynomial fit is accounted for.

Regarding point 4, crack length errors were observed to be a maximum 7.5% longer or shorter; with average error was 2.9%. Crack lengths tended to be underestimated for $\alpha < 0.5$ and shorter. At higher α values, crack lengths were both overestimated and underestimated. Equation 15 is assumed to account for this up to 7.5% error in crack length. Crack length errors are listed in Appendix I: Sample parameters, p130.

The uncertainty arising from calculating the crack growth rate is as follows:

- 1) To calculate the FCG rate, a linear fit between 250 μm of crack length and cycles was calculated. This fit will contain an uncertainty in slope.
- 2) The stress intensity was averaged over this 250 μm of crack length used to fit a crack growth rate.

Points 1 and 2 are accounted for below:

Regarding point 1, the uncertainty in the slope averaged at 3% for constant load tests. Uncertainty in slope was calculated via the 'linest' function from Excel. Load shedding tests had a maximum uncertainty of 18%. Load shedding tests were not analyzed for activation energy, therefore further discussion on uncertainty from load shedding tests is ignored. Note there is no uncertainty from cycles as cycle count is an absolute integer.

Regarding point 2, the standard deviation of ΔK averaged around 0.1 $\text{MPa}\sqrt{\text{m}}$ for all samples.

The uncertainty arising in calculating the applied stress intensity range is as follows:

- 1) The load cell had a accuracy of $\pm 0.5\%$.

Point 1 is accounted for below:

Regarding point 1, the uncertainty due to load cell accuracies would affect ΔP , the applied load in Equation 13, p61. The uncertainty in stress intensity due to 0.5% accuracy is calculated to effect ΔK depending on crack length. For crack lengths at 10mm the uncertainty in ΔK is 0.03 MPa \sqrt{m} , while at longer crack lengths (~20mm) the uncertainty in ΔK is 0.1 MPa \sqrt{m} for a realistic load range of 1000-100N. With the standard deviation of ΔK found to be 0.1 MPa \sqrt{m} , this uncertainty is accounted for.

4.4 Activation energy calculation

To find the activation energy, Q , based on FCG curves, one considers the process to be dominated by thermally activated mechanisms [91] such that the crack growth rate is proportional to an Arrhenius relation, Equation 16.

$$da/dN \propto kf(a) \exp\left(-Q/R_g T\right)$$

Equation 16 – Activation energy relation. Where: 'da/dN' is the rate of transformation, 'kf(a)' is a function containing all terms independent of 'T', 'Q' is the activation energy, 'R_g' is the gas constant and 'T' is the temperature.

For Equation 16 to be valid one must compare the fatigue data such that the only variable is temperature. This means that waveform, load ratio, stress intensity, cracking mode etc. must be the same. Recall from 1.6 Fatigue crack growth, p25 there is a threshold, Paris and final fracture regions of FCG. Stress intensities must be chosen to come from the same region as different fatigue mechanisms are active in the three different regions of the FCG curves.

Taking the natural logarithm of Equation 16 and slight rearranging, one may linearize the equation:

$$\ln\left(\frac{da}{dN}\right) = \left(\frac{-Q}{R_g}\right) 1/T + \ln C$$

Equation 17 - Linearization of Equation 16.

The FCG rates were plotted $\ln(da/dN)$ against $1/T$ and for ΔK intervals of $1 \text{ MPa}\sqrt{\text{m}}$. A linear fit was used to find Q utilizing Equation 17. Only data gathered from constant load experiments were analyzed for activation energy.

4.5 Uncertainty in activation energy

The uncertainty arising from calculating the activation energy is as follows:

1) Stress intensity intervals used to calculate activation energy varied within 5% of each other.

2) Stage one to stage two crack growth occurs at different stress intensities at higher temperatures; therefore, a different cracking mechanism is active and temperature is not the only variable in Equation 16, p69.

3) Activation energy was calculated by plotting the natural logarithm of the FCG rate against inverted temperature. The activation energy was then related to the slope of the fit. This slope also has uncertainty which must be accounted for.

4) Induction furnace maintained sample temperature within $1\text{-}3^\circ\text{C}$

Points 1 to 4 are accounted for below:

Regarding point 1, The author assumes this uncertainty will be accounted for in point 3.

Regarding point 2, while a transition from stage one to stage two crack growth was observed, the influence on fatigue crack growth rate is negligible. Equation 16, p69 is assumed to be valid because the stage one to stage two crack mechanism shift does not adversely affect FCG rates.

Regarding point 3, the slope uncertainty for activation energy fit will be accounted for. The 'linest' function in excel will yield the uncertainty in slope for this measurement.

Regarding point 4, temperature is an input in the Arrhenius equation. The uncertainty is the standard deviation of the temperature fluctuation (typically 1 to 3°C , see

Appendix I: Sample parameters, p130).

4.6 Uncertainty in calculating the activation energy

To calculate the activation energy, a linear fit between the logarithm of the crack growth rate and inverted temperature was done at ΔK intervals of 1 MPa \sqrt{m} . To account for the error associated with the linear fit of the FCG data (Figure 44), the 'linest' function in excel utilized to find slope errors. In the subsequent section, this error is called 'fit' error. The The uncertainty due to the fit is listed as 'Err Q fit' in Table 10, p97 and Table 11, p98.

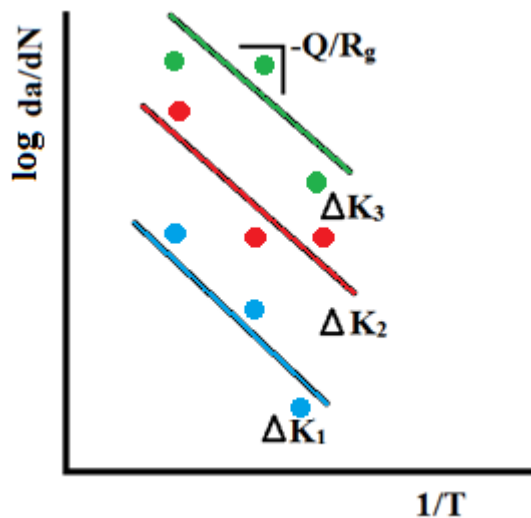


Figure 44 - Error sources accounted for via fit method.

4.7 Calculating experimental uncertainty

To estimate the uncertainty associated with the experimental setup an analysis from Taylor [111] was implemented. Taylor's method will account for the uncertainty in the crack length and temperature fluctuations. Figure 45 illustrates the errors accounted for Taylor's method.

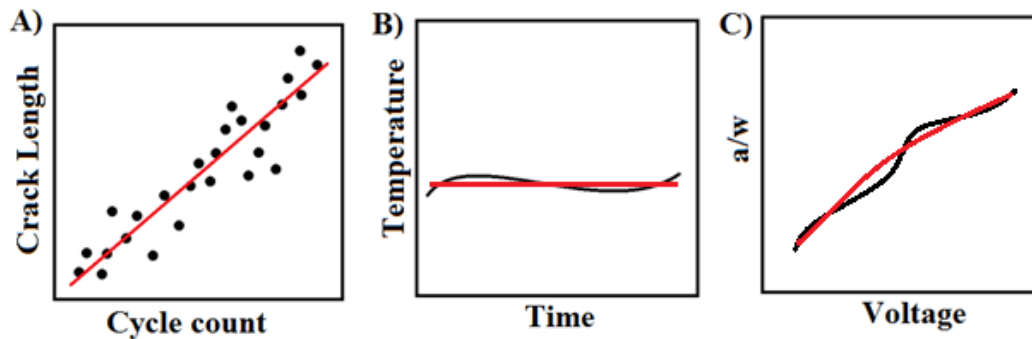


Figure 45 - Error sources accounted for via Taylor method, Black represents fluctuations, red represents average measurements. A) Slope error from raw data B) fluctuations in temperature, C) fluctuations in voltage effecting α (assumed to be accounted for in A).

Taylor suggested the uncertainty in a system with multiple independently measured variables is found by Equation 18.

$$\delta q = \sqrt{\left(\frac{\delta q}{\delta x_1} dx_1\right)^2 + \dots + \left(\frac{\delta q}{\delta x_n} dx_n\right)^2}$$

Equation 18 – Uncertainty in a function of several variables as found by Taylor [111].

The reason the quadrature method was chosen (Equation 18) was to avoid overestimating the uncertainty. Crack length is a function of voltage off the front face of the sample. There is a voltage drift associated with the power supply and a voltage drift associated with the furnace. The probability that the peak uncertainty of both are concurrent is low as the equipment is independent of each other. Being independent, it is highly improbable that peak uncertainty will occur simultaneously for both variables; therefore, a quadrature sum is more appropriate [111].

Solving Equation 17, p69 for Q,

$$Q = R_g T \ln C - R_g T \ln\left(\frac{da}{dN}\right)$$

Equation 19 - Equation 17 solved for Q.

Taking partial derivative of Equation 19 with respect to temperature,

$$\frac{\delta Q}{\delta T} = -R_g \ln\left(\frac{da}{dN}\right) + R_g \ln(C)$$

Equation 20 – Partial derivative of activation energy with respect to temperature.

Taking partial derivative of Equation 19 with respect to crack growth rate,

$$\frac{\delta Q}{\delta\left(\frac{da}{dN}\right)} = -R_g T / \left(\frac{da}{dN}\right)$$

Equation 21 - Partial derivative of activation energy with respect to crack growth rate.

Using Equation 18-Equation 21 one may calculate the uncertainty in the activation energy from data measurement. The associated errors for temperature and crack growth rate for each test was correlated to the reported stress intensity range. The observed standard deviation of temperature and slope uncertainty for crack growth rates is listed in,

Appendix I: Sample parameters, p130. On average da/dN error was 3% and standard deviation of temperature was around 1°C. Experimental uncertainty is listed as 'Err Q Taylor' in Table 10, p97 and Table 11, p98.

4.8 Total activation energy uncertainty

The fit method (4.6 Uncertainty in calculating the activation energy, p71) accounts for the uncertainty in the activation energy due to the linear fit. The Taylor method (4.7 Calculating experimental uncertainty, p71) accounts for the error due to the raw data uncertainty and temperature fluctuations. The two error sources were combined by taking a sum (Equation 22) to estimate the final activation energy uncertainty. The reason that summing the errors is appropriate here and not a quadrature sum is because the experimental error and the fit error are not independent as both uncertainties are functions of the crack length.

$$\Delta Q_{Tot} = \Delta Q_{Taylor} + \Delta Q_{fit}$$

Equation 22 - Equation used to sum uncertainty. Where: ' ΔQ_{tot} ' is the total uncertainty, ' ΔQ_{Taylor} ' is the experimental uncertainty, and ' ΔQ_{fit} ' is the uncertainty in the fit to the activation energy calculation.

5. Experimental Results

Utilizing ASTM E647 the FCG rates were gathered at 550, 650 and 750°C both at 25 Hz and 0.25 Hz loading frequencies. The data for Haynes 282 is presented in the following sections.

5.1 Fatigue crack growth rates

Figure 46 shows the FCG rates in the range of 550°C – 750°C at a cycle frequency of 25 Hz and Figure 47 shows them at 0.25 Hz.

For both frequencies tested, the FCG rates increase with increasing temperature. At 25 Hz loading frequency (Figure 46), the effect of temperature is to simply increase the FCG rates and shift the curves higher. The FCG curves at 0.25 Hz loading frequency (Figure 47) show a slope change at around $\Delta K = 17 \text{ MPa}\sqrt{\text{m}}$ for 650°C, as well as the 750°C data in a more subtle manner.

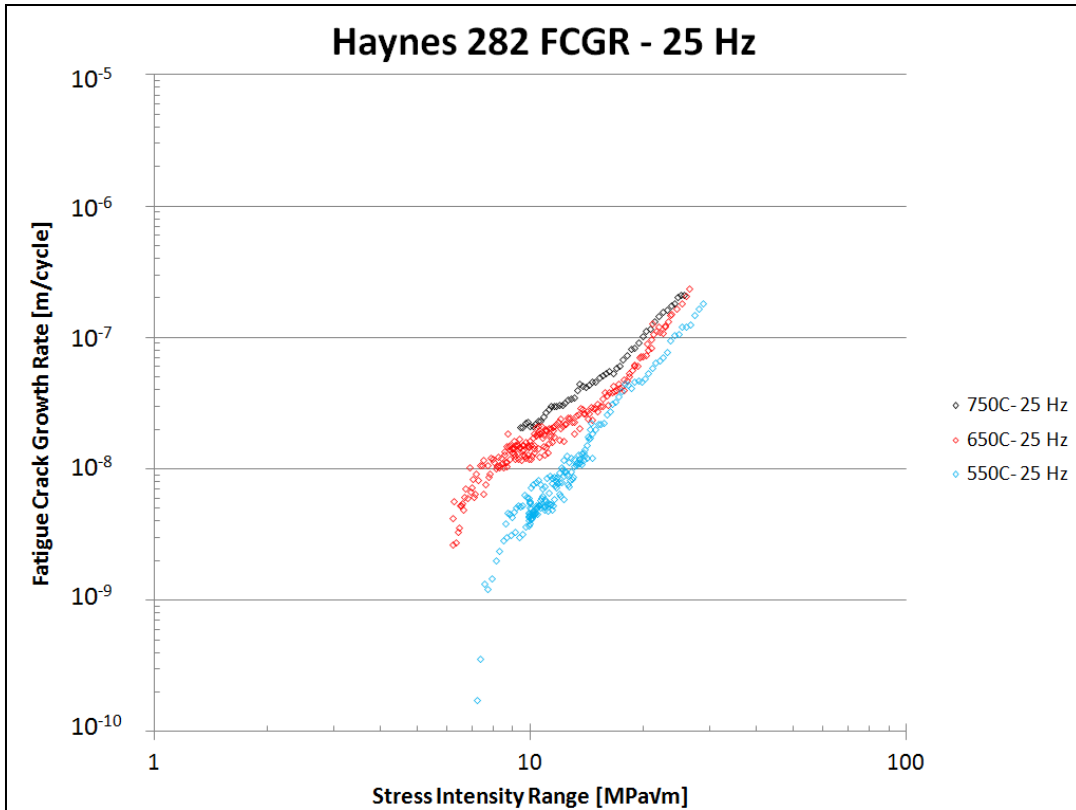


Figure 46- FCG of Haynes 282 at 25 Hz at 550°C (blue diamonds, bottom), 650°C (red diamonds, middle), and 750°C (black diamonds, top). Load ratio 0.1, waveform: sinusoidal.

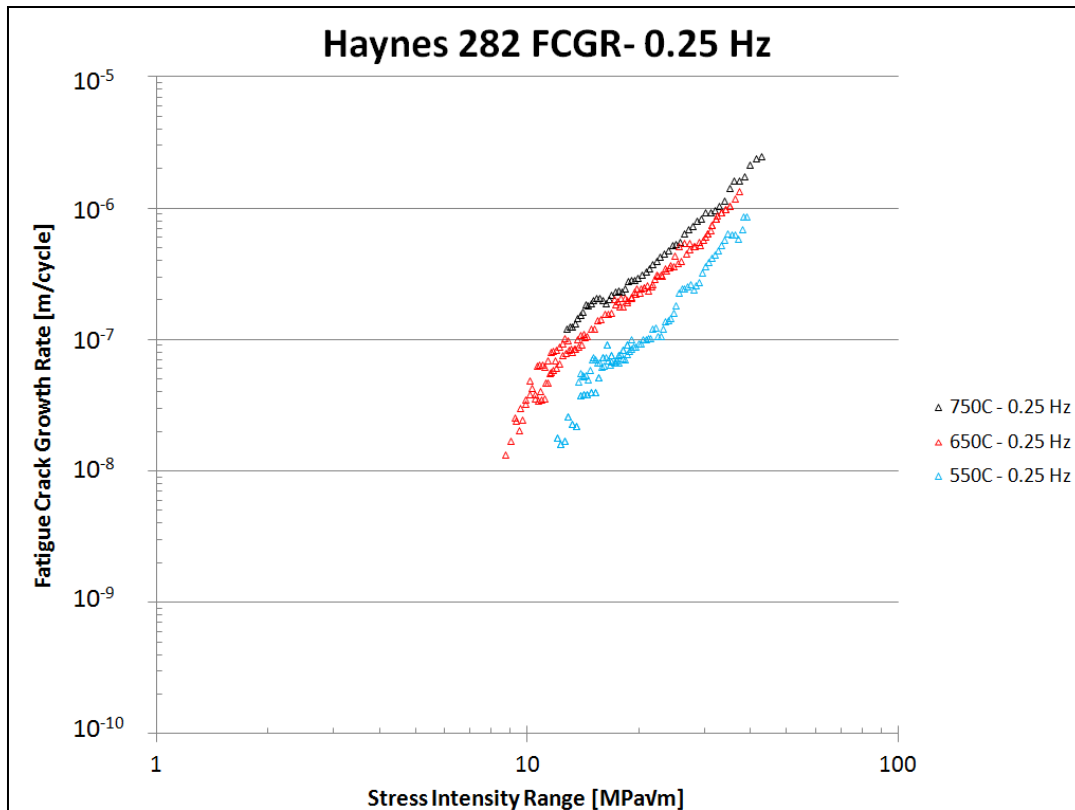


Figure 47- FCG of Haynes 282 0.25 Hz at 550°C (blue triangle, bottom), 650°C (red triangle, middle), and 750°C (black triangle, top). Load ratio 0.1, waveform: triangular.

5.1.1 Paris fit to FCG curves

Recall from section 1.6 Fatigue crack growth, p25 the Paris region of the FCG curves follow the Paris law (Equation 10, p26). Fitting the FCG data in Figure 46 and Figure 47 to an exponential function, one may find the Paris constants. Figure 48 to Figure 50 show the FCG curves at each temperature tested, with exponential fit to calculate Paris constants.

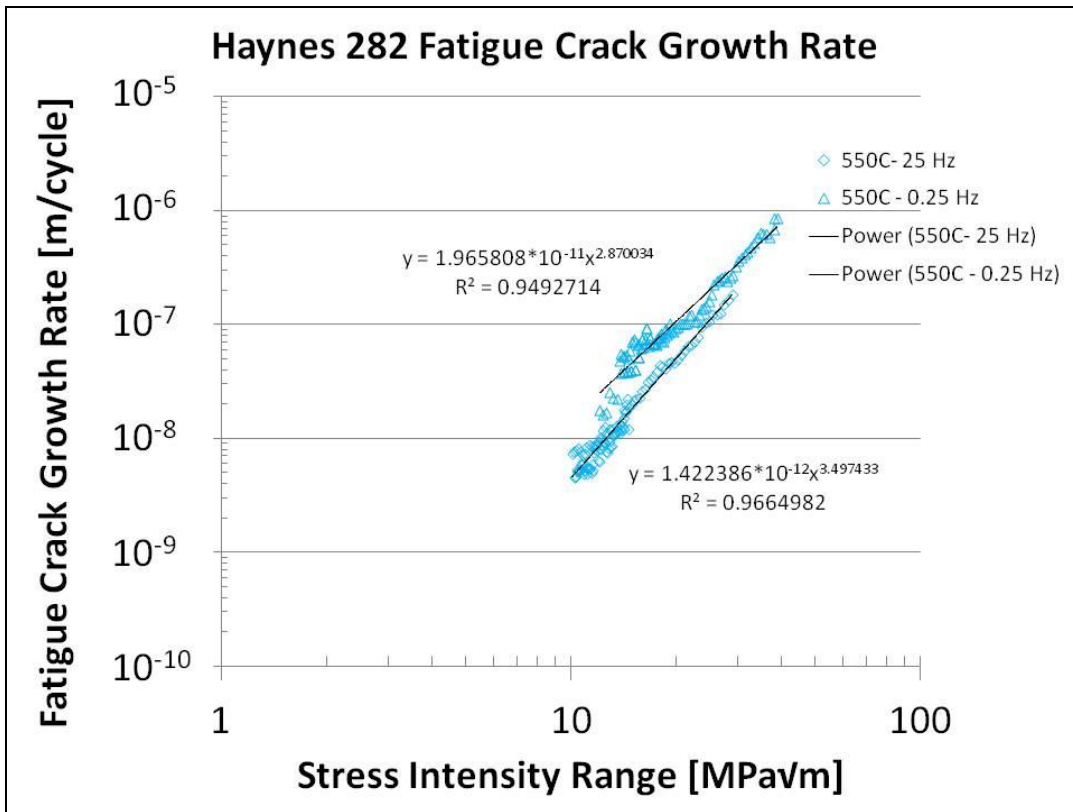


Figure 48 - FCG rates at 550°C isolated by loading frequency, with exponential trend line fit. The 0.25 Hz is upper curve and 25 Hz is lower curve.

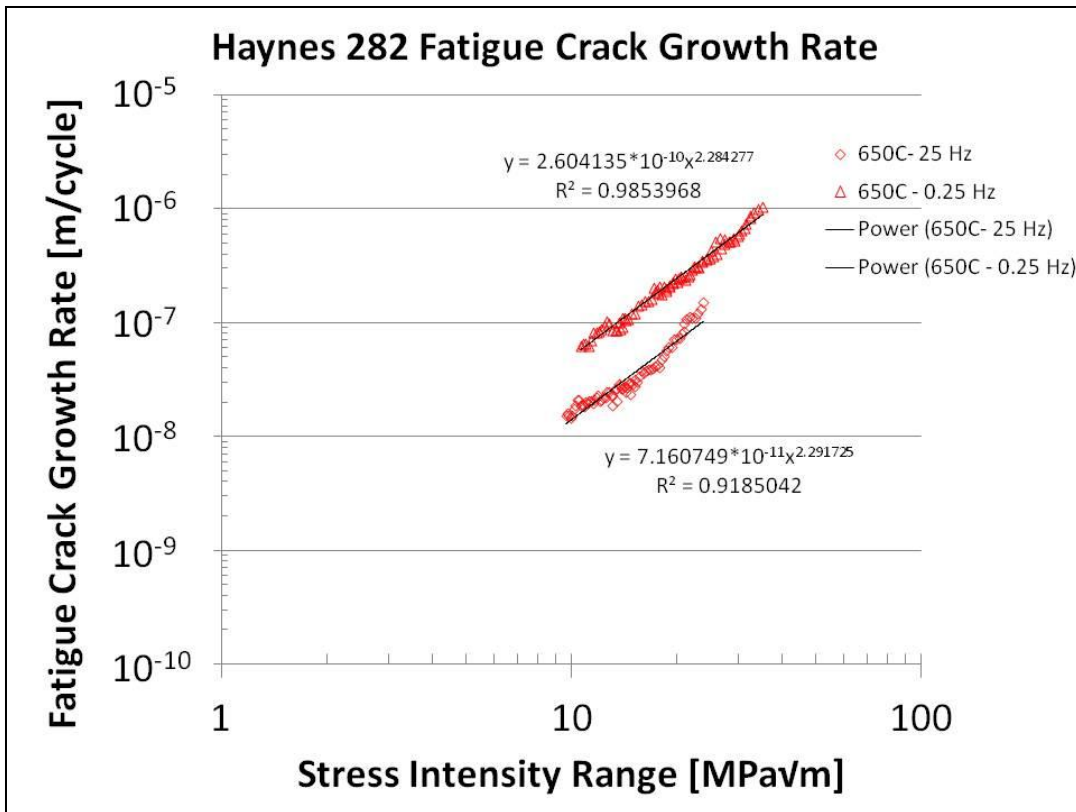


Figure 49 - FCG rates at 650°C isolated by loading frequency, with exponential trend line fit. The 0.25 Hz is upper curve and 25 Hz is lower curve.

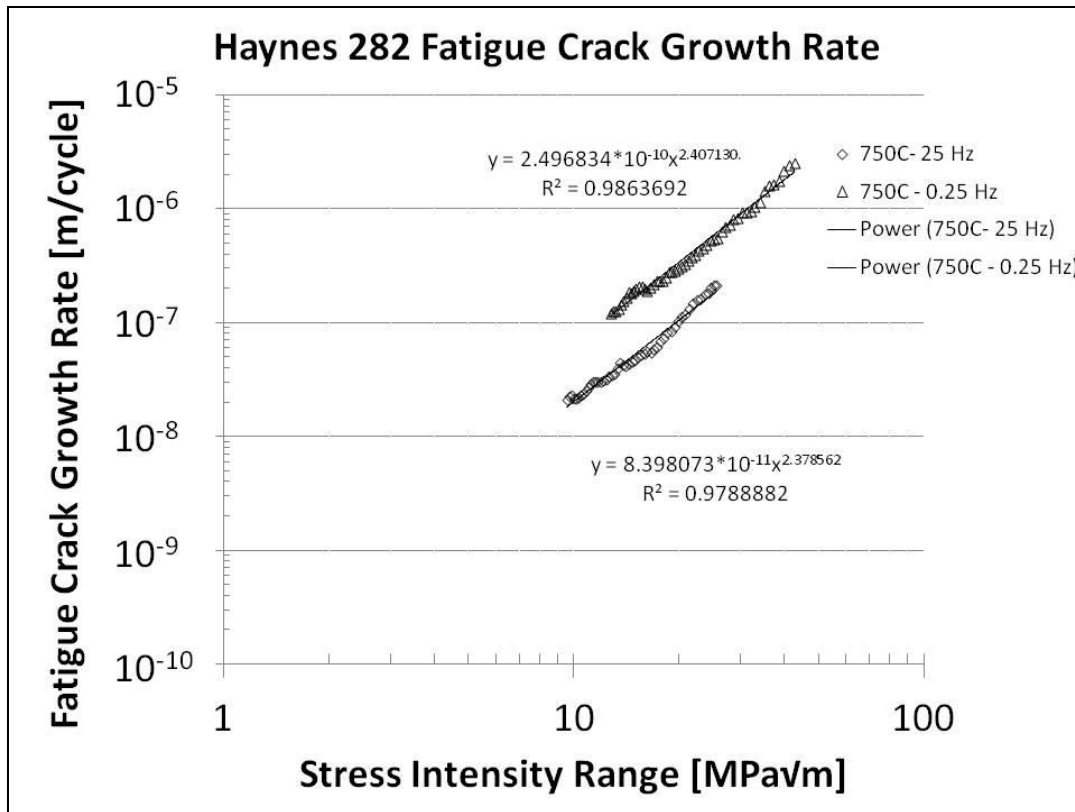


Figure 50 - FCG rates at 750°C isolated by loading frequency, with exponential trend line fit. The 0.25 Hz is upper curve and 25 Hz is lower curve.

The Paris constants for Figure 48 to Figure 50 are presented in Table 9 for 25 Hz loading frequency and for in Table 8 for 0.25 Hz loading frequency. The Paris constants at 25 Hz loading frequency were fit between, $9.6 < \Delta K < 17$, $17 < \Delta K < 24.7$ MPa√m for 750°C, $9.6 < \Delta K < 17$, $17 < \Delta K < 23.5$ MPa√m for 650°C, $10.3 < \Delta K < 28.9$ MPa√m for 550°C, for Table 9. As noted prior, the FCG rates at 650°C and 750°C at 25 Hz loading frequency showed a change in slope around $\Delta K = 17$ MPa√m (Figure 46). The Paris constants were therefore split at $\Delta K = 17$ MPa√m at 25 Hz for 750°C and 650°C.

The Paris constants at 0.25 Hz loading frequency were fit between $12.8 < \Delta K < 42.8$ MPa√m for 750°C, $10.6 < \Delta K < 34.1$ MPa√m for 650°C, $12.6 < \Delta K < 38.9$ MPa√m for 550°C for Table 8.

0.25 Hz	C_p	m
550°C	$1.966 \cdot 10^{-11}$	2.870
650°C	$2.604 \cdot 10^{-10}$	2.284
750°C	$2.497 \cdot 10^{-10}$	2.407

Table 8 - Paris constants at 0.25 Hz for each tested temperature.

Temperature	ΔK MPa \sqrt{m}	C	m
550°C	all	1.422E-12	3.497
650°C	<17	4.383E-10	1.580
650°C	>17	9.012E-13	3.778
750°C	<17	2.511E-10	1.937
750°C	>17	7.366E-12	3.185

Table 9 - Paris constants at 25 Hz for each tested temperature. Paris constants for 650°C and 750°C split at $\Delta K = 17$ MPa \sqrt{m} .

5.1.2 FCG of Haynes 282 relative to other NBSAs

Presented below are the FCG rates of Haynes 282 relative to other NBSAs. Figure 51 shows the FCG at frequencies of 2-25 Hz with sinusoidal waveforms. Figure 52 shows the FCG at frequencies from 0.05 to 0.33 Hz with triangular waveforms. Haynes 282 is observed to have the lowest FCG rates at 25 Hz. Conversely, Haynes 282 lies in the middle of the pack at 0.25 Hz. Inconel 718 is observed to perform the best at 0.25 Hz.

Waspaloy is a gamma prime strengthened super alloy of similar chemistry and higher volume fraction gamma prime of Haynes 282. Udimet 720 and 720li are also gamma prime strengthened alloys. U720/720li have higher volume fraction gamma prime relative to Haynes 282, however previous investigations have shown U720 unable to meet creep requirements for steam turbine rotor alloys [104]. Inconel 718 is a gamma double prime strengthened alloy, with an upper temperature limit around 700°C due to the gamma double prime instability at high temperatures. Inconel 718 is manufactured via hot isostatic pressing and used in turbine disks [112]. Inconel 100 is another gamma prime strengthen NBSA.

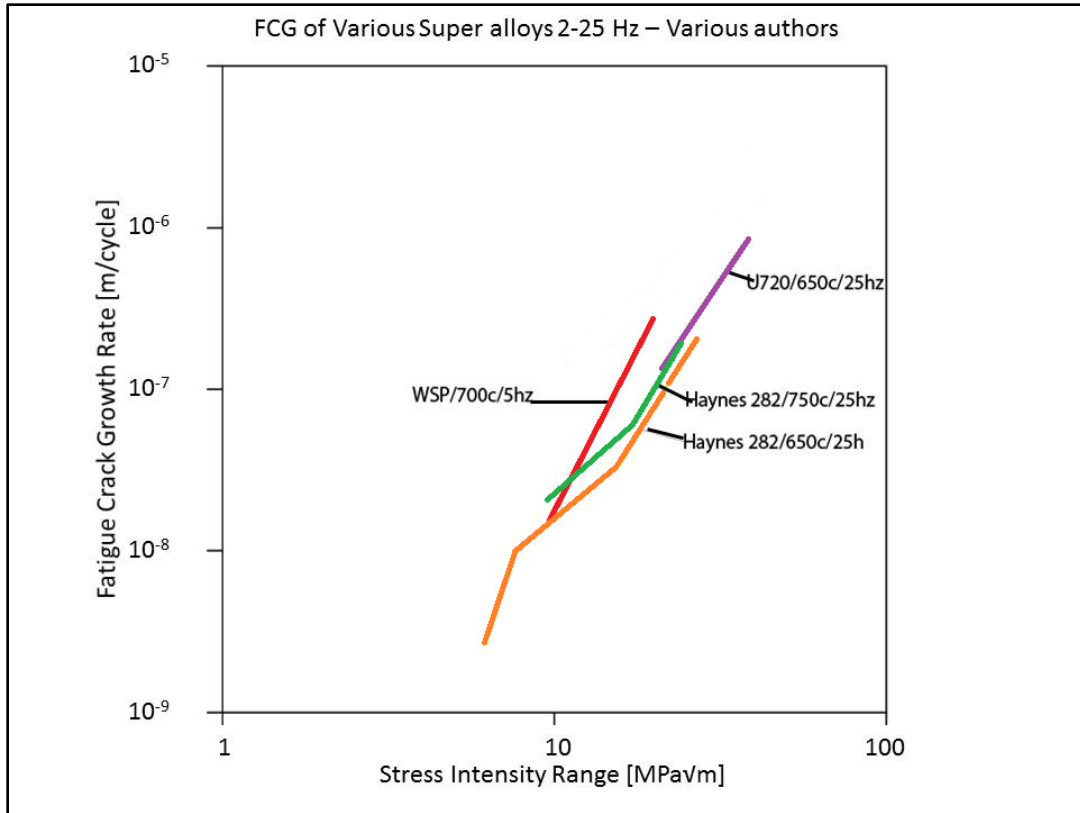


Figure 51 – FCG rates of various superalloys in temperature ranges between 650-760°C and frequencies of 2-25 Hz. WSP = Waspaloy [113], U720li = Udimet 720 low interstitial [114].

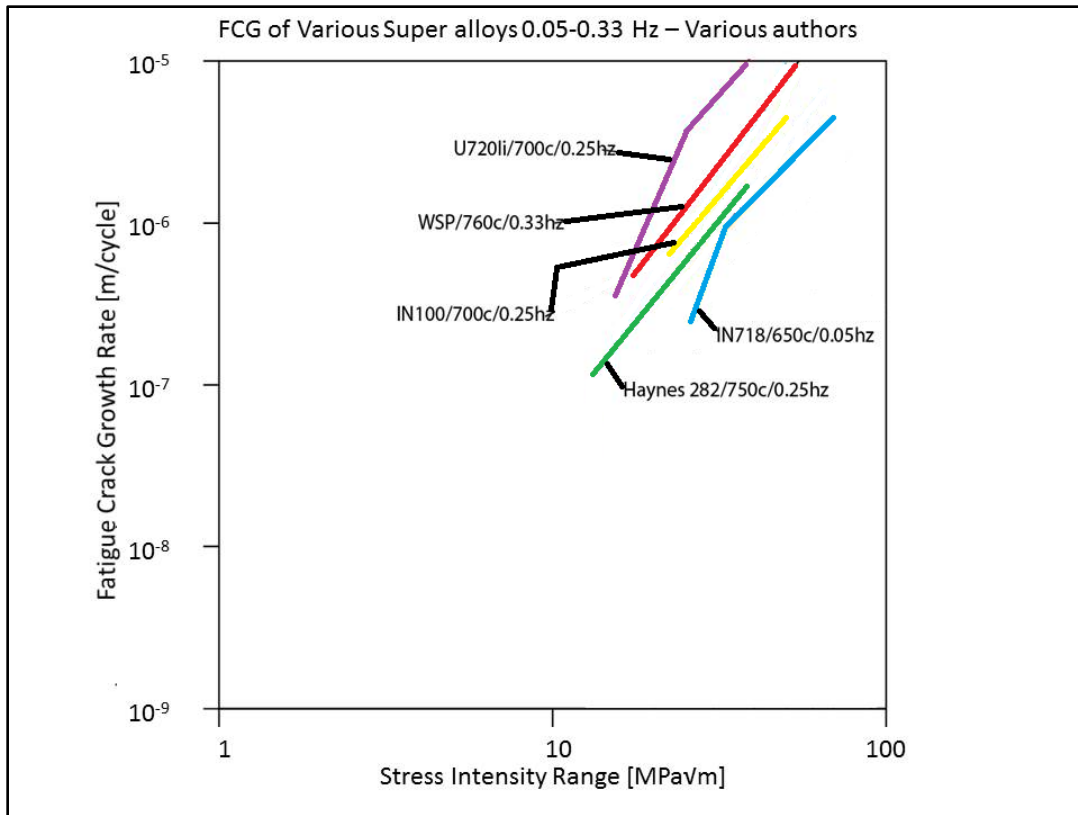


Figure 52 – FCG rates of various superalloys from 650-760°C at 0.05 to 0.33 Hz. IN718 = Inconel 718 [115], U720li = Udimet 720 low interstitial [8], WSP = Waspaloy at 760°C [116], IN100 = Inconel 100 at 700°C [117].

5.2 Fractography results

To help assess the active FCG mechanisms, fracture surfaces were investigated, for various stress intensity ranges using SEM.

5.2.1 Fracture surfaces at 25 Hz loading frequency

Exhibited in Figure 53 are the fracture surfaces for the 25 Hz testing using a sinusoidal loading waveform. Observed from the fracture surfaces Figure 53 is transgranular crack growth, as fracture surface is planar with no grain facets observable. A transition from stair step like stage one crack growth to stage two crack path where fatigue striations are observed around ΔK of $14 \text{ MPa}\sqrt{\text{m}}$ for 550°C and 650°C (Figure 53 B, E), while the

transition occurs at a ΔK of 20 MPa \sqrt{m} for 750°C (not shown). One effect of temperature is to delay the transition from stage one to stage two crack growth at higher temperatures.

Comparing the effect of stress intensity at 550°C (Figure 53 A, B, C) the fracture surfaces appear to get rougher with increasing stress intensity range. A shift from stage one to stage two crack growth is observed as stress intensity range is increased. Secondary cracking is observed between fatigue striations at high stress intensity ranges.

At 650°C (Figure 53 D, E, F) similar observations hold compared to 550°C, where Figure 53 E is rougher than Figure 53 D, stage one to stage two cracking mechanism shift is observable by disappearance of stair step like stage one crack growth and presence of fatigue striations are observable in Figure 53 F.

The fracture surfaces at 750°C (Figure 53 G, H, I) deviate from fracture surfaces at 550°C and 650°C temperatures slightly. Figure 53 G appears to be very smooth with a observable twin and stage one crack growth (stair step like pattern). Also observed in Figure 53 G is possible evidence of grain boundary cavitation, where a void opens between grain boundaries. At 750°C, at high ΔK , secondary cracking appears between fatigue striations, as observed at other temperatures.

The effect of temperature on fracture surfaces with 25 Hz loading frequency appears to smooth the fracture surfaces at low stress intensity ranges. At higher stress intensity ranges the fracture surfaces appear very similar with fatigue striations and secondary cracking between the fatigue striations appearing on most of the surfaces. At low stress intensities ($\Delta K < 10$ MPa \sqrt{m}) some creep mechanisms (shown by grain boundary cavitation, Figure 53 G) seem to be activated at 750°C. As noted prior, increasing the temperature delayed the transition to stage two cracking at 750°C.

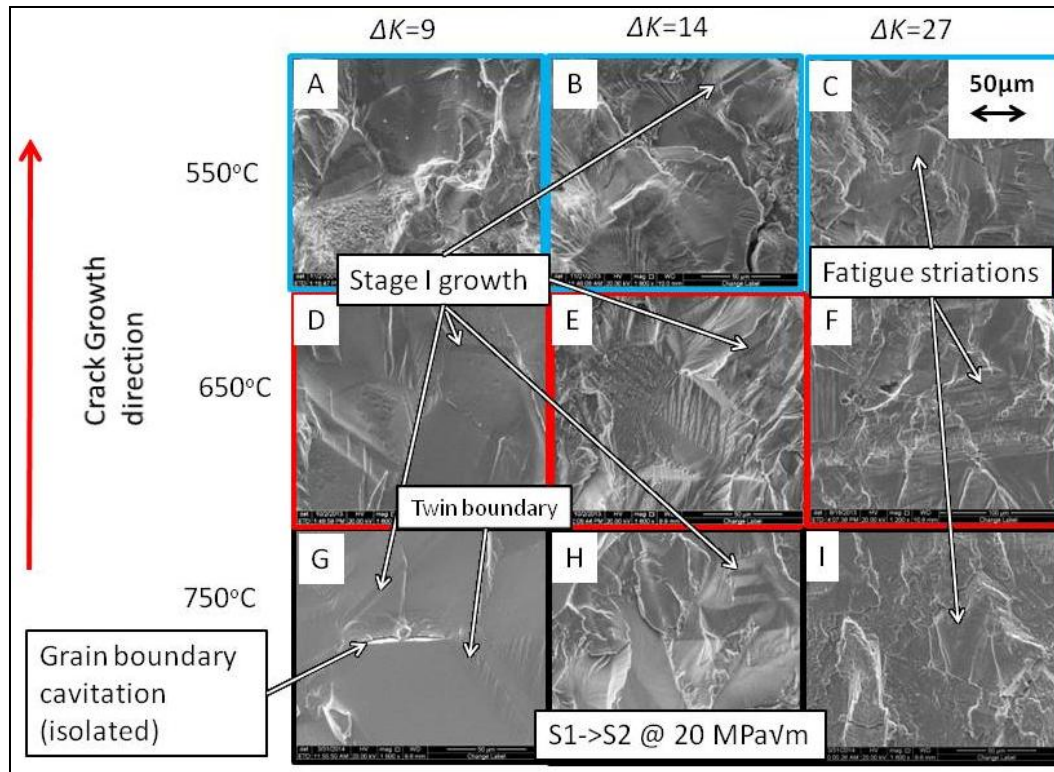


Figure 53 - Fracture surfaces of Haynes 282 tested at 25 Hz, at various temperatures and stress intensity ranges. Crack growth direction is bottom to top for all images A-I. A transition from stage one to stage two crack growth mechanism was observed at ΔK of 14 $\text{MPa}\sqrt{\text{m}}$ for 650°C and below. Not shown is the delayed stage one to stage two cracking mechanism shift at 750°C at ΔK of 20 $\text{MPa}\sqrt{\text{m}}$.

5.2.2 Fracture surfaces at 0.25 Hz loading frequency

Exhibited in Figure 54 is the fracture surface of Haynes 282 at 0.25 Hz testing with a triangular loading waveform. Observed crack growth path is transgranular. Stage one to stage two crack growth transition happened at 14 $\text{MPa}\sqrt{\text{m}}$ for 550°C and 650°C while the transition was not until 19 $\text{MPa}\sqrt{\text{m}}$ at 750°C.

For higher stress intensity range at 550°C (Figure 54 B, C) the fracture surfaces exhibit features of secondary cracking between fatigue striations, and rough transgranular fracture surface. Fracture surfaces at 650°C (Figure 54 D, E, F) are observed to have similar features to that of 550°C.

Observed at 750°C (Figure 54 G, H, I) the fracture surfaces at low ΔK exhibit some possible intergranular features (Figure 54 G), where partial grain facets appear. Stage two crack growth appears to be delayed until higher ΔK of 19 MPa \sqrt{m} .

The effect of temperature on fracture surfaces with 0.25 Hz loading frequency appears to be negligible from 550°C to 650°C. As noted prior, increasing the temperature delayed the transition to stage two cracking at 750°C. Increasing the temperature to 750°C seemed to activate some process which enabled secondary cracking along grain boundaries independent of the applied stress intensity range. The presence of cracking along grain boundaries could mean Coble creep or oxidation influences.

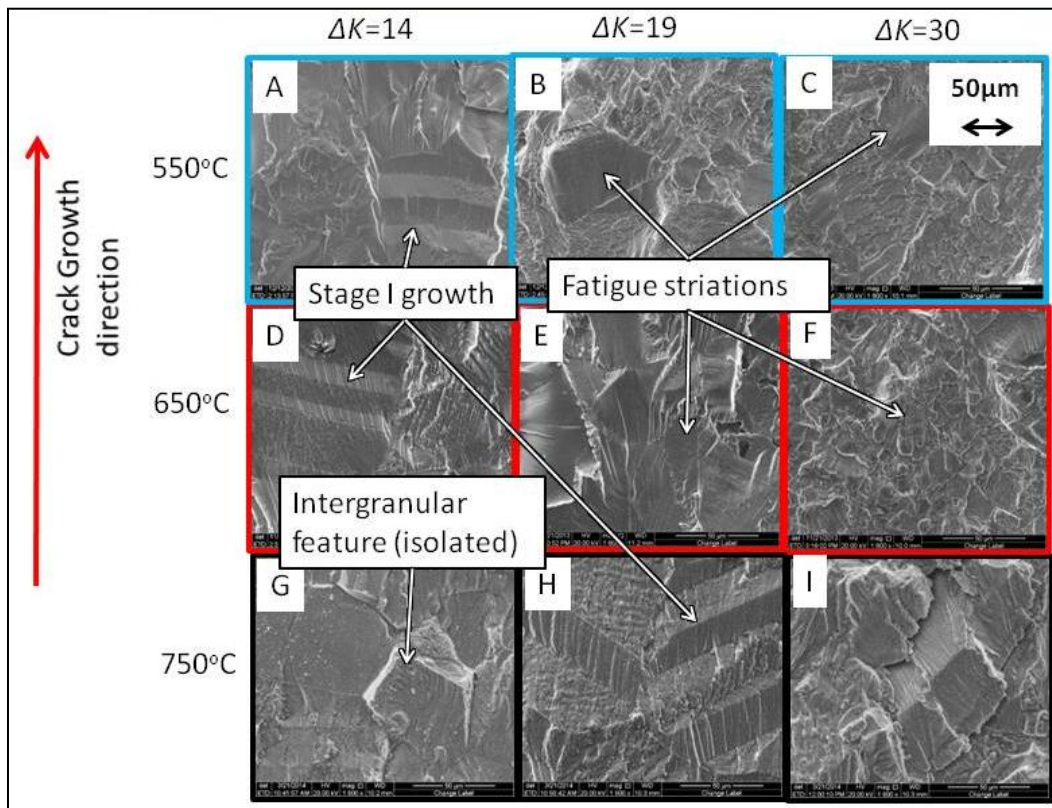


Figure 54 - Fracture surfaces of Haynes 282 tested at 0.25 Hz, at various temperatures and stress intensity ranges. Crack growth direction is bottom to top for all images. A transition from stage one to stage two crack growth mechanism was observed at ΔK of 14 MPa \sqrt{m} for 650°C and below, while this transition happened at ΔK of 19 MPa \sqrt{m} for 750°C.

5.2.3 Secondary cracking

At low stress intensity ranges secondary cracking appeared to be randomly oriented for 650°C and below (Figure 55A, B, D, E). At 750°C when secondary cracking occasionally took place it was observed to follow grain boundaries (Figure 55C & F).

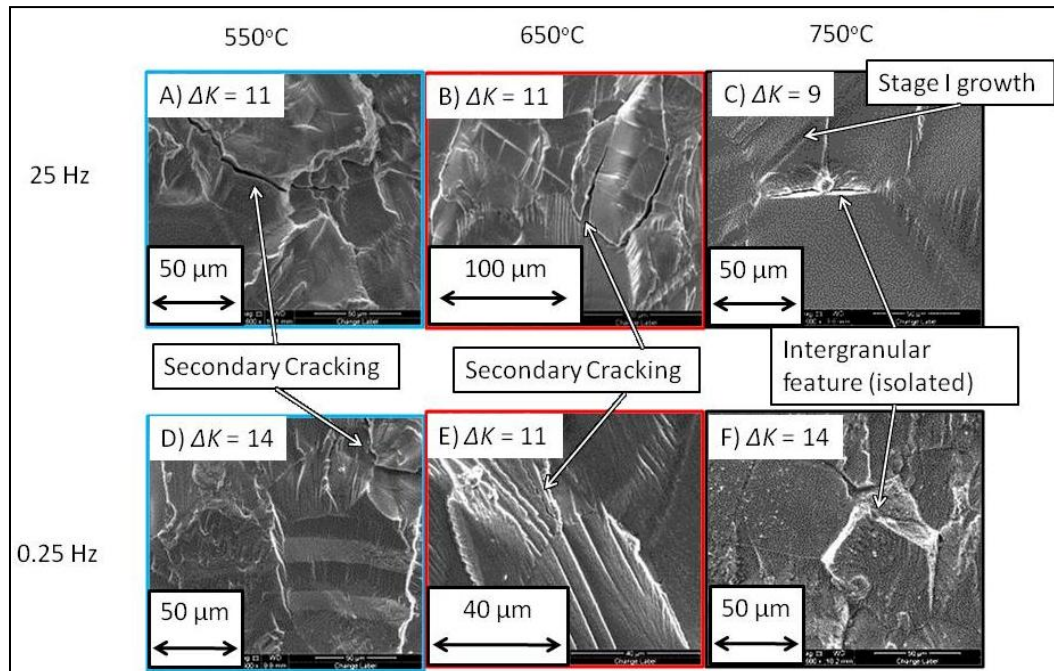


Figure 55 - Secondary cracking at low stress intensity ranges. A-C) secondary cracking at 25 Hz loading frequency, D-F) secondary cracking at 0.25 Hz loading frequency.

At high stress intensity ranges secondary cracking appeared to be biased towards cracking in-between fatigue striations (Figure 56 A-E), except at 750°C at the 0.25 Hz loading frequency. At 750°C at the 0.25 Hz loading frequency the occasional secondary cracking between grain boundaries persisted even at high stress intensity ranges (Figure 56F). The isolated intergranular features observed at 25 Hz loading frequency disappeared as stress intensity range was increased. This indicates frequency may have a minor affect on cracking mode.

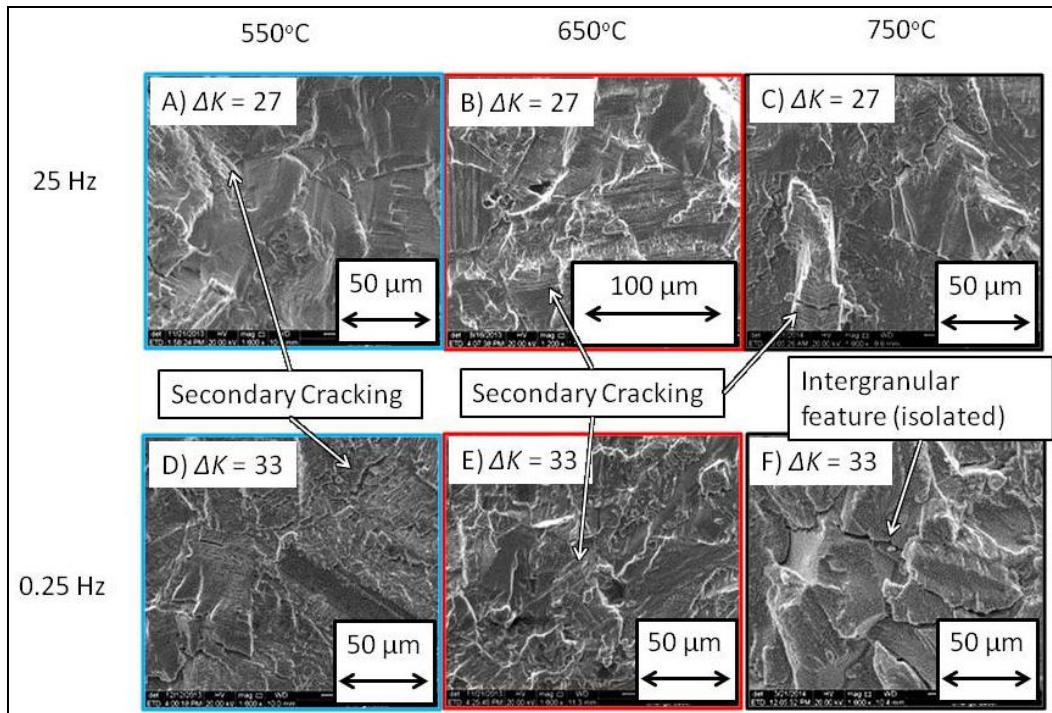


Figure 56 - Secondary cracking at high stress intensity ranges. A-C) secondary cracking at 25 Hz loading frequency, D-F) secondary cracking at 0.25 Hz loading frequency.

5.2.4 Note on intergranular features

The author has shown some features which may mislead the reader to believe the crack path is mixed or intergranular at 750°C. This is false. The author has zoomed into an interesting feature, see Figure 57. No fracture surfaces investigated at 550°C, 650°C and 750°C exhibited mixed or intergranular crack path both at 25 Hz and 0.25 Hz loading wave forms. Neither did the fracture surfaces presented in Appendix II: Fracture surfaces at 0.05 Hz loading frequency, p133 where samples were cracked at 0.05 Hz loading frequency.

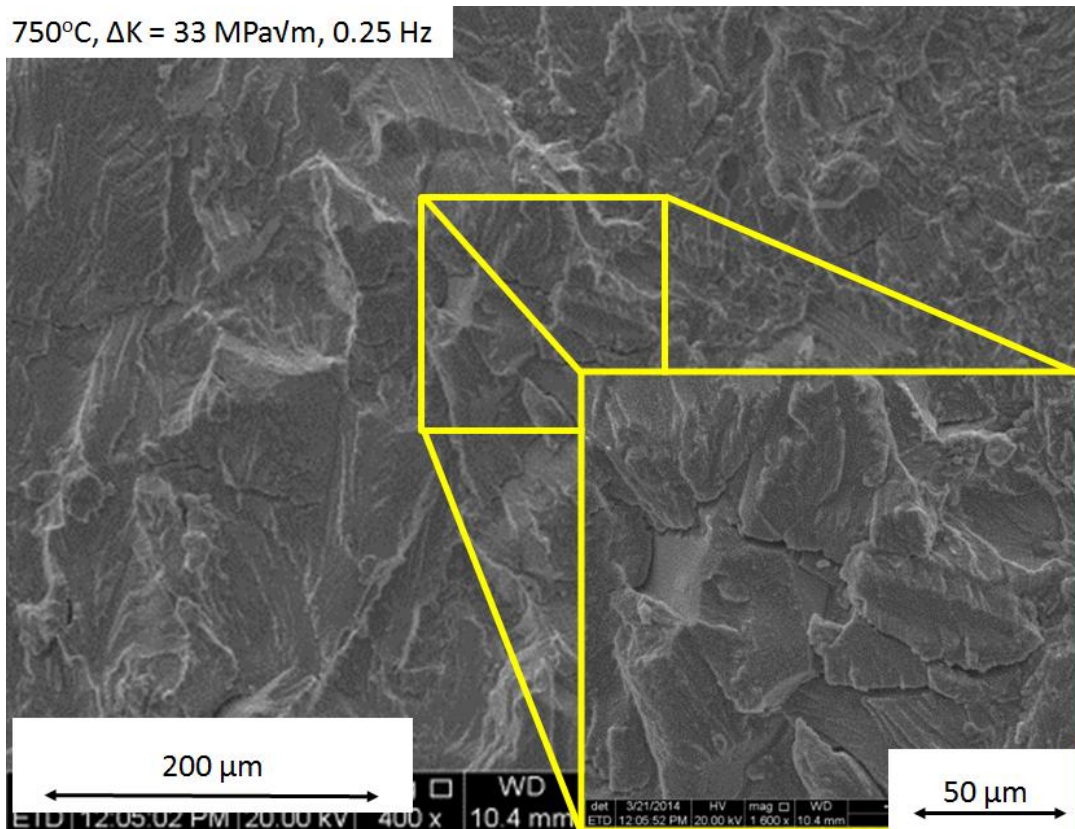


Figure 57 - Lower magnification fracture surface illustrating transgranular crack growth.

5.3 Microstructure results

To help assess the active FCG mechanisms, the plastic zones were investigated at various stress intensity ranges using TEM. The following section presents the results from the microstructure evaluation. Presented first is the peak aged microstructure, followed by the observed active mechanisms, the microstructure correlated with temperature and frequency and dark field images of the gamma prime.

5.3.1 Initial peak aged microstructure

Haynes 282 was tested under peak aged condition. The heat treatment schedule for peak aging is as follows: i) Anneal at 1149°C, ii) Hold at 1010°C for 2 hours then air cool, iii) hold at 788°C for 8 hours then air cool. The peak aging heat treatment shows annealing twins, observed by the straight lines and difference in contrast in Figure 58A, low density

dislocations and occasional carbides (Figure 58B) and carbides precipitated along boundaries (Figure 58C).

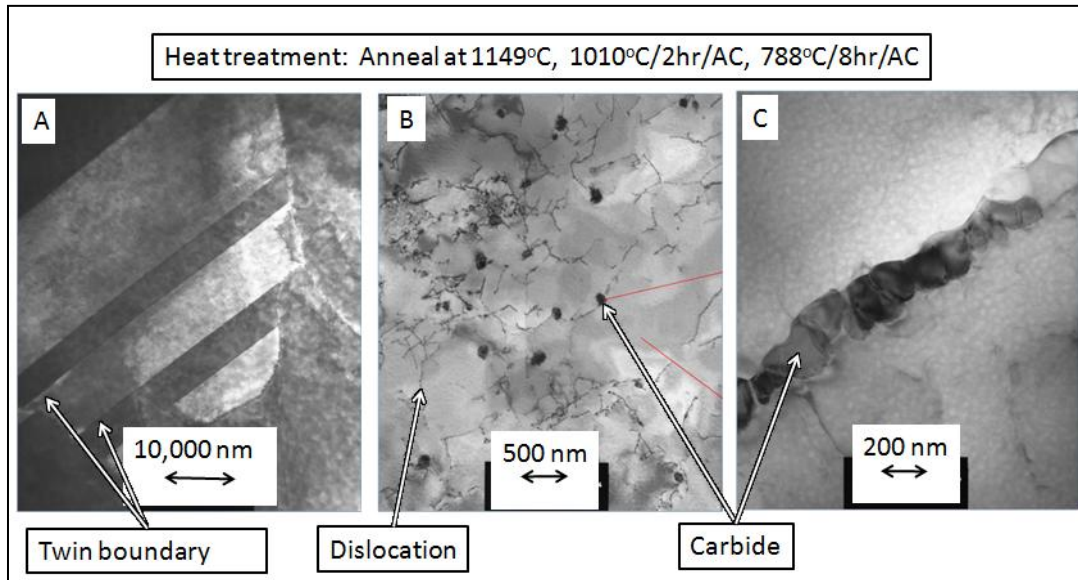


Figure 58 – Initial microstructure after peak aged heat treatment. A) showing annealing twins, B) Showing individual dislocations and carbides, C) showing carbides along a boundary. [118]

5.3.2 Observed active mechanisms

The observed deformation mechanisms in Haynes 282 include the following:

- a) Shearing of gamma prime, observed by the semicircular features observed to be shifted relative to each other in Figure 59A. Also Figure 59D shows shearing of gamma prime by super partial dislocations, where the leading dislocation bows around gamma prime and the trailing dislocation is relatively straight.
- b) Persistent slip bands observable by the classic rung and ladder type morphology (Figure 59B)
- c) Orowan looping where the dislocations bow around the gamma prime precipitates, leaving either loops or horseshoe like dislocations (Figure 59C).

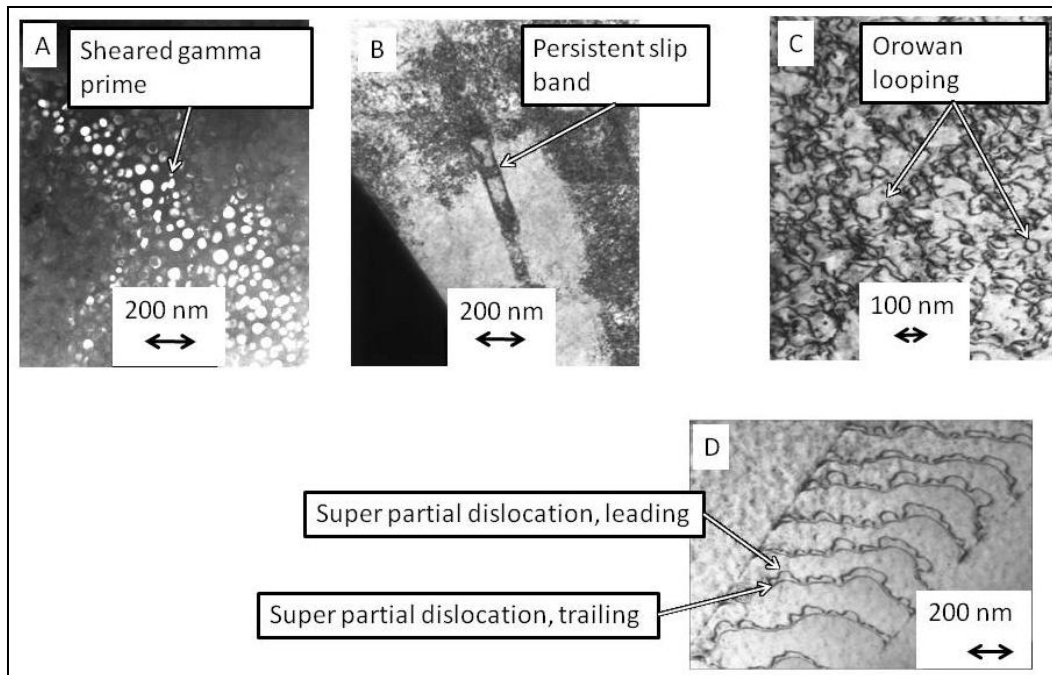


Figure 59 – Observed deformation mechanisms active in Haynes 282. A) shearing of gamma prime, B) Persistent slip bands, C) Orowan looping mechanism, D) shearing of gamma prime by partial dislocations.

5.3.3 Microstructure of the plastic zones

Figure 60, shows the TEM images of plastic zones in front of the crack tips, parallel to the crack (recall Figure 43, p. 66). The specimens were cracked at constant ΔK of 9 ± 1 $\text{MPa}\sqrt{\text{m}}$ at 25 Hz for Figure 60A-C, while for Figure 60D-F, the specimens were cracked at constant ΔK of 14 ± 1 $\text{MPa}\sqrt{\text{m}}$ at 0.25 Hz .

The plastic zone microstructure for 25 Hz loading frequency is shown in Figure 60A-C. Comparing 750°C to 550°C images (Figure 60A & C) it is apparent that the dislocation density is sharply decreased as the temperature increases. At 650°C the sample was thinned too much for high resolution analysis; however, a thick section was digitally enhanced to reveal a high density dislocation structure. At 750°C the deformation mode is dislocation shear bands, with a paired dislocation observed and evidence for Orowan looping is shown (Figure 60C). Because the TEM images are a two dimensional projection of a three dimensional volume it is possible that two separate dislocations are

projected on top of one another, leading to a false interpretation of a paired dislocation. See section 6.5.2 Looping transition, p121 for more details about this paired dislocation.

The plastic zone microstructure for 0.25 Hz loading frequency is shown in Figure 60D-F. Again increasing the temperature from 550°C to 750°C (Figure 60D & F) it is apparent that the dislocation density is sharply decreased. At 550°C dislocation density is high, with what appears to be dislocation vein structure (Figure 60D). At 650°C the dislocation density is "medium", allowing for interpretation of occasional single dislocations. Shown in Figure 60E is a vein structure and a possible Orowan looping at 650°C. At 750°C, (Figure 60F) dislocation density appears the lowest, with the deformation mode being primarily Orowan looping.

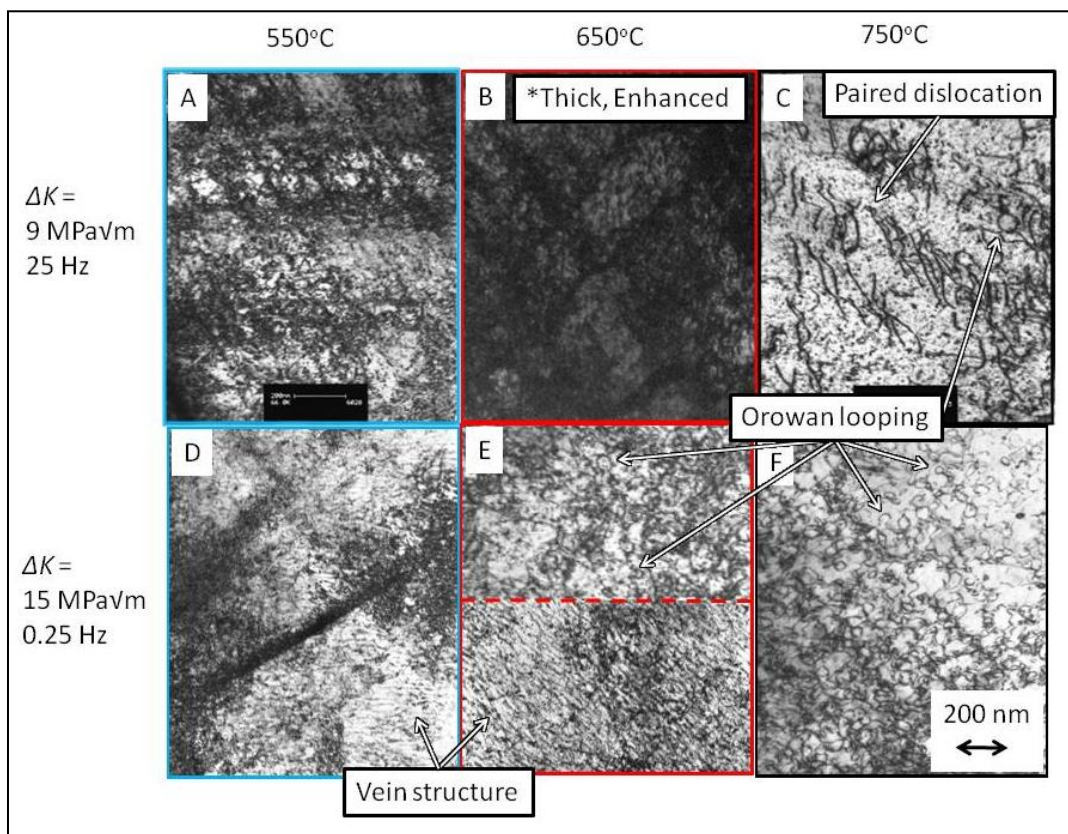


Figure 60 – TEM images of samples selected in front of the crack tip, parallel to the crack. A, B,C Specimen cracked at ΔK of 9 MPa \sqrt{m} at 25 Hz. D, E, F Specimen cracked at ΔK of 15 MPa \sqrt{m} at 0.25 Hz.

5.3.4 Dark field microscopy of gamma prime

To image gamma prime the TEM is set to image in dark field mode. In dark field an aperture is selected to block the electrons traveling straight through from source to sample to detector. Only electrons which are diffracted by the sample into the detector are imaged. This illuminates the diffracted features and leaves a dark background, hence 'dark field'. Because dark field requires a specific crystallographic orientation to diffract electrons into the detector it is more difficult to image in this mode.

Figure 61 shows the dark field microscopy of gamma prime. In only two of the seven samples cut was a reflection orientation found, to diffract gamma prime. Figure 61A shows sheared gamma prime for the sample cracked at 650°C with 0.25 Hz waveform at of ΔK of 15 MPa \sqrt{m} . Figure 61A represents the onset of stage two cracking mechanism. Figure 61B shows gamma prime with no evidence of shearing for the sample cracked at 750°C with 0.25 Hz waveform at of ΔK of 9 MPa \sqrt{m} . Figure 61B represents stage one crack growth.

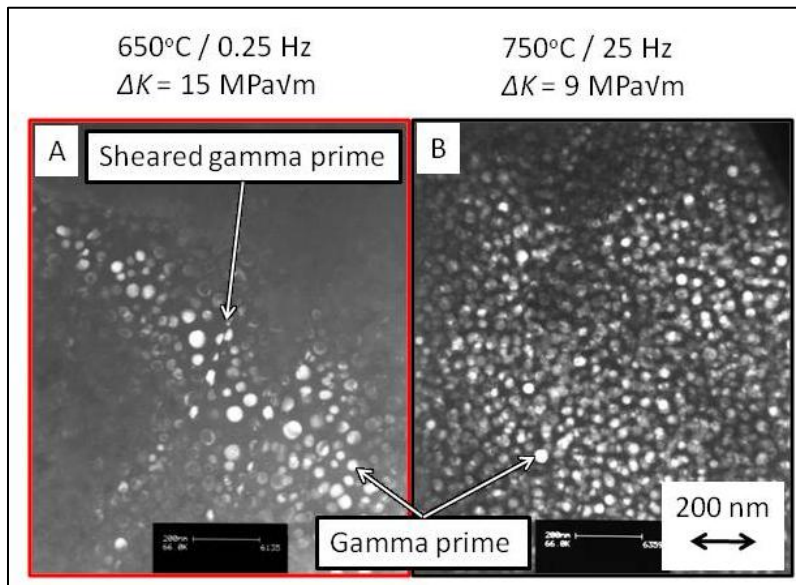


Figure 61 - Dark field microscopy of gamma prime. A) at 650°C with 0.25 Hz waveform at of ΔK of 15 MPa \sqrt{m} B) at 750°C with 0.25 Hz waveform at of ΔK of 9 MPa \sqrt{m} .

5.4 Activation energy

Increases in FCG rates (Figure 46-Figure 47) could be due to changes in mechanical properties such as yield strength and Young's modulus, activated creep mechanisms, or environmental effects such as oxidation. Accordingly, to help determine the thermally activated mechanism the activation energy was calculated as a function of ΔK .

Activation energy was found at ΔK intervals of 1 MPa \sqrt{m} . In general the fits were quite good with R^2 values mostly higher than 0.85. Crack growth rates at each ΔK level were taken from an average of a minimum of 3 data points or ± 0.5 MPa \sqrt{m} in order to reduce uncertainty. Uncertainty in Q varied from 0.1 to 18 kJ/mol depending on the accuracy of the fit in growth rates at each ΔK intervals of 1 MPa \sqrt{m} . At 25 Hz activation energy was plotted from 10-25 MPa \sqrt{m} , while at 0.25 Hz activation energy was plotted from 14-37 MPa \sqrt{m} , see Figure 62.

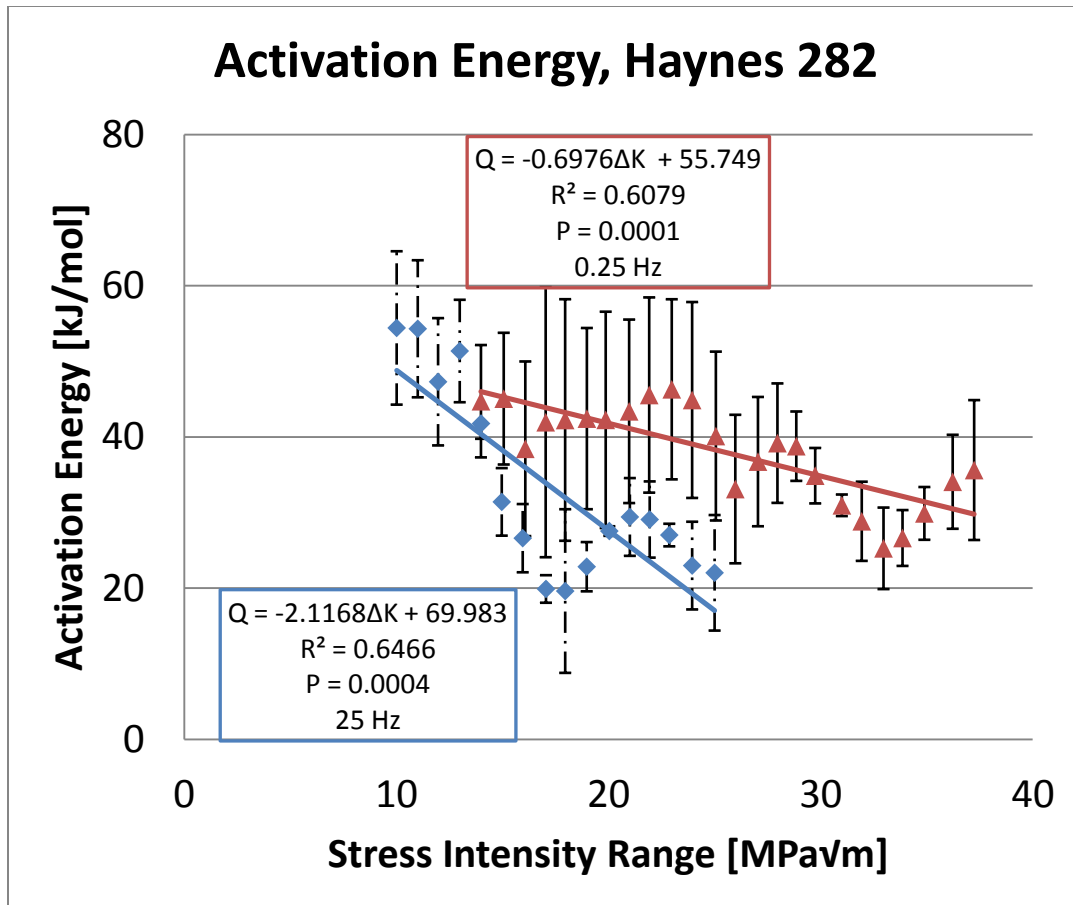


Figure 62 - Activation energy of Haynes 282. Blue diamonds are activation energy in kJ/mol for 25 Hz, while red triangles is for 0.25 Hz. Error bars indicate uncertainty. Statistical analysis of the trendline at 25 Hz shows $P = 0.0004$ and at 0.25 Hz, $P = 0.0001$.

At 25 Hz (blue diamonds from Figure 62), activation energy decreases as stress intensity range increases from 9-17 MPa√m. Statistical analysis shows a statistically significant decrease in the activation energy with increasing stress intensity range with P values less than 0.05. The author believes that for $\Delta K > 17$ MPa√m the FCG rates at a loading frequency of 25 Hz are parallel as shown in Figure 46, p75. Therefore, activation energy would be constant for $\Delta K > 17$ MPa√m; hence, the modeling of 25 kJ/mol at 25 Hz loading frequency.

At 0.25 Hz (red triangles from Figure 62), the activation energy decreases with increasing stress intensity range. Statistical analysis shows a statistically significant decrease in the

activation energy with increasing stress intensity range with P values less than 0.05.

Again it is the authors judgment that the FCG curves at 0.25 Hz loading frequency (Figure 47, p76) are roughly parallel, meaning activation energy would be constant. Therefore at 0.25 Hz, activation energy is modeled at 35 kJ/mol.

5.4.1 Activation energy of other NBSAs

Starink and Reed [91] presented a plot of the activation energy for various NBSAs.

Shown in Figure 63 below is how Haynes 282 performs relative to other alloys. For Udimet and RR1000 large increases in activation energy are observed for 20 second hold times and transition from a vacuum to air environment. Haynes 282 is observed to perform similarly to alloy N18. For Udimet 720, RR1000 and N18 alloys activation energy was calculated from FCG rates at 650°C and 725°C.

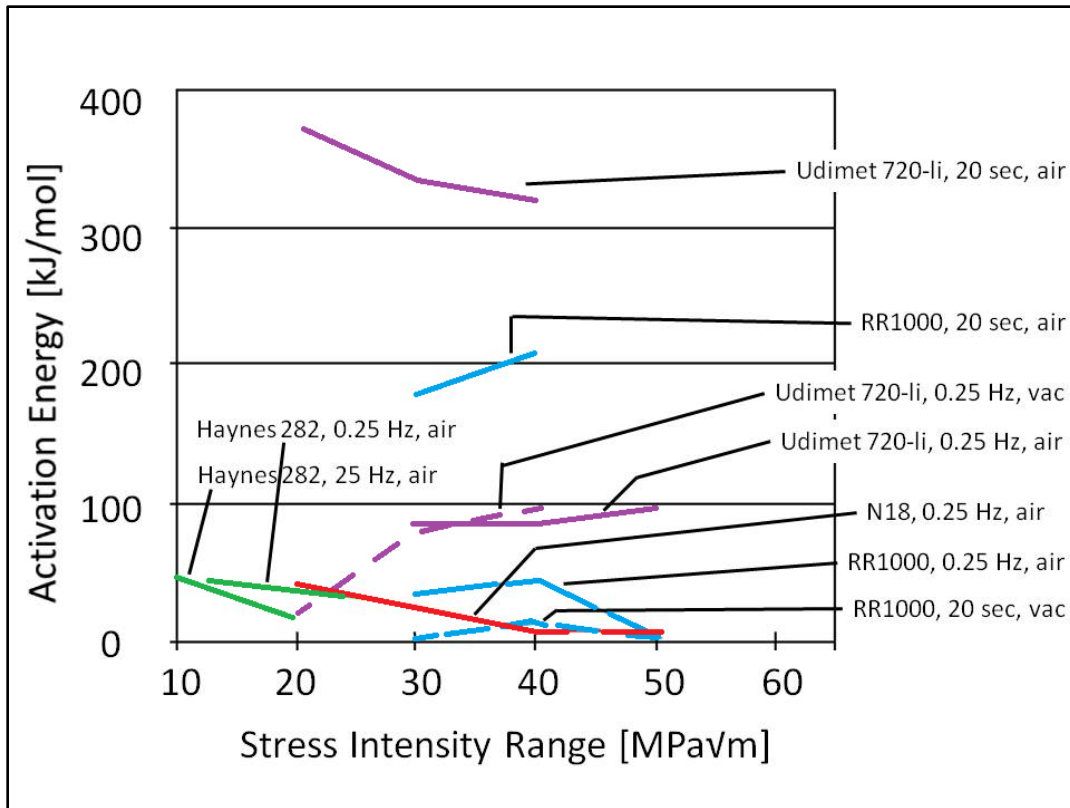


Figure 63 - Activation energy of various NBSA. Vac = vacuum, 0.25 Hz = 0.25 Hz loading frequency with triangular waveform, 20 sec = trapezoidal waveform with 20 second hold time. Sources as follows: Udimet 720li [119] [120], RR1000 [121], N18 [122] [123]

5.4.2 Uncertainty in activation energy

Shown below in Table 10 is the total uncertainty in the activation energy calculation for the FCG curves at 25 Hz loading frequency. Shown below in Table 11 is the total uncertainty in the activation energy calculation for the FCG curves at 0.25 Hz loading frequency.

ΔK [MPa \sqrt{m}]	25 Hz				
	Q [kJ/mol]	Err Q Taylor [kJ/mol]	Err Q fit [kJ/mol]	Err Q Quad [kJ/mol]	% Err Q Quad
10	54	0.6	9.6	10.2	16%
11	54	0.6	8.5	9.1	15%
12	47	0.6	7.9	8.5	16%
13	51	0.6	6.2	6.8	12%
14	42	0.6	1.5	2.1	5%
15	31	0.6	3.9	4.5	13%
16	27	0.6	4.0	4.6	15%
17	20	0.6	1.3	1.9	9%
18	20	0.6	10.3	10.9	36%
19	23	0.6	2.7	3.3	13%
20	28	0.6	0.1	0.7	3%
21	29	0.6	4.6	5.2	15%
22	29	0.6	4.5	5.1	15%
23	27	0.6	1.0	1.5	6%
24	23	0.6	5.3	5.8	21%
25	22	0.6	7.1	7.7	26%
Average	33	0.6	4.9	5.5	15%

Table 10 - Activation energy and uncertainty for 25 Hz.

ΔK [MPa \sqrt{m}]	0.25 Hz				
	Q [kJ/mol]	Err Q Taylor [kJ/mol]	Err Q fit [kJ/mol]	Err Q Quad [kJ/mol]	% Err Q Quad
14	45	0.6	6.9	7.5	15%
15	45	0.6	8.2	8.8	17%
16	38	0.6	11.0	11.6	24%
17	42	0.6	17.3	17.9	30%
18	42	0.6	15.4	16.0	28%
19	42	0.6	11.5	12.0	23%
20	42	0.6	13.8	14.4	26%
21	43	0.6	11.6	12.2	22%
22	46	0.6	12.4	13.0	23%
23	46	0.6	11.4	12.0	21%
24	45	0.6	12.4	13.0	23%
25	40	0.6	10.7	11.2	22%
26	33	0.6	9.3	9.9	23%
27	37	0.6	8.0	8.6	19%
28	39	0.6	7.4	7.9	17%
29	39	0.6	4.1	4.6	11%
30	35	0.6	3.2	3.7	10%
31	31	0.6	0.9	1.5	5%
32	29	0.6	4.7	5.3	16%
33	25	0.6	4.9	5.4	18%
34	27	0.6	3.2	3.7	13%
35	30	0.6	3.0	3.5	11%
36	34	0.6	5.7	6.3	16%
37	36	0.6	8.7	9.3	21%
Average	38	0.6	8.6	9.1	19%

Table 11 - Activation energy and uncertainty for 0.25 Hz.

6. Discussion:

In this section the author will begin by comparing the FCG curves of Haynes 282 to other authors and compare and contrast any found differences in FCG rates. The author will then explain why the FCG rates are observed to increase with temperature. Then the author will explain why the FCG rates are observed to increase with lower loading frequencies. The section will conclude with a discussion on the stage one to stage two crack growth mechanism transition.

6.1 FCG of Haynes 282 from other authors

Buckson and Ojo [100] studied the FCG rates of Haynes 282 at 600°C. Buckson and Ojo used a sinusoidal waveform at 15 Hz and 0.05 Hz at a loading ratio of 0.1. Shown below in Figure 64 and Figure 66 are the how the author's FCG curves compare to Buckson's and Ojo's data.

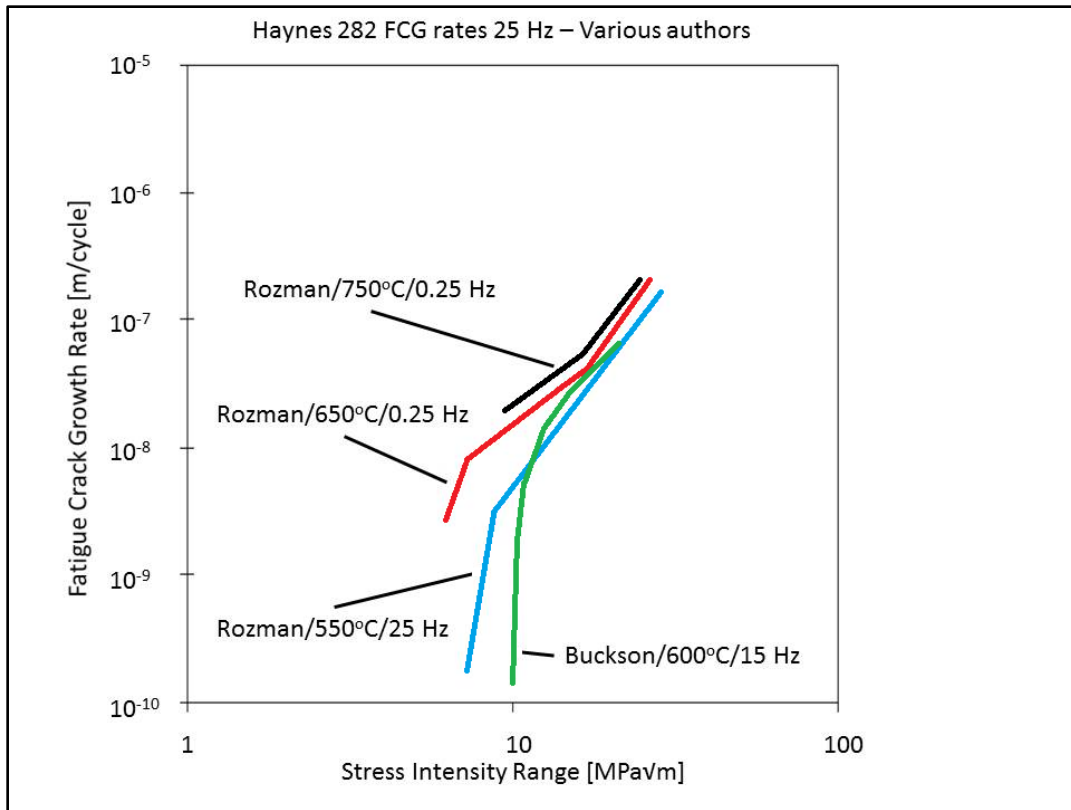


Figure 64 - FCG data of Buckson and Ojo [100] against the author's at high frequency.

Comparing data in Figure 64, Buckson and Ojo tested at 600°C at 15 Hz with a sinusoidal waveform (green line), while the author's tested at 550°C (blue line), 650°C (red line) at 25 Hz also with a sinusoidal waveform. Experimental agreement between the author's occurs between ΔK of ~20 to 14 MPa√m in the Paris regime of FCG. At lower stress intensities experimental data is observed to deviate, with Buckson's and Ojo's data sharply decreasing in crack growth rate.

The author tested ~67% faster frequency than Buckson and Ojo (25 Hz vs 10 Hz). The testing frequencies are close enough together in the two studies one would not expect any influence on FCG due to the testing frequencies.

Buckson and Ojo used a load shedding constant of -0.1 mm^{-1} , while the author used a constant of -0.24 mm^{-1} . The author verified increasing the load shedding constant did not

have adverse effects between ΔK of 14 to 6.5 MPa $\sqrt{\text{m}}$ at both 550°C and 650°C. Therefore, the change in load shedding constant cannot explain the deviance in the data.

Short cracks are known to grow faster than long cracks [5] [109] [110]. However, as noted in section 4.2.1, the author's data was collected using microstructurally long cracks. Buckson and Ojo adhered to ASTM E647 procedure for FCG as well, meaning cracks were microstructurally long as well. Therefore, short cracks cannot account for the difference in threshold value measured in the two studies.

Other possible reasons the data may deviate is due to microstructural grain size differences. Buckson and Ojo had a ASTM grain size of ~2 while the author's material had a ASTM grain size of ~4. Pang and Reed [124] tested Udimet 720Li at various grain sizes ranging from ASTM 9 to 11 and found that fatigue thresholds ranged from ΔK of 6.2 to 8.5 MPa $\sqrt{\text{m}}$ with larger thresholds measured at larger grain sizes. This trend where larger grain sizes lead to higher fatigue crack growth stress intensity thresholds, is also observed in Haynes 282; with Buckson and Ojo's larger grain size having a higher threshold stress intensity than the authors. Grain size may explain the differences in FCG between Buckson and Ojo's data and the author's data.

Other effects which may affect the threshold stress intensity range include oxide formation and tertiary gamma prime size. It is well known that oxide layers may flake off inside the crack tip and shield the crack from the applied stress. This would have the effect of decreasing the stress intensity applied to the crack tip. However, fracture surfaces from Buckson and Ojo show no signs of oxidation. Therefore, oxide induced crack closure is not the explanation for the difference in observed threshold stress intensity ranges between the author's and Buckson and Ojo's data. Chan [125] found increasing the chromium content and tertiary gamma prime size increased FCG thresholds. The author's investigation into the microstructure of Haynes 282 showed no tertiary gamma prime. However, Buckson and Ojo did report fine tertiary gamma prime precipitates (Figure 65). The tertiary gamma prime is likely responsible for the discrepancy in fatigue threshold stress intensity ranges at high frequency loading between the author's and Buckson and Ojo's data.

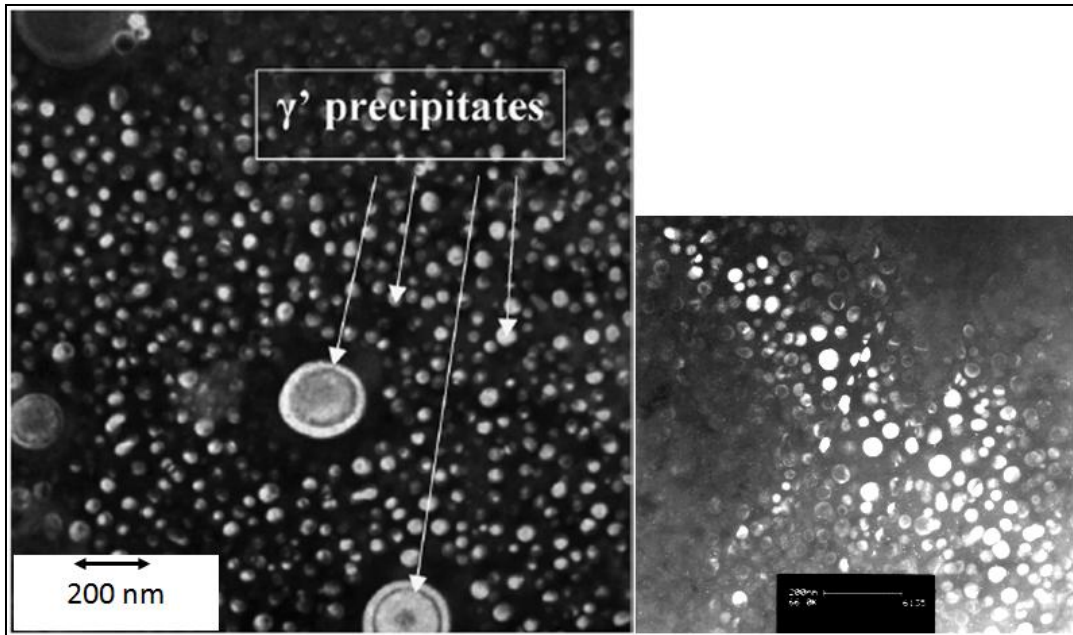


Figure 65 - Microstructure of Haynes 282, images resized to equal scales. A) reported by Buckson and Ojo [100], B) reported by the author.

Comparing data in Figure 66, Buckson and Ojo tested at 600°C at 0.05 Hz with a sinusoidal waveform (green line), while the author's tested at 550°C (blue line), 650°C (red line) at 0.25 Hz with a triangular waveform. At low frequencies the two independently gathered data sets are in good agreement, with the 600°C data gathered from Buckson and Ojo lying in-between the 650°C and 550°C data gathered by the author.

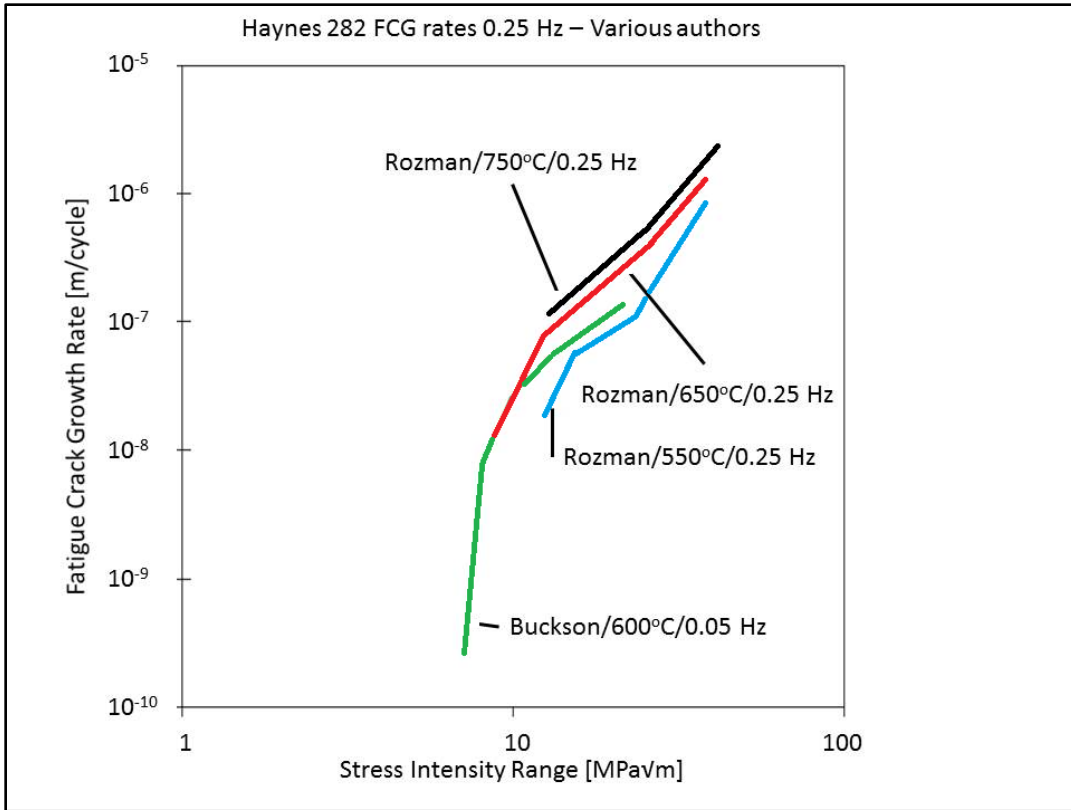


Figure 66 - FCG data of Buckson and Ojo [100] against the author's data at low frequency. The author used a triangular waveform, while Buckson and Ojo used a sinusoidal.

6.2 Verification of activation energy

To verify the difference in FCG rates had an activation energy associated with them, a normalization factor was applied to the calculated activation energy (Equation 23) in a manner analogous to a Zener-Hollomon plot for creep [126]. The Zener-Hollomon method involves multiplying the fatigue crack growth rates by a normalization factor (Equation 23).

$$N = \exp\left(\frac{Q}{R_g T}\right)$$

Equation 23 - Normalization factor applied to the FCG rates.

Chosen activation energies of 25 kJ/mol and 35 kJ/mol selected for 25 Hz and 0.25 Hz loading frequencies respectively. The observance of coincidence of the normalized FCG rates shows that an affect of 25 kJ/mol is acting on FCG at 25 Hz and 35 kJ/mol is acting on FCG at 0.25 Hz; see Figure 67.

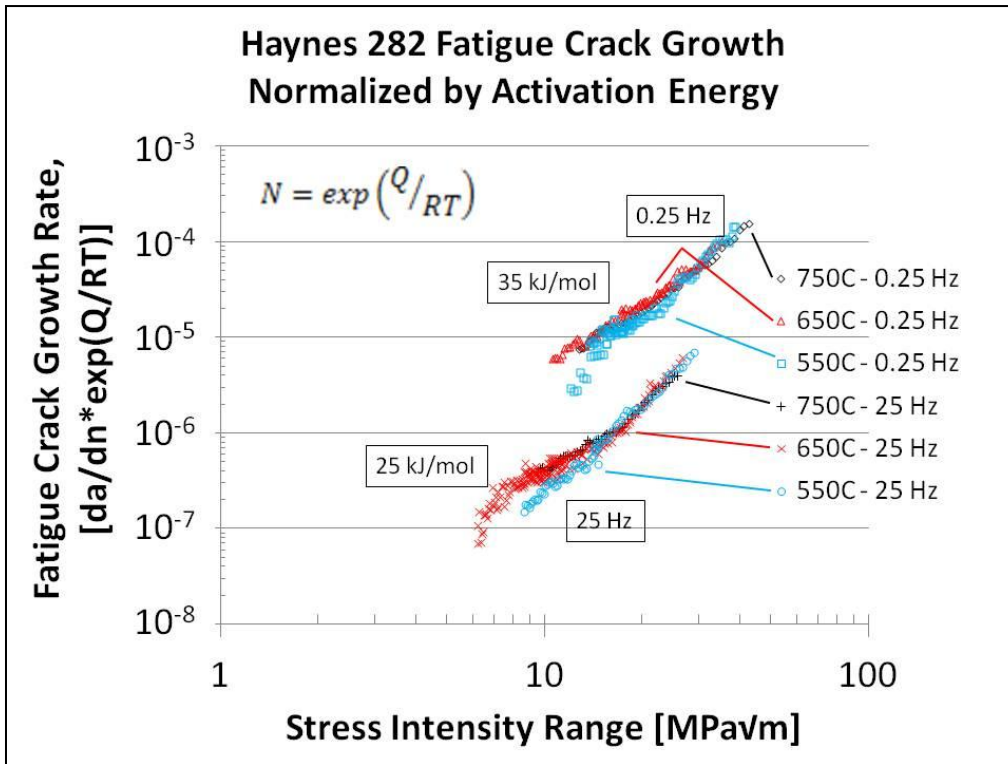


Figure 67 - Normalized FCG rates by activation energy of 25 kJ/mol for 25 Hz (lower group) and 35 kJ/mol for 0.25 Hz (upper group).

At 25 Hz loading frequency coincidence of the FCG curves in Figure 67 is better for $\Delta K > 14.5 \text{ MPa}\sqrt{\text{m}}$. For $\Delta K < 14.5 \text{ MPa}\sqrt{\text{m}}$ coincidence for 550°C is observed to deviate. This could be due to a crack growth mechanism change. However, stage one to stage two crack growth mechanism change occurred at ΔK of 14 $\text{MPa}\sqrt{\text{m}}$ at 650°C and ΔK of 20 $\text{MPa}\sqrt{\text{m}}$ at 750°C. With coincidence of the 650°C and 750°C curves despite the different stress intensities observed for crack growth mechanism change, the deviance of the 550°C crack growth curve at $\Delta K < 14.5 \text{ MPa}\sqrt{\text{m}}$ is unlikely to be explained by a change in crack growth mechanism from stage one to stage two.

At 0.25 Hz loading frequency coincidence of the FCG curves was good for $\Delta K > 25$ MPa \sqrt{m} and for $14 \text{ MPa}\sqrt{m} < \Delta K < 15 \text{ MPa}\sqrt{m}$. The observed deviation from coincidence between $15 \text{ MPa}\sqrt{m} < \Delta K < 25 \text{ MPa}\sqrt{m}$ is likely due to experimental variation.

6.3 Discussion of temperature effect on FCG curves

Increases in FCG rates (Figure 46, p75 and Figure 47, p76) with increasing temperature may be due to temperature dependent changes in mechanical properties such as yield strength and Young's modulus, thermally activated creep, environmental effects such as oxidation, or other thermally activated mechanisms. The following subsections will discuss the effect of the mentioned attributes.

6.3.1 Effect of mechanical properties on FCG curves

To account for the temperature dependence of the elastic modulus and yield strength, FCG data is replotted with a normalized stress intensity range in Figure 68. The normalization (Equation 24) is based off of the concept that the increase in FCG rates should be related to the increase in crack tip opening displacements at higher temperatures [127].

$$\Delta K_{norm} = \Delta K / \sqrt{\sigma_y E}$$

Equation 24 – Mechanical normalization factor. Where: ' ΔK ' is the stress intensity range, ' σ_y ' is the yield stress, 'E' is Young's modulus

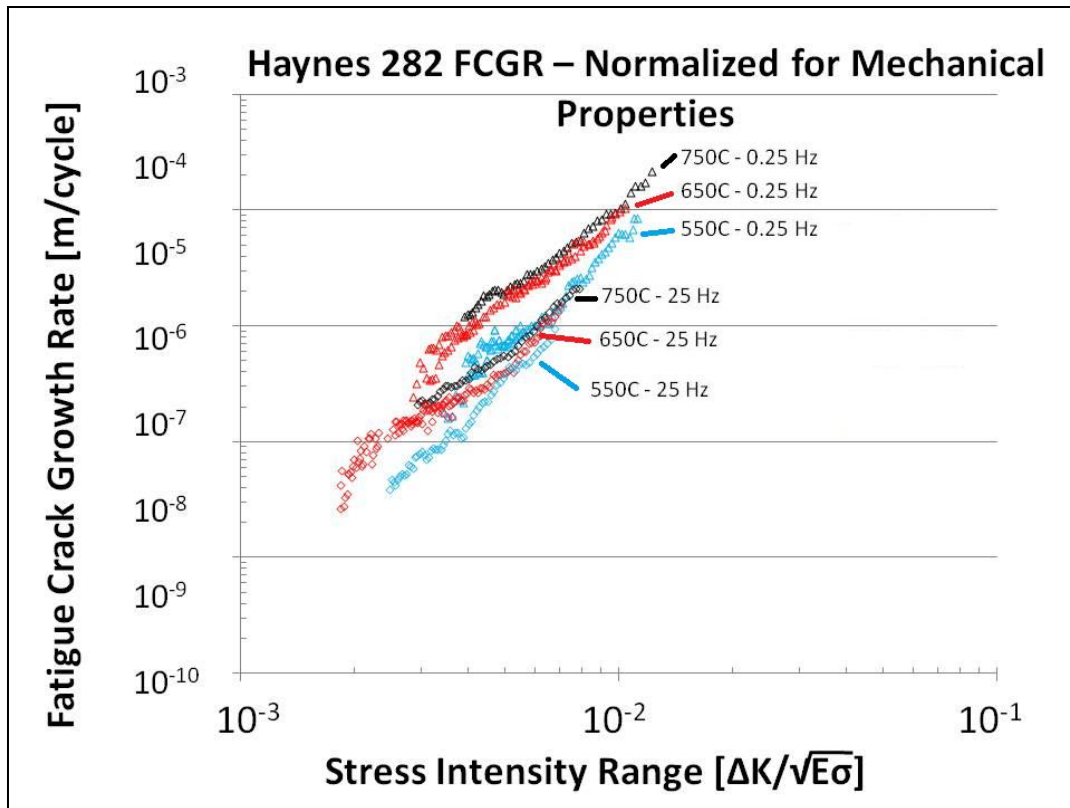


Figure 68 - FCG of Haynes 282 normalized by yield strength and Young's modulus changes with temperature.

It is apparent from Figure 68 that a temperature dependent shift in FCG persists after normalization of the stress intensity range using Equation 24, suggesting changes in yield stress and Young's modulus are not solely responsible for the increase in FCG observed with temperature.

Temperature dependent mechanical properties such as Young's modulus and yield strength may account for up to 60 KJ/mol of activation energy [91]. Pike [4] has gathered tensile data at various temperatures, which is reported in Table 7, p57. Following an Arrhenius type regression of the data reported in Table 7 the activation energy found due to mechanical properties varying with temperature is estimated near 3 kJ/mol between 550°C to 750°C, which is much lower than 25 and 35 kJ/mol processes determined to be active. It is concluded that changes in mechanical properties due to

increased temperature is not the reason the FCG rates are observed to increase with temperature.

6.3.2 The effect of environment effects on FCG

Environmental effects are known to affect FCG. Environmental effects such as oxidation have a temperature threshold, below which no adverse effects are observed. Typically environmental effects such as oxidation will tend to transition the crack path from a transgranular crack path to an intergranular crack path [7] [6], drastically increasing the FCG rates. For a crack to transition from transgranular to intergranular crack path, the grain boundaries need to be weakened. Oxygen has been observed to lower grain boundary strength for other NBSAs [6] [85]. While oxygen damage is possible, fractography (Figure 53, p84 and Figure 54, p85) shows no signs of oxidation.

Oxidation for nickel based super alloys appears to be chemistry dependent, with high Nb alloys having high activation energies near 250 KJ/mol, while Nb free and high Cr alloys, similar to Haynes 282 have activation energies much lower between 80-40 KJ/mol [128] [129] [130]. The oxidation of pure Ni has an activation energy of 130 KJ/mol between 600-800°C [128].

Using data from Pike [4], one may estimate the oxidation activation energy for Haynes 282 alloy. Table 12 exhibits data found by Pike [4]. Pike reportedly placed sections of Haynes 282 alloy in 817°C, 927°C and 982°C flowing air for six 168 hour cycles and reported metal loss or 'spalling' and average effected depth of oxidation. From an Arrhenius type regression of the data reported in Table 12 (using depth of oxidation) the activation energy due to oxidation is estimated near 120 KJ/mol, near that of pure Ni.

Temperature [°C]	metal loss [μm]	Depth of oxidation [μm]
871	5	15
927	3	28
982	5	46

Table 12 - Oxidation depth in Haynes 282 as reported from Pike [4].

With measured activation energy peaking at 50 kJ/mol, and no evidence of oxidation from the fractography, oxidation is not considered to cause the increase in FCG rates observed with temperature.

Further investigations in local chemistry may be useful. It may be the case that local oxygen is slightly higher than the surrounding grains, weakening the grain boundaries slightly. Similarly, boron and phosphorus assist grain boundary cohesiveness, and depletion of these alloying elements may also assist grain boundary cracking. For Haynes 282, boron is an alloying element while phosphorus is not. Detection of local species of elements was not done under this project.

6.3.3 The effect of microstructural phases at high temperature

As noted by Hawk et al. [104], small amounts of sigma phase were calculated to be present via ThermoCalc. No evidence was found for sigma phase. No tertiary gamma prime was found, observable growth in grain size, or carbides. As microstructural changes were not observed, microstructural changes due to temperature cannot explain the increase in FCG rates.

6.3.4 Temperature dependent shear

As dislocations annihilate the matrix dislocation density is reduced. With a reduction in dislocation density, each dislocation is carrying more strain, and the matrix is softer. With less obstacles (sessile dislocations) the glissile dislocations may glide with less resistance to the crack tip, enhancing the FCG rates.

High temperature deformation was studied in Waspaloy [131] and Nimonic 80A [132]. At 800°C for Nimonic 80A, dislocation densities drop significantly with temperature. With reduced dislocation density the dislocations encountered less resistance to glide and carried higher strain per individual dislocations. Shearing in gamma prime was observed in Nimonic 80A [132], Waspaloy [133] [134] and Rene 80 [135] leading to further softening at high temperatures.

Temperature dependent shear mechanisms have been observed by Xie et al. [136]. Using atomistic simulations Xie et al. found at low temperatures gamma prime would undergo shear; however, at high temperatures thermally activated cross slip assisted in formation of Lomer-Cottrell locks.

Xie et al. proposed a mechanism in NBSAs involving superpartial dislocations moving through gamma prime forming Lomer-Cottrell locks. Xie et al. found the activation energy of forming Lomer-Cottrell locks of 48 KJ/mol at 5% strain. The energy barrier to form the Lomer-Cottrell lock was strain dependent and decreased with increasing strain. Shear of superpartials through gamma prime was found to be 24.5 KJ/mol and unlocking of Lomer-Cottrell locks was 155 kJ/mol. Lomer-Cottrell locks were found not to form below 3% strain.

Based on the findings of Xie [136] gamma prime should undergo shearing as the measured activation energy is 25 kJ/mol or above. Figure 61A, p92 shows the shearing of gamma prime at 650°C at 0.25 Hz loading frequency. From Figure 61B, p92 gamma prime appeared undeformed at 750°C; however, the presence of paired dislocations(Figure 60C, p91), would suggest shearing of precipitates. Finding a reflection orientation for gamma prime was difficult. Therefore, conclusions on the shear of gamma prime is avoided with only two areas showing gamma prime.

Assuming 5% or greater strain in the plastic zone ahead of the crack tip, an activation energy of 50 kJ/mol would suggest a Lomer-Cottrell locking mechanism might be active in the gamma prime, effectively locking slip in the gamma prime at higher temperatures. Locking of slip mechanism would force dislocations to bow around or cross slip or climb around precipitates to continue deforming. However, the author would expect the formation of Lomer-Cottrell locks in gamma prime to act as a strain hardening mechanism, which would decrease the crack growth rate, rather than enhance it. The experimental observations were such that increasing the temperature increased the FCG rates; therefore, formation of Lomer-Cottrell locks is not the likely explanation for observed increases in FCG rates with increasing temperature.

6.3.5 Temperature dependent dislocation cross slip and annihilation

Evidence of cross slip is inferred from the micrographs (Figure 60, p91) via dislocation annihilation. Looking at the microstructure (Figure 60, p91) it is apparent that the dislocation density is reduced as temperature increases at both loading frequencies. Because the TEM samples were cracked at the same stress intensity levels, the amount of dislocations generated will be the same between all temperatures. Therefore, the observed drop in dislocation density as temperature is increased is due to dislocation annihilation via cross slip and/or climb.

Dislocations may annihilate by exiting the surface or gliding into a dislocation of opposite sign. Dislocation annihilation by exiting surfaces cannot explain the reduction in dislocation density because the grains are held together by plastic constraint, limiting the amount of physical deformation. Therefore, dislocations are annihilating by gliding into the opposite sign dislocation. For screw dislocations this involves cross slip, and for edge dislocations this involves climb.

The activation energy required to collapse a partial dislocation via the Escaig model in nickel is ~ 227 kJ/mol [33], which is too high to account for thermally activated cross slip. When extended screw dislocations intersect with forest dislocations, Rao et al. [35] found that the activation energy for cross slip could be lowered by 2-5 times relative to the Escaig model.

Brown found for pure Ni, the activation energy for jog migration in screw dislocations was 12.5 kJ/mol [41]. The migration of jogs will reduce the spacing between screw dislocation dipoles, as schematically shown in Figure 18, p21.

Spontaneous annihilation distance for a screw dislocation pair is known to be thermally activated and increase with temperature for cross slip [137] [138]. Paus et al. [40] reported the critical minimum distance for cross slip annihilation in a screw dislocation pair was expanded from 51 nm at 20°C to 116 nm at 477°C in pure nickel [139].

For edge dislocations to annihilate they must climb. Climb is a thermally activated process, rate limited by vacancy diffusion. The activation energy for climb is the same as self diffusion, which for nickel is 285 kJ/mol [140] [141]. However, measured activation energy peaked around 50 kJ/mol for the authors experiments. This means there is not enough energy in the system to support continuous dislocation climb, which leads to creep processes. Because the annihilation distance for cross slip is known to increase with temperature, the author assumes that the spontaneous annihilation distance between two edge dislocations in a dipole would also increase, even though the mechanism for edge dislocation annihilation is climb and not cross slip.

Evidence for climb could entail a dislocation curved around a precipitate, or a paired dislocation which disappeared in some section, leaving a 'v' shaped ligament between the glide planes. No such evidence was found from TEM images for dislocation climb. Likely, the dislocations annihilated without any traces left in the TEM samples.

With an activation energy of 12.5 kJ/mol for jog migrations and measured activation energies greater or equal to 25 kJ/mol, jog migrations likely play a role in dislocation annihilation. Also thermally activated widening of the critical distance between a screw dislocation pair to spontaneous cross slip and annihilate, is another likely mechanism to explain the reduction in dislocation density.

6.3.6 Summary of temperature effects on FCG

Discussed in this subsection were the noted effects of temperature on FCG rates. Thermal degradation of mechanical properties was not found to explain the increases in FCG rates as activation energy was too low and normalization did not collapse the FCG curves. Investigations into oxidation also showed inadequate activation energy and lacked the typical intergranular fracture features. Temperature dependent shear of gamma prime was not found to be congruent with experimental observations. Lastly no evidence for detrimental microstructural phases was found.

The only mechanism found to be causal in the increase in FCG rates was the creep related mechanism of thermally activated cross slip and dislocation annihilation. The noted

activation energy in pure Ni, for jog migration (which assists dislocation annihilation) was 12.5 kJ/mol which fits with the measured activation energy. The microstructure showed greatly reduced dislocation density at high temperatures, reinforcing dislocation annihilation. Also thermally activated widening the critical distance between a screw dislocation pair spontaneous cross slip annihilation is another likely mechanism to explain the reduction in dislocation density.

6.4 Discussion of Frequency effects on FCG rates

The effect of frequency on the FCG rates was observed to be minimal at 550°C (Figure 48, p77), but large at 650°C and above (Figure 49, p78 and Figure 50, p79). At 550°C the FCG rates appear to merge around ΔK of 20 MPa \sqrt{m} . At 650°C and above the FCG rates are observed to increase by ~0.5 orders of magnitude by decreasing the loading frequency from 25 to 0.25 Hz.

The effect of frequency on the crack growth mechanism appeared minimal for 650°C and below. For both the loading frequencies of 25 and 0.25 Hz stage one to stage two cracking mechanism shift happened at ΔK of 14 MPa \sqrt{m} for temperatures of 650°C and below, while this shift was delayed at 750°C until a ΔK of ~20 MPa \sqrt{m} . The largest difference in crack growth due to frequency was the continued onset of creep like features influencing the secondary cracking at 750°C at the lower loading frequency of 0.25 Hz.

The effect of frequency on microstructure should be taken with a caveat, as the stress intensity ranges are different from the TEM samples. Comparing Figure 60A-C, p91 to Figure 60D-F, p91 is not a one to one comparison and the effect of increasing stress intensity should also be considered. For both loading frequencies of 25 and 0.25 Hz increasing the temperature decreased the dislocation density. The effect of frequency seemed to shift dislocation motion from shearing to looping at 750°C; however, this effect could be explained also by increasing the stress intensity, as there is a minimum stress required to bow a dislocation around a precipitate.

6.4.1 The effect of creep on FCG rates

Evidence supporting creep related cracking included grain boundary cavitation as shown in Figure 53G, p84. Grain boundary cavitation is a process where vacancies diffuse and aggregate around a grain boundary, leaving a void [75]. Also supporting creep processes during FCG at low stress intensity ranges is Figure 54G, p85 where it appears a grain has partially exited from the surface. Cracking along grain boundaries was observed at higher stress intensity ranges in Figure 56F, p87.

However, supporting evidence for LEFM controlled stage one cracking appear on Figure 53G, p84, where stage one crack growth (stair case pattern) was observed. The concurrent creep and LEFM crack growth mechanisms suggest both mechanisms are active and competing to influence the crack growth path. This would mean that the creep damage zone does not exceed the LEFM damage zone (Figure 23, p30). The LEFM plastic zone size at ΔK of $10 \text{ MPa}\sqrt{\text{m}}$ is $\sim 76 \text{ }\mu\text{m}$.

There appears to be a temperature threshold for the intergranular like features observed in the fractography as they only appear at 750°C . There also seems to be a time dependent threshold as intergranular like features at 750°C appear throughout the 4 second waveform, but only show up at low crack velocities / low stress intensity ranges in the 0.04 second waveform.

For 25 Hz loading frequency (0.04 second waveform) it would appear that creep has a minor influence and the loading frequency is too fast for any type of creep mechanisms to dominate. The LEFM plastic zone is also observed to dominate over the creep damage zone, with creep related phenomena limited to $\Delta K < 10 \text{ MPa}\sqrt{\text{m}}$.

To explain observed creep related features on secondary cracks at 25 Hz loading waveform for $\Delta K > 10 \text{ MPa}\sqrt{\text{m}}$, one should consider the LEFM plastic zone size (Equation 9, p25) in relation to the creep damage zone. Creep related phenomena are just beginning to activate for $\Delta K < 10 \text{ MPa}\sqrt{\text{m}}$ where the LEFM plastic zone is small ($\sim 76 \text{ }\mu\text{m}$). Since creep is time dependent, the creep damage zone is assumed constant, as the loading frequency was constant. This is not exactly true as the creep damage zone is

actually visco-plastic, see Figure 69. However, for purposes in this argument, the creep damage zone is assumed to be dependent on the loading waveform time. For $\Delta K > 10$ $\text{MPa}\sqrt{\text{m}}$ the LEFM plastic zone size significantly exceeds the influence of creep.

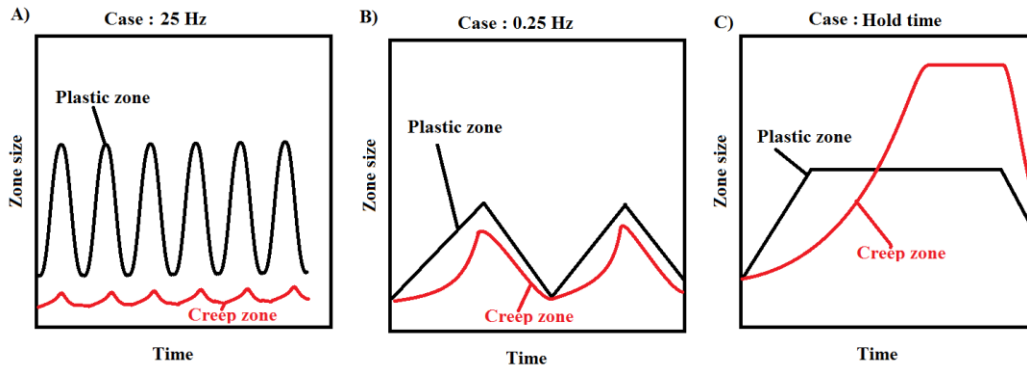


Figure 69 - Schematic of visco-plastic creep damage zone. A) small creep zone at high frequency, B) larger creep zone at lower frequency, C) creep zone exceeds plastic zone with a time delay.

For the 0.25 Hz loading frequency, creep related phenomena were observed throughout all measured stress intensity ranges. Because creep related phenomena are observed throughout all stress intensity ranges measured at 750°C with 0.25 Hz loading frequency, the damage zone for creep is having some effect on the FCG rates at 0.25 Hz loading frequency. However, because the creep related features were isolated the LEFM plastic zone is observed to be the dominant crack growth mechanism even at small stress intensity ranges, where the plastic zone is reduced in size. The LEFM plastic zone size at ΔK of $10 \text{ MPa}\sqrt{\text{m}}$ is $\sim 76 \mu\text{m}$ and it is $\sim 1200 \mu\text{m}$ at ΔK of $40 \text{ MPa}\sqrt{\text{m}}$. The creep damage zone is dependent on the loading frequency and applied load (Figure 69). If the creep damage zone was $600 \mu\text{m}$ (50% of plastic zone at high stress intensity range) than significant creep influence would happen at low stress intensity ranges, which is not observed. Likewise, if the creep damage zone was $38 \mu\text{m}$ (50% of plastic zone at low stress intensity range) then creep influence would disappear at high stress intensity ranges, which also was not experimentally observed.

Shown in Appendix II: Fracture surfaces at 0.05 Hz, p133, are the fracture surfaces with loading waveform of 0.05 Hz (20 seconds per cycle). For 650°C the fracture surfaces appear primarily transgranular with no evidence of transgranular crack growth. At 750°C the fracture surfaces were still primarily transgranular; however, sometimes grain facets are clearly visible on fracture surfaces. It would appear that further increasing the creep damage zone (going from 4 s to 20 s waveform) did not transition the crack path to an intergranular mode.

To transition the cracking mode to an intergranular type, the author would suggest going to a higher temperature or hold time. Boehlert and Loganbach [105] have shown intergranular fracture creep in Haynes 282 at 815°C and Starink and Reed [91] have shown large increases in activation energy in U720 and R1000 by introduction of a 20 second hold time.

6.4.2 Steady state diffusion creep

Nabarro-Herring creep occurs around 210 to 300 KJ/mol [140] [142] [143] [144] which is the activation energy of self diffusion and various common alloying elements in NBSAs. With high activation energy (210+ kJ/mol vs measured 50 kJ/mol) Nabarro-Herring creep is ruled out as the cause for the increase in FCG rates.

Starink and Reed [91] have reported that Coble or grain boundary creep for nickel base super alloys, occurs around 150 KJ/mol which corresponds to the diffusion of various metallic elements along grain boundaries. With peak activation energy measured at 50 kJ/mol, there is not enough energy to sustain Coble creep in Haynes 282, even though intergranular type features were observed at 750°C (Figure 53G, p84, Figure 54G, p85 and Figure 56F, p87)

6.4.3 Strain rate sensitivity in NBSAs

The increases in FCG rates at lower loading frequencies may be due to a strain rate sensitivity. At high frequency the dislocations have a shorter time period to glide to the crack front. Therefore, the dislocation velocity needs to be higher at 25 Hz than 0.25 Hz

loading frequency to achieve the same amount of deformation. This increase in dislocation velocity may explain why the FCG rates decrease at higher frequency loading waveforms. Or in other words, higher strain rates lead to slower FCG rates (Figure 48, p77 to Figure 50, p79)

Strain rate sensitivity can occur due to the following mechanisms: i) creep [5], ii) strain induced martensitic transformation interactions, iii) deformation twinning, and iv) solute dislocation dragging [145]. Creep was previously discussed and found not to be active due to the 150 kJ/mol activation energy requirement and lack of intergranular fracture mode. Martensitic transformations do not occur in NBSAs to the knowledge of the author.

Twinning is observed in Haynes 282, see Figure 40, p57 (faint straight lines inside grains). Christian [55] discusses twinning phenomenon extensively, noting strain rate sensitivity is prevalent in BCC metals, but in FCC metals strain rate sensitivity is observed primarily at low temperatures. If twinning was the source of strain rate sensitivity, one would expect a noticeable rise in twinning on fracture surfaces or in microstructure. No such fine twinning is observed from the fracture surfaces (Figure 53, p84 and Figure 54, p85) or in the microstructure (Figure 60, p91); therefore, strain rate sensitivity from twinning is discounted in Haynes 282.

Solute drag has been proposed as a strain hardening mechanism [80] [133] [146] [147] [148] [149] [150], as well as precipitation of carbides on dislocations [133] [151]. Sharghi-Moshtaghin and Asgari [152] showed the solute diffusion velocities of Co, Mo, and Cr in Ni are much slower than dislocation velocities and since twinning did not occur in IN738, pipe diffusion of interstitials was the concluded cause of strain rate sensitivity for IN738 under tensile tests. Sharghi-Moshtaghin and Asgari [152] attributed an activation energy of 67-83 KJ/mol for interstitial element dragging of dislocations in IN738. This interstitial diffusion mechanism was first proposed by Hayes and Hayes [146] to explain observed serrated flow in tensile tests in Waspaloy.

To explain the observed serrated flow in Waspaloy at high temperatures and low strain rates, Hayes and Hayes [146] proposed a mechanism which involves dislocations capturing carbon, slowing down, depositing carbon at gamma prime, then bypassing gamma prime by Orowan mechanism as illustrated in Figure 70 below. At low temperatures or high strain rates there was not enough energy or time for carbon diffusion, hence the stress-strain curve breaks into serrations.

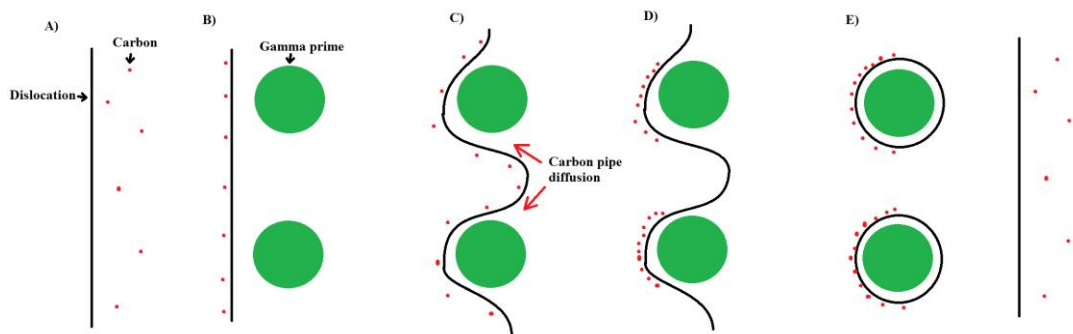


Figure 70 - Hayes and Hayes's proposed model for serrated flow, A) Dislocation glides as normal, B) Dislocation has picked up carbon, C) Dislocation bows around gamma prime, D) Carbon pipe diffuses and is captured by gamma prime, E) Dislocation bypasses gamma prime by Orowan mechanism, leaving carbon at gamma prime and dislocation is free to glide as normal.

Hayes and Hayes tested stress-strain curves for Waspaloy from 204°C to 649°C, at strain rates from 8.3×10^{-5} to $3.7 \times 10^{-2} \text{ s}^{-1}$. The activation energy for the carbon diffusion was found to be 66 kJ/mol. The activation energy for the $\text{Ni}_3\text{Al-C}$ reaction was measured at 132 kJ/mol.

Similar results were found in In738LC. Sharghi-Moshtaghin and Asgari [152] tested stress-strain curves for IN738 at strain rates from 8.7×10^{-5} to $4.3 \times 10^{-2} \text{ s}^{-1}$ at temperatures from 250°C to 550°C. Measured activation energy was also 67 kJ/mol to 83 kJ/mol.

See Table 13 for the author's estimated strain rates at various estimated strains in the C(T) sample.

strain	strain rate 25 Hz	strain rate 0.25 Hz
0.002	1.00E-01	1.00E-03
0.003	1.50E-01	1.50E-03
0.005	2.50E-01	2.50E-03
0.010	5.00E-01	5.00E-03
0.020	1.00E+00	1.00E-02
0.050	2.50E+00	2.50E-02

Table 13 - Strain rates for various levels of strain estimated in the C(T) sample.

At 0.25 Hz loading frequency the strain rate is near that tested by Hayes and Hayes; it is possible that at 25 Hz loading frequency carbon does not have adequate time to diffuse down the dislocation and deposit at or react with the gamma prime. This may slow dislocation motion at 25 Hz loading frequency and subsequently slow the FCG curves.

The author measured an activation energy peaking around 50 kJ/mol, which is just under the amount measured for Waspaloy and IN738LC. Haynes 282 is alloyed with carbon at 0.06 % weight. Waspaloy and IN738LC are reported to have 0.05 and 0.11 % weight of carbon respectively. Haynes 282 has a low volume fraction of gamma prime, slightly lower than Waspaloy, while IN738LC has a higher volume fraction, at about 45%. IN738LC also has a duplex gamma prime structure with 15% as primary cubical gamma prime and 30% as small secondary spherical gamma prime.

With similar carbon contents between Waspaloy and Haynes 282 and similar strain rates between both experiments, it is possible that at the higher frequency of 25 Hz strain aging effects could be taking place. However, stress-strain plots are monotonically loaded, and fatigue tests are cyclically loaded. This means that the strain rate will reverse and should allow some time for diffusion as the load is relaxed.

However, direct evidence was not found for this mechanism. Should the strain controlled stress-strain plots show serrated flow in Haynes 282, the interstitial solute dragging mechanism may explain some of slower fatigue response at higher loading frequencies.

Also problematic is how carbon is absorbed onto the dislocations. The initial heat treated microstructure (Figure 58, p89) is relatively dislocation free. Carbon may diffuse and

absorb onto the initial dislocations. However as the material is cyclically loaded dislocations will glide and multiply. It is rather unlikely that carbon would diffuse onto a glissile dislocation. The diffusion of interstitial elements through the gamma matrix, such as boron [153] and carbon [91], are 166 and 144 KJ/mol respectively.

Koul and Pickering [154] have shown the diffusion of carbon is faster than dislocation motion, which may support this carbon atmosphere theory. There is argument in the literature if carbon is the active element or if it is another interstitial element.

6.4.4 Summary of time dependence on FCG rates

Regardless of the active cracking mechanism, the crack is constantly looking to propagate on the lowest energy path available. For some unknown reason at 750°C some of the crack's lowest energy path was along grain boundaries in isolated cases. This may be due to localized creep or local chemistry changes in the grain boundaries. Whatever mechanism is responsible for the isolated intergranular features, there is not enough energy to sustain the crack path. Further investigation into why the alternate crack path was arrested would be useful. The author would suggest hold time experiments at 750°C to see if an intergranular crack path can be achieved. The author would also suggest a more detailed chemical analysis of grain boundaries which failed to see if there was inhomogeneity in the material.

Strain rate sensitivity may also play a role in deformation of Haynes 282. Serrated flow was observed in both Waspaloy and IN738. Strain rate sensitivity was suggested to explain frequency effects on FCG by Buckson and Ojo [100]. The author would suggest investigating strain rate controlled stress-strain experiments to verify serrated flow as an active mechanism experienced in Haynes 282.

6.5 Cracking mechanism transition

Fracture surfaces from Figure 53, p84 and Figure 54, p85 show a change from stage one to stage two crack growth. This mechanism change was observed around ΔK of 14 MPa \sqrt{m} for temperatures 650°C and below, while the shift from stage one to stage two happened

at a higher ΔK of 20 MPa \sqrt{m} at 750°C for both 25 Hz and 0.25 Hz loading frequency. Note the transition from stage one to stage two crack growth mechanism had no effect on FCG rates at either loading frequency (Figure 46, p75 and Figure 47, p76).

There are two major theories explaining the transition from stage one to stage two crack growth in polycrystals. The first explanation is that the plastic zone size spans multiple grains, activating duplex slip. The second explanation is that in precipitate strengthened materials, the dislocation motion transitions from a shearing to a Orowan looping mechanism. The following sections will cover these transition theories in more detail.

6.5.1 Duplex slip transition

The transition from stage one to stage two crack growth is theorized to occur due to the plastic zone in front of the crack tip encompassing multiple grains [5]. When the plastic zone ahead of the crack tip is smaller than the grain size, single shear slip is promoted as observed in Figure 53, p84 and Figure 54, p85. Alternatively, when the plastic zone encompasses multiple grains multiple oriented slip systems will be activated. Due to plastic constraint, dislocation slip in the active grain will induce dislocation slip in the adjacent grain; hence, the duplex slip.

While each individual grain has a different cross sectional area, largest from Figure 40, p57 appears to be around 250 μm . Stage one crack growth is observed in Figure 54H, p85 at 750°C at ΔK of 19 MPa \sqrt{m} . The plastic zone size under these conditions is 300 μm , just slightly larger than the largest grain in Figure 40, p57. At lower temperatures the transition from stage one to stage two occurred at ΔK of 14 MPa \sqrt{m} , which gives a plastic zone size of 150 μm . With an average grain size of ASTM 4 or $\sim 91 \mu m$ it would appear the transition from stage one to stage two crack growth at lower temperatures occurs when the plastic zone is 1.6x average grain size, and at higher temperatures 3.3x average grain size.

More likely the delay in stage one to stage two cracking mechanism is due to the decreased dislocation density observed at higher temperatures. At both 25 Hz and 0.25 Hz loading frequency (Figure 60, p91) dislocation density is observed to decrease with

increasing temperature. When dislocation density is lower, there is less probability for a glissile dislocation to interact with random sessile dislocation. Recall, sections 1.2.2 Interactions of dislocations in FCC materials, p11 and Reprinted from Hull, Bacon with permission of Elsevier publishing.

1.3.2 Cross slip of NBSAs, p19, screw dislocations can act to impede dislocation glide by the jog or Lomer-Cottrell lock. Once a dislocation is locked, further dislocations must cross slip or climb around the obstacle, promoting duplex slip. At higher temperatures where dislocation density is lower, there are less obstacles to encounter and less probability for cross slip or Lomer-Cottrell lock formation, even across grain boundaries. This will promote a single shear system, which promotes stage one crack growth.

6.5.2 Looping transition

A second way fatigue is shifted from stage one to stage two is when precipitate dislocation interaction shifts from shearing to Orowan bypass [5]. Recall the shift to stage two crack growth occurred at ΔK of $14 \text{ MPa}\sqrt{\text{m}}$ for temperatures 650°C and below, while the shift from stage one to stage two happened at a higher ΔK of $20 \text{ MPa}\sqrt{\text{m}}$ at 750°C for both 25 Hz and 0.25 Hz loading frequency. Because this shift happened at the same stress intensity ranges regardless of frequency comparing the microstructures at these different frequencies for a mechanism transition from stage one to stage two crack growth is valid.

The microstructure at 25 Hz loading frequency (Figure 60A-C, p91) represents stage one crack growth, with $\Delta K = 9 \text{ MPa}\sqrt{\text{m}}$, well below the transition. The microstructure at 0.25 Hz loading frequency (Figure 60D-E, p91) is representative of the onset of stage two cracking for temperatures 650°C and below and stage one for 750°C .

Reviewing the microstructure at 25 Hz loading frequency (Figure 60A-C, p91) at 650°C and below, shows very dense highly tangled dislocation structures while at 750°C the dislocation structure is lower density, with shear bands present. At 750°C gamma prime appears intact with no evidence of shearing (Figure 61, p92). The microstructure for 25

Hz loading waveform was cracked at a ΔK was $\sim 9 \text{ MPa}\sqrt{\text{m}}$; therefore, this microstructure represents stage one cracking mechanism.

The paired dislocation at 750°C (Figure 60C, p91) where the leading dislocation appears to bow around a precipitate would suggest a partial dislocation shearing through gamma prime, which is contrary to the unsheared gamma prime present in Figure 61, p92. It is possible the author is misinterpreting two dislocations projected on top of each other, which may be likely as the feature pointed to in Figure 60C, p91 seems to be an isolated example, see enhanced and circled feature in

Figure 71B.

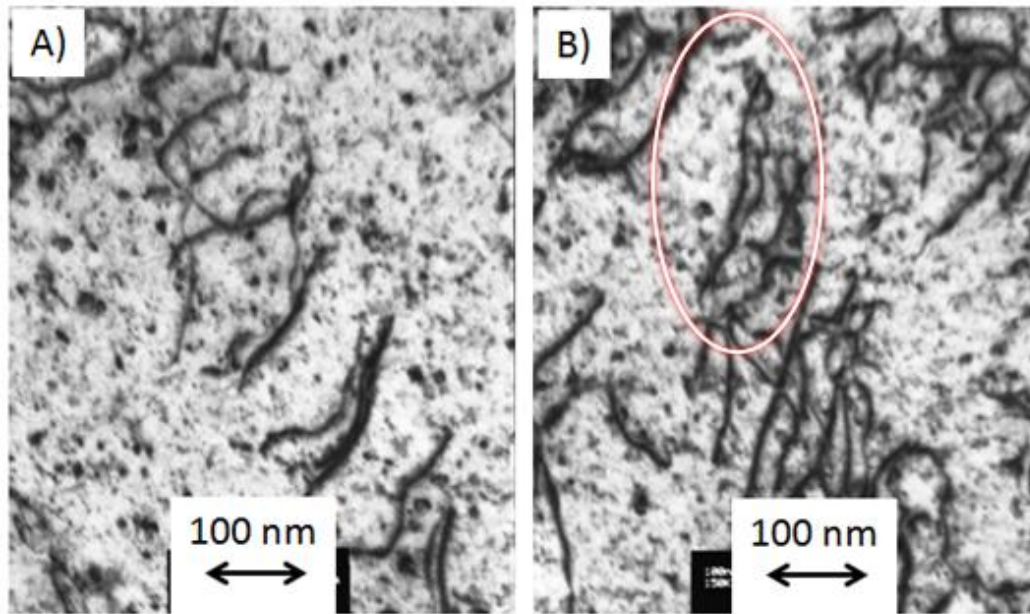


Figure 71 - Dislocation shear bands at from the microstructure at 750°C , 25 Hz. A) showing a typical shear band, B) zoomed in from Figure 60F, p91. Potential partial dislocation pair in question is circled.

Should the gamma prime undergo shearing at 25 hz loading frequency, the likely explanation for this contradiction is that not enough gamma prime was imaged. With lower density dislocation bands at 750°C , a larger area would need to be surveyed to observed gamma prime shearing. Unfortunately the gamma prime precipitates were hard

to image in the TEM, as a reflection axis was not readily found. More images of gamma prime are required to form a conclusion about their deformation.

Comparing the fractography and microstructure at 0.25 Hz (Figure 54, p85 and Figure 60D-E, p91) the microstructure shows dense tangles at 550°C, looping and shearing of precipitates at 650°C and significantly lower dislocation density at 750°C with only dislocations looping what is assumed to be precipitates. The microstructure for 0.25 Hz loading waveform was cracked at a $\Delta K \sim 15 \text{ MPa}\sqrt{\text{m}}$. Therefore, the microstructure for 650°C and below represents the onset of stage two crack growth (transition was at a ΔK of $\sim 14 \text{ MPa}\sqrt{\text{m}}$) and the microstructure at 750°C still represents stage one crack growth mechanism.

One possible explanation for the concurrent looping and shearing behavior of the dislocations observed is that the samples were grown close to the stress intensity range where the cracking mechanism transitions from stage one to stage two. Therefore, one would expect reminiscence of stage one to persist.

There are two reasons known to the author why dislocations would loop around precipitates. Firstly, there is a minimum stress or size required for a dislocation to bow around a precipitate. Secondly Lomer-Cottrell complex locks and the Kear-Winsdolf locks may form in the gamma prime, with the effect of arresting dislocation motion in gamma prime precipitates. The arresting of dislocation motion in gamma prime precipitates would force a dislocation pileup at the precipitate interface until enough stress has been reached to bow the dislocation around the precipitate. Locking and impeding dislocation glide should slow the FCG rates, which is contrary to observations.

Also the microstructure at 750°C shows dislocation shear (Figure 60C, p91) and dislocation looping (Figure 60E, p91) at stress intensity ranges below the stage one to stage two transition. This leaves the author to conclude that dislocation deformation transition from shear to looping has nothing to do with the stage one to stage two crack growth transition. This is congruent with observations in other NBSAs, where the

dislocation interactions with precipitates depended on precipitate size and applied stress as noted by Pineau and Antolovich [9].

7. Conclusion

This dissertation has evaluated the fatigue crack growth rates of Haynes 282. The test methodology followed ASTM E647, "Standard test method for measurement of fatigue crack growth rates." Temperatures investigated were 550°C, 650°C and 750°C. The loading frequencies were 0.25 and 25 Hz. In general, the effect of temperature on fatigue crack growth rates was to increase the crack growth rate as temperature increased.

Thermally activated cross-slip and dislocation annihilation were the primary mechanisms responsible for the increased fatigue crack growth rate. The noted activation energy for dislocation jog migration, which is related to dislocation annihilation, was about 12.5 kJ/mol. This value fit with the measured activation energy. The post-test microstructure showed greatly reduced dislocation density at the highest temperature. Fractography of the crack growth region showed transgranular crack growth at 550°C and 650°C with signs of isolated intergranular features at 750°C.

The effect of frequency on the fatigue crack growth rates was minor at 550°C. However, frequency effect was more prominent at 650°C and 750°C. For the temperatures investigated the effect of lowering the loading frequency was to increase in the fatigue crack growth rates. At high loading frequency, the isolated intergranular features were present only at stress intensity ranges below 11 MPa√m. At low loading frequency, the isolated intergranular features persisted through to higher stress intensity ranges.

While the isolated appearance of intergranular features in the post-test crack growth region is of some concern, the measured activation energy was well below creep and / or oxidation activation energies. This means that the growing crack did not have enough energy to sustain the intergranular aspects of crack propagation.

Fractography also revealed a transition from stage one to stage two cracking mechanism for a stress intensity of ~14 MPa√m at 550 and 650°C, independent of loading frequency. For 750°C, this cracking mechanism transition occurred at a stress intensity of ~19 MPa√m and was also independent of loading frequency. Investigations into the

microstructure at 750°C revealed that the dislocation density was significantly less than at the lower temperatures. Lower dislocation density at high temperature is determined to be causal in the delay of stage one to stage two crack growth mechanism.

Relative to other studies that have looked at the fatigue crack growth rates of Haynes 282, the author's data was in agreement at lower frequencies but disagreed somewhat at higher frequencies. It was determined that different microstructures caused this discrepancy.

Relative to other nickel-base superalloys intended for use as rotors, the fatigue crack growth rates of Haynes 282 is slower than Waspaloy and on par with Udimet 720 at high loading frequency (i.e., > 5 Hz). At lower loading frequencies (i.e., < 0.33 Hz) the fatigue crack growth rate of Haynes 282 is slightly higher than Inconel 718, but lower than that of either Waspaloy or Udimet 720. It should be noted that Inconel 718 has an effective upper use temperature limit of between 650°C and 700°C due to creep constraints, while Udimet 720 has been shown to have inadequate creep strength at 760°C.

Measured activation energy for Haynes 282 peaked around 50 kJ/mol for both loading frequencies. For these loading frequencies, the activation energy decreased with increasing stress intensity. Statistical analysis showed this trend to be significant. The activation energy for Haynes 282 relative to other nickel based superalloys was found to be lower than Udimet 720LI (i.e., low interstitial content) and RR1000 tested in air at 0.25 Hz.

In summary, the work discussed in this dissertation investigated the fine details of fatigue crack growth of Haynes 282. This study has closed some of the existing gap in the literature regarding the fatigue crack growth rates of Haynes 282. Previous studies have shown no adverse effects during low cycle fatigue and creep for Haynes 282 at temperature up to and including 760°C. This study has shown no adverse effects in the fatigue crack growth of Haynes 282 up to 650°C. However, some isolated indications of intergranular crack propagation within the crack growth region were observed at 750°C. These isolated regions were observed to arrest, or to revert back to transgranular crack

propagation. This mechanistic aspect, i.e., change back to transgranular crack propagation, is a promising result.

While not investigated in this work, strain rate sensitivity may influence deformation in Haynes 282. Serrated flow in the tensile stress-strain curve has been observed in both Waspaloy and IN738 (both high volume fraction gamma prime strengthened nickel superalloys). Strain rate sensitivity was suggested as one explanation for frequency effects in studies on fatigue crack growth in these alloys and by other authors investigating the fatigue crack growth rates of Haynes 282. While not a significant effect, the author would suggest further studies on the effects of strain rate on deformation in Haynes 282. In particular, it would be useful to better understand the strain rate sensitivity of Haynes 282 as a function of temperature and to correlate any effects with microstructural changes due to the different testing conditions.

In moving forward with Haynes 282 as a rotor alloy, it is important to understand the isolated intergranular features of crack propagation at 750°C. Regardless of the active cracking mechanism, the crack is constantly looking to propagate on the lowest energy path available. For some yet unidentified reason, a portion of the propagating crack's lowest energy path at 750°C was along the grain boundaries or just adjacent to the boundary. This may be due to local chemistry changes at or adjacent to the grain boundaries or the nature and morphology of carbides along the affected boundaries. Whatever mechanism is responsible for the isolated intergranular features, there is not enough energy to sustain the growing crack in this manner as shown by the measured activation energy. Further investigation into why the alternate crack path was initiated and arrested would be beneficial to the understanding the long-term stability of Haynes 282.

Also, important to understand is the possible effect of hold time. Activation energy significantly increased in other nickel-base superalloys with the introduction of a 20 second hold time at peak load (i.e., highest tensile stress). Intergranular crack growth has also been observed with the introduction of a 20 second hold time in Udimet 720. The author would suggest further fatigue crack growth rate testing of Haynes 282 at 650°C

and 750°C but with 20 and 200 second hold times to see if the aspects of crack propagation will transition into an intergranular mode. While other authors have seen no adverse effects of creep for Haynes 282 at 760°C exceeding 16,000 hours, it is important to more fully understand this effect given the long-term life requirement of a steam turbine rotor. Waspaloy has shown synergistic effects of creep and fatigue, with gamma prime undergoing unexpected accelerated growth. Identifying any mechanical instability or change in mechanism is critical to understanding the potential of this alloy for use in fossil energy applications.

The author would also suggest a more detailed post-test analysis of the crack growth region, including visual identification and chemical analyses of affected and unaffected grain boundaries that showed indications of intergranular crack propagation. Should it be possible to identify features within the microstructure that correlate with changes in crack propagation mechanism, it may be possible to alter the manufacturing process to correct this.

Finally, it would also be beneficial to test the fatigue crack growth rates of Haynes 282 up to 800°C at 0.25 and 25 Hz to see if intergranular aspects of crack propagation increase or if crack propagation transitions completely to an intergranular mode. Other authors have shown intergranular failure due to high strain creep testing at 815°C in Haynes 282. Additional testing of this nature would provide insight as to whether time or temperature or frequency is the primary culprit in the transition between transgranular and intergranular crack growth. If temperature is solely the cause of this transition, then the operating practice of the steam turbine can dictate the maximum operating temperature for Haynes 282. However, if creep-fatigue is the main or sole cause of this transition to intergranular crack propagation, then knowing more details about the temperature, frequency, critical hold time, number of cycles etc., for this to occur in Haynes 282 will result in better utilization of this alloy in fossil energy applications.

Designing an alloy for steam turbine rotor use in fossil energy applications is a complicated process. There are material property, manufacturing, and US legal code aspects needing to be addressed to develop rotor alloys. Previous research has addressed

the mechanical properties aspects of Haynes 282 in low cycle fatigue, creep and yield strength, showing no adverse effects. This project has investigated the fatigue crack growth properties of Haynes 282 and identified potential problems which need to be further investigated for alloy use at 760°C. Further issues include investigations of the corrodibility of Haynes 282 in the steam environment and potential synergistic interaction of creep and fatigue as shown in Waspaloy. Manufacturing aspects such as weldability of Haynes 282 to ferritic steels, casting and forging aspects should be addressed as well. Lastly ASME and US legal codes should be addressed.

Appendix I: Sample parameters

Presented below (Table 14-Table 20) is the parameters for each C(T) specimen. Reported are the initial and final crack lengths ('a'), the error associated with the crack length, the error associated with 'da/dN', the stress intensity ranges measured, and the sample temperature and standard deviation of the temperature.

Sample 24	Min	Max	Average	Standard Deviation
Measured 'a' [mm]	13.74	20.35	-	-
Calculated 'a' [mm]	13.74	20.41	-	-
Error 'a'	-	0.29%	-	-
Error 'da/dN'	-	4.70%	0.70%	-
ΔK [Mpa/m]	12.5	40	-	-
Temperature [°C]	-	-	750	0.7

Table 14 - Parameters for sample 24, measured at 750°C and 0.25 Hz.

Sample 20	Min	Max	Average	Standard Deviation
Measured 'a' [mm]	13.64	20.79	-	-
Calculated 'a' [mm]	13.64	20.4	-	-
Error 'a'	-	-1.88%	-	-
Error 'da/dN'	-	2.60%	1.00%	-
ΔK [Mpa/m]	9	25	-	-
Temperature [°C]	-	-	744	3

Table 15 - Parameters for sample 20, measured at 750°C and 25 Hz.

Sample 13	Min	Max	Average	Standard Deviation
Measured 'a' [mm]	12.33	20.77	-	-
Calculated 'a' [mm]	12.33	19.19	-	-
Error 'a'	-	-7.61%	-	-
Error 'da/dN'	-	3.10%	1.40%	-
ΔK [Mpa \sqrt{m}]	10.6	30	-	-
Temperature [°C]	-	-	644	1.6

Table 16 - Parameters for sample 13, measured at 650°C and 0.25 Hz.

Sample 11	Min	Max	Average	Standard Deviation
Measured 'a' [mm]	16.89	21.18	-	-
Calculated 'a' [mm]	16.89	21.52	-	-
Error 'a'	-	1.58%	-	-
Error 'da/dN'	-	3.00%	1.00%	-
ΔK [Mpa \sqrt{m}]	30	37	-	-
Temperature [°C]	-	-	657	2.6

Table 17 - Parameters for sample 11, measured at 650°C and 0.25 Hz.

Sample 11	Min	Max	Average	Standard Deviation
Measured 'a' [mm]	8.44	16.89	-	-
Calculated 'a' [mm]	8.44	17.8	-	-
Error 'a'	-	5.11%	-	-
Error 'da/dN'	-	3.00%	1.70%	-
ΔK [Mpa \sqrt{m}]	9	25	-	-
Temperature [°C]	-	-	648	0.9

Table 18 - Parameters for sample 11, measured at 650°C and 25 Hz.

Sample 14	Min	Max	Average	Standard Deviation
Measured 'a' [mm]	9.76	17.89	-	-
Calculated 'a' [mm]	9.76	17.81	-	-
Error 'a'	-	-0.45%	-	-
Error 'da/dN'	-	3.10%	1.00%	-
ΔK [Mpa \sqrt{m}]	13.7	38	-	-
Temperature [°C]	-	-	556	0.9

Table 19 - Parameters for sample 14, measured at 550°C and 0.25 Hz.

Sample 12	Min	Max	Average	Standard Deviation
Measured 'a' [mm]	8.9	18.5	-	-
Calculated 'a' [mm]	8.9	17.5	-	-
Error 'a'	-	-5.41%	-	-
Error 'da/dN'	-	2.50%	1.30%	-
ΔK [Mpa \sqrt{m}]	9	30	-	-
Temperature [°C]	-	-	550	0.8

Table 20 - Parameters for sample 12, measured at 550°C and 25 Hz.

Appendix II: Fracture surfaces at 0.05 Hz loading frequency

As noted in

Appendix I: Sample parameters, p130 FCG tests were concluded at a final crack length between 18 and 21 mm. The author was left with a sample which had 3 to 5 mm of crack plane left uncracked. To crack the samples in half for SEM investigation the author choose to crack some samples at constant load with an initial ΔK of $30 \text{ MPa}\sqrt{\text{m}}$ at a triangular waveform at 0.05 Hz until fracture. However, the author's custom crack length to voltage relation is not valid past 22 mm; therefore, FCG rates were not plotted. The intention of this final cracking procedure was to investigate if a lower frequency could produce a mixed or intergranular fracture surface. Shown below in Figure 72 is the fracture surfaces at 0.05 Hz. Note the stress intensity ranges are "relative" as the author's α to V relation is invalid at crack length for this experiment. Also the load ratio was set to 0.1; however, the computer had trouble maintaining $R = 0.1$. The resultant fracture surfaces show mostly transgranular crack growth for 650°C , while 750°C show secondary cracking is biased towards grain boundaries at 750°C .

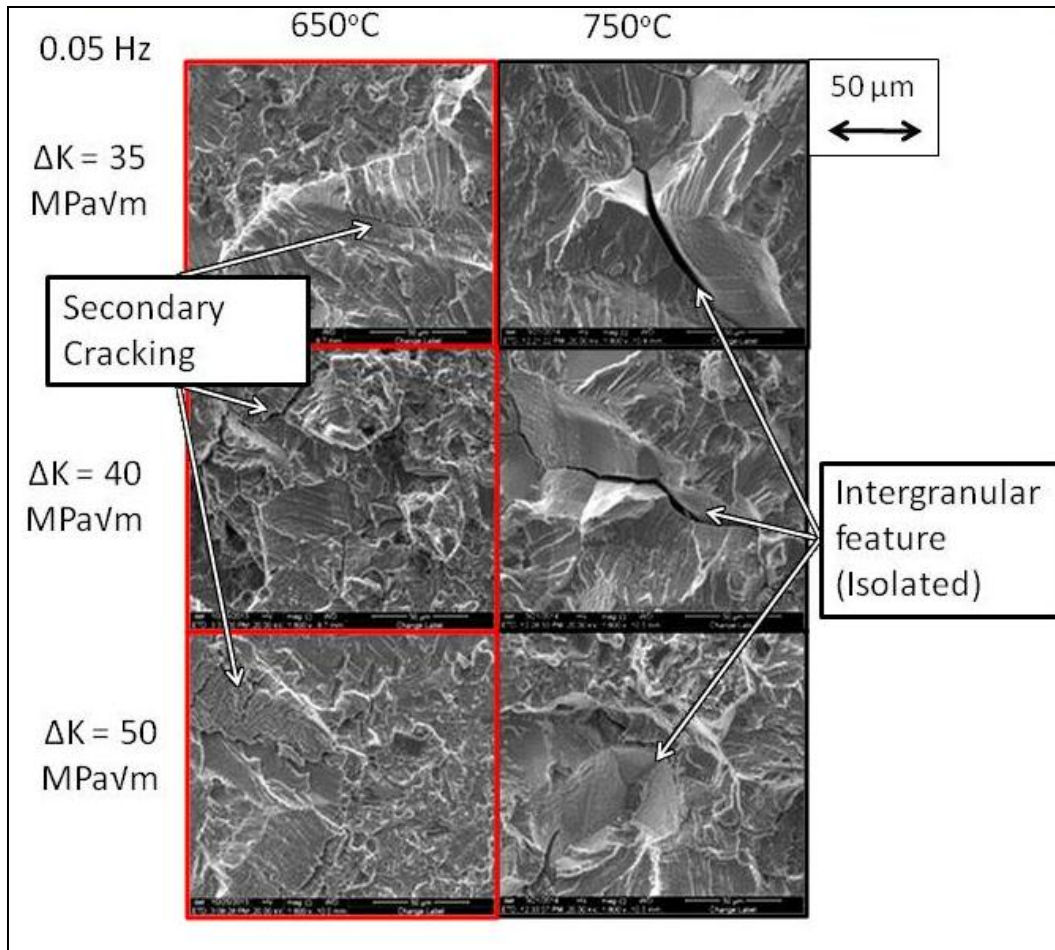


Figure 72- Fracture surfaces at 0.05 Hz with triangular waveform, R=0.1. Approximate stress intensity levels.

Works Cited

- [1] Viswanathan, Henry and e. al., "U.S. program on materials technology for ultra-supercritical coal power plants," *Journal of Materials Engineering and Performance*, vol. 14, no. 3, pp. 281-292, 2005.
- [2] "<http://www.netl.doe.gov/technologies/coalpower/advresearch/>," [Online]. [Accessed 15 Dec 2011].
- [3] Jablonski, Hawk, Cowen and e. al., "Processing of advanced cast alloys for A-USC steam turbine applications," *Journal of materials*, vol. 64, no. 2, p. 217, 2012.
- [4] Pike, "Haynes 282 Alloy - A new wrought superalloy designed for improved creep strenght and fabricability," in *ASME Turbo Expo*, Barcelona, Spain, 2006.
- [5] Suresh, *Fatigue of Materials*, Cambridge, New York: Cambridge university press, 2004.
- [6] Everitt and Jiang, "Comparison of fatigue crack propagation behavior in two gas turbine disc alloys under creep-fatigue conditions: evaluating microstructure, environment and temperature effects," *Materials Science and Technology*, vol. 29, no. 7, p. 781, 2013.
- [7] Adair and Johnson, "Identification of fatigue crack growth mechanism in IN100 Superalloy as a fuction of temperature and frequency," *Fatigue and Fracture of Engineering Materials & Structures*, vol. 36, p. 217, 2012.
- [8] Onofrio and Osinkolu, "Fatigue crack growth of Udimet 720 Li superalloy at elevated temperature," *International Journal of Fatigue*, vol. 23, p. 887, 2001.

- [9] Pineau, "High temperature fatigue of nickel-base superalloys - a review with special emphasis on deformation modes and oxidation," *Engineering failure analysis*, vol. 16, p. 2668, 2009.
- [10] Xiao and Chen, "Effect of boron on fatigue crack growth behavior in superalloy In 718 at RT and 650C," *Materials Science and Engineering: A*, vol. 428, p. 1, 2006.
- [11] Sun and Gao, "Effects of phosphorus on the delta Ni₃Nb phase precipitation and stress rupture properties in alloy 718," *Materials Science and Engineering: A*, vol. 247, p. 173, 1998.
- [12] S. H. Sims, *Superalloys 2*, New York: Wiley and Sons, 1987.
- [13] B. Hull, *Introduction to dislocations*, Burlington, Ma: Elsevier Butterworth-Heinemann, 2005.
- [14] Reed, *The superalloys fundamentals and applications*, Cambridge, NY: Cambridge university press, 2006.
- [15] Kent, "Mechanical properties and structural characteristics of NASA IIB," Cleveland OH, 1970.
- [16] Clark and Iwanski, "Institute of metals division - phase changes in precipitation hardening nickel-chromium-iron alloys during prolonged heating," *Transactions of the AIME*, vol. 215, p. 648, 1960.
- [17] Ross, "Recent research on IN-100," in *AIME annual meeting*, Dallas, Tx, 1963.
- [18] Ross, "Rene 100: a sigma-free turbine blade alloy," *Journal of metals*, vol. 19, no. 12, p. 12, 1967.
- [19] Dreshfield and Ashbrook, "TND-5185," NASA, April, 1969.

- [20] Dreshfield and Ashbrook, "TND-6015," NASA, September 1970.
- [21] Morral, *Superalloys source book*, Metals Park, OH: ASM, 1984.
- [22] Fox, "The structure of M-252 after exposure for 1,000,000 hours," in *AIME annual meeting*, Cleavland, OH, 1970.
- [23] B. Brooks, "Metallurgical stability of IN718," in *Superalloys*, Warrendale, PA, The metallurgical society, 1988, pp. 33-42.
- [24] Cozar and Pineau, "Morphology of gamma prime and gamma double prime precipitates and thermal stability of IN718 type alloys," *Metallurgical transactions*, vol. 4, p. 47, 1973.
- [25] Basinski, Korbel and Basinski, "The temperature dependence of the saturation stress and dislocation structure in fatigued copper single crystals," *Acta Metallurgica*, vol. 28, pp. 191-207, 1980.
- [26] Ackerman, Kubin and e. al., "The dependence of dislocation microstructure on plastic strain amplitude in cyclically strained copper single crystals," *Acta Metallurgica*, vol. 32, pp. 715-725, 1984.
- [27] Bonneville and Escaig, "Cross-slipping process and the Stress-orientation dependence in pure copper," *Acta Metallurgica*, vol. 27, pp. 1477-1486, 1979.
- [28] Pueschl, "Models for dislocation cross-slip in close-packed crystal structures: a critical review," *Progress in materials science*, vol. 47, pp. 415-461, 2002.
- [29] Escaig, "Sur le glissement dévié des dislocations dans la structure cubique à faces centrées," *Journal de physique*, vol. 29, pp. 255-239, 1968.
- [30] Paidar, Pope and Vitek, "A theory of the anomalous yield behavior in L12 ordered

- alloys," *acta metallurgica*, vol. 32, no. 3, pp. 435-448, 1984.
- [31] Rasmussen, Jacobsen and e. al., "Atomistic Determination of Cross-Slip Pathway and Energetics," *Physical Review Letters*, vol. 79, no. 19, p. 3676, 1997.
- [32] Rasmussen, Jacobsen and e. al., "Simulations of the atomic structure, energetics, and cross slip of screw dislocations in copper," *PHYSICAL REVIEW B*, vol. 56, no. 5, p. 2977, 1997.
- [33] Rao and Parthasarathy, "Atomistic simulation of cross-slip processes in model FCC structures," *Philosophical magazine A*, vol. 79, no. 5, pp. 1167-1192, 1999.
- [34] Vegge, Rasmussen and e. al., "Atomistic simulations of cross-slip of jogged screw dislocations in copper," *Philosophical Magazine Letters*, vol. 81, no. 3, pp. 137-144, 2001.
- [35] Rao and Dimiduk, "Activated states for cross-slip at screw dislocation intersections in face-centered cubic nickel and copper via atomistic simulation," *Acta Materialia*, vol. 58, p. 5547, 2010.
- [36] Qi, Strachan and e. al., "Large scale atomistic simulation of screw dislocation structure, annihilation and cross slip in FCC ni," *Materials science and engineering A*, Vols. 309-310, pp. 156-159, 2001.
- [37] Qi, Ikeda and e. al., "Deformation Behavior of FCC Crystalline Metallic Nanowires Under High Strain Rates," *Materials Research Society Symposium Proceedings*, vol. 554, p. 367, 1998.
- [38] Sutton and Chen, "Long-range Finnis–Sinclair potentials," *Philosophical Magazine Letters*, vol. 61, no. 3, p. 139, 1990.
- [39] Rafii-Tabar and Sulton, "Long-range Finnis-Sinclair potentials for f.c.c. metallic

- alloys," *Philosophical Magazine Letters*, vol. 63, no. 4, pp. 217-224, 1991.
- [40] Paus, Kratochvil and Benes, "A dislocation dynamics analysis of the critical cross slip annihilation distance and the cyclic saturation stress in FCC single crystals at different temperatures," *Acta materialia*, vol. 61, pp. 7917-7923, 2013.
- [41] Brown, "A dipole model for the cross-slip of screw dislocation in fcc metals," *Philosophical Magazine A*, vol. 82, no. 9, pp. 1691-1711, 2002.
- [42] Hirsch, "Extended jogs in dislocations in face-centered cubic metals," *Philosophical Magazine*, vol. 7, no. 73, pp. 67-93, 1962.
- [43] Suzuki and Barrett, "Deformation twinning in silver-gold alloys," *Acta Metallurgica*, vol. 6, no. 3, pp. 156-165, 1958.
- [44] Haasen, "Plastic deformation of nickel single crystals at low temperatures," *Philosophical Magazine*, vol. 3, no. 28, p. 384, 1958.
- [45] Ookawa, "On the Mechanism of Deformation Twin in fcc Crystal," *Journal of the Physical society of japan*, vol. 12, no. 7, p. 825, 1957.
- [46] Chin, Hosford and Mendorf, "Accommodation of Constrained Deformation in f.c.c. Metals by Slip and Twinning," *Proceedings of the Royal Society A*, vol. 309, p. 433, 1969.
- [47] Venables, "Deformation twinning in face-centred cubic metals," *Philosophical Magazine*, vol. 6, no. 63, p. 379, 1961.
- [48] Cohen and Weertman, "Reply to comments on "A dislocation model for twinning in f.c.c. metals"," *Acta Metallurgica*, vol. 11, no. 12, p. 1368, 1963.
- [49] Mori and Fujita, "Dislocation reactions during deformation twinning in Cu-11at.%

- Al single crystals,” *Acta Metallurgica*, vol. 28, no. 6, p. 771, 1980.
- [50] Mahajan and Chin, “Formation of deformation twins in f.c.c. crystals,” *Acta Metallurgica*, vol. 21, no. 10, p. 1353, 1973.
- [51] Narita and Takamura, “Deformation twinning in silver-and copper-alloy crystals,” *Philosophical Magazine*, vol. 29, no. 5, p. 1001, 1974.
- [52] Viswanathan and Sarosi, "Investigation of creep deformation mechanisms at intermediate temperatures in Rene88DT," *Acta Materialia*, vol. 53, no. 10, p. 3041, 2005.
- [53] Hirth and Lothe, *Theory of dislocations*, New York, NY: Wiley, 1982.
- [54] Karthikeyan and Unocic, "Modeling microtwinning during creep in ni-based superalloys," *Scripta Materialia*, vol. 54, p. 1157, 2006.
- [55] Christian and Mahajan, "Deformation Twinning," *Progress in Materials Science*, vol. 39, pp. 1-157, 1995.
- [56] Kolbe, "The high temperature decrease of the critical resolved shear stress in nickel-base superalloys," *Materials Science and Engineering: A*, Vols. 319-321, p. 383, 2001.
- [57] Xie and Yu, "The effects of crack orientation on the twin formation from the crack tip in gamma prime Ni₃Al," *Materials science and engineering A*, vol. 580, p. 99, 2013.
- [58] Anderson, *Fracture Mechanics*, Boca Raton, FL: CRC Press, 2005.
- [59] Paris and Erdogan, “A critical analysis of crack propagation laws,” *Journal of basic engineering*, vol. 85, p. 528, 1960.

- [60] G. Riemelmoser, "Dislocation modelling of fatigue cracks: an overview," *Materials Transactions*, vol. 42, no. 1, p. 2, 2001.
- [61] Z. Pippan, "On the mechanism of fatigue crack propagation in ductile metallic materials," *Fatigue and fracture of engineering materials and structures*, vol. 34, p. 1, 2010.
- [62] Williams and Starke, "Progress in structural materials for aerospace systems," *Acta materialia*, vol. 51, pp. 5774-5799, 2003.
- [63] Bowman, "The effect of microstructure on the fatigue crack growth resistance of nickel base superalloys," Georgia Tech, 1988.
- [64] Lawless and Antolovich, "The effect of microstructure on the fatigue crack propagation and overload behavior of Waspaloy at room temperature," in *Fracture: interactions of microstructures, mechanisms and mechanics*, Warrendale, Pa, AIME, 1985, p. 285.
- [65] Reed, "Fatigue crack growth mechanisms in superalloys: overview," *Materials science and technology*, vol. 25, no. 2, p. 258, 2009.
- [66] Krueger and Kissinger, "Development and introduction of a damage tolerant high temperature nickel base disk alloy, rene'88DT," in *Superalloys*, Cincinnati, OH, 1992.
- [67] Bussac and Antolovich, "The effects of microstructure and environment on the fatigue crack propagation behavior of a Ni-base alloy," in *9th international fatigue congress*, Atlanta, GA, 2006.
- [68] Bain, Gambone and e. al., "Development of damage tolerant microstructures in udimet 720," in *Superalloys*, Warrendale, Pa, 1988, pp. 13-22.

- [69] Locq, Caron and e. al, "On the role of tertiary gamma prime precipitates in the creep behavior at 700oC of a powder metallurgy disk super alloy," in *Superalloys*, Warrendale, Pa, 2004, pp. 179-188.
- [70] Merrick and Floreen, "The effects of microstructure on elevated temperature crack growth in nickel-base alloys," *Metallurgical Transactions A*, vol. 9, no. 2, p. 231, 1978.
- [71] Floreen, "Creep-fatigue-environmental interactions," in *TMS-AIME*, Warrendale, Pa, 1980.
- [72] Gayda, Miner and Gabb, "On the fatigue crack propagation behavior of superalloys at intermediate temperatures," in *TMS-AIME, Superalloys*, Warrendale, PA, 1984.
- [73] Lawless and Antolovich, "Fracture: interactions of microstructure, mechanisms and mechanics," in *TMS-AIME*, Warrendale, PA, 1984.
- [74] King, "Effects of grain size and microstructure on threshold values and near threshold crack growth in powder-formed Ni-base superalloy," *Metal Science*, vol. 16, no. 7, p. 345, 1982.
- [75] Nabarro and d. Villers, *Physics of Creep*, Bristol, Pa: Taylor and Francis Inc., 1995.
- [76] E. Findley, "A critical assessment of fatigue crack nucleation and growth models for ni- and ni,fe-based alloys," *International materials reviews*, vol. 56, no. 1, p. 49, 2011.
- [77] F. Larson, "Metallurgical factors affecting the crack growth resistance of a superalloy," *Metallurgical Transactions A*, vol. 8, no. 1, p. 51, 1977.
- [78] H. Y. C. Liu, "Superalloys 718, 625 and various derivatives," in *TMS*, Warrendale, Pa, 1991.

- [79] Xu and Wu, "An intergranular creep crack growth model based on grain boundary sliding," *Metallurgical and Materials Transactions A*, vol. 30, no. 4, p. 1039, 1999.
- [80] Wells and Sullivan, "The effect of temperature on low cycle fatigue behavior of Udimet 700," *Trans ASM*, vol. 60, pp. 217-222, 1967.
- [81] Gabb, Gayda and Miner, "Orientation and temperature dependence of some mechanical properties of the single-crystal nickel-base superalloy René N4: Part II. Low cycle fatigue behavior," *Metallurgical Transactions A*, vol. 17, no. 3, p. 497, 1986.
- [82] Coffin, "The effect of frequency on the cyclic strain and low cycle fatigue behavior of cast Udimet 500 at elevated temperature," *Metallurgical and Materials Transactions B*, vol. 2, no. 11, p. 3106, 1971.
- [83] Jaski, Rice and e. al., "CR-135022," NASA, 1976.
- [84] Frost and Ashby, *Deformation-Mechanism maps*, Oxford, England: Pergamon, 1982.
- [85] Molins and Hochstetter, "Oxidation effects on the fatigue crack growth behavior of alloy 718 at high temperature," *Acta Materialia*, vol. 45, p. 663, 1997.
- [86] Andrieu and Molins, "Intergranular crack tip oxidation mechanism in a nickel-based super alloy," *Materials Science and Engineering A*, vol. 154, no. 1, p. 21, 1992.
- [87] Pineau, "Mechanical behavior of materials at high temperatures," in *TMS*, New York, NY, 1996.
- [88] Woodford and Bricknell, *Treatise Mater. Sci. Technol*, vol. 25, p. 157, 1983.

- [89] Yuen and Roy, "Effect of oxidation kinetics on the near threshold fatigue crack growth behavior of a nickel base superalloy," *Metallurgical Transactions A*, vol. 15, no. 9, p. 1769, 1984.
- [90] S. Hunt, "Superalloys 2000," in *TMS*, Warrendale, PA, 2000.
- [91] Starink and Reed, "Thermal activation of fatigue crack growth: analysing the mechanism of fatigue crack propagation in superalloys," *Material science and engineering A*, vol. 491, pp. 279-289, 2008.
- [92] Yokobori and Aizawa, "The influence of temperature and stress intensity factor upon the striation spacing and fatigue crack propagation rate of aluminum alloy," *International Journal of Fracture*, vol. 9, no. 4, pp. 489-491, 1973.
- [93] Yokobori, Yokobori and Kamei, "Dislocation dynamics theory for fatigue crack growth," *International Journal of Fracture*, vol. 11, no. 5, pp. 781-788, 1975.
- [94] Yokobori and Konosu, in *4th Int. Conf. on 'Fracture'*, Waterloo, Ontario, 1978.
- [95] Xu, Dickson and Koul, "Grain growth and carbide precipitation in superalloy Udimet 520," *Metallurgical and materials transactions A*, vol. 29, pp. 2687-2695, 2998.
- [96] Fang, Ji and e. al., "Critical strain and models of dynamic recrystallization for FGH96 superalloy during two-pass hot deformation," *Materials Science and Engineering A*, vol. 593, pp. 8-15, 2014.
- [97] Hongyu, Lingli and e. al., "Coarsening behavior of gamma prime particles in a nickel-base superalloy," *Rare metals*, vol. 28, no. 2, pp. 197-201, 2009.
- [98] Lerch, "CR-165497," NASA, 1982.

- [99] Hull, *Fractography*, Cambridge, UK: Cambridge university press, 1999.
- [100] Buckson and Ojo, "Cyclic deformation characteristics and fatigue crack growth behavior of newly developed aerospace superalloy haynes 282," *Materials Science and Engineering A*, vol. 555, p. 63, 2012.
- [101] Pike, "Long term thermal exposure of Haynes 282 alloy," in *7th international symposium on superalloy 718 and derivatives*, TMS, 2010.
- [102] Pike, "Low-cycle fatigue behavior of haynes 282 alloy and other wrought gamma prime strengthened alloys," in *ASME turbo expo 2007: power for land, sea and air*, Montreal, CA, 2007.
- [103] Pike and Srivastava, "Oxidation behavior of wrought gamma-prime strengthened alloys," *Materials science forums*, Vols. 595-598, pp. 661-671, 2008.
- [104] Viswanathan, Hawk, Totemeir and e. al., "Steam turbine materials for ultrasupercritical coal power plants," US department of energy, Independence, OH, 2009.
- [105] Boehlert and Longanbach, "A comparison of the microstructure and creep behavior of cold rolled haynes 230 and haynes 282 alloy," *Materials science and engineering a*, vol. 528, pp. 4888-4898, 2011.
- [106] Evans and Wilshire, *Creep of metals and alloys*, 1st ed., New York, NY: The intitute of metals, 1985.
- [107] Crossman and Ashby, "The non-uniform flow of polycrystals by grain-boundary sliding accommodated by power-law creep," *Acta Metallurgica*, vol. 23, no. 4, p. 425, 1975.
- [108] A. s. E647, "Standard test method for measurment of fatigue crack growth rates,"

ASTM international, 2011.

- [109] Healy, Grabowski and Beevers, "Short-fatigue-crack growth in a nickel-base superalloy at room and elevated temperature," *International journal of fatigue*, vol. 13, no. 2, pp. 133-138, 1991.
- [110] Pang and Reed, "Fatigue crack initiation and short crack growth in nickel-base turbine disk alloys - the effects of microstructure and operating parameters," *International journal of fatigue*, vol. 25, pp. 1089-1099, 2003.
- [111] Taylor, *An introduction to error analysis*, Mill Valley, CA: University science books, 1982.
- [112] Lee, "Modeling of materials behavior at various temperatures of hot isostatically pressed superalloys," *Materials science and engineering A*, vol. 541, pp. 81-87, 2012.
- [113] Smith, Liu and Grabowski, "Short fatigue crack growth behavior in waspaloy at room and elevated temperatures," *Fatigue and fracture of engineering materials and structures*, vol. 19, no. 12, pp. 1505-1514, 1996.
- [114] Schoettle, Sinclair and e. al., "Deflected 'teardrop cracking' in nickel based superalloys: Sustained macroscopic deflected fatigue crack growth," *International journal of fatigue*, vol. 44, pp. 188-201, 2012.
- [115] Ghonem and Zheng, "Depth of intergranular oxygen diffusion during environmental-dependent fatigue crack growth in alloy 718," *Materials Science and Engineering: A*, vol. 18, pp. 1431-1439, 1992.
- [116] Liu, Kang and Chang, "The effect of hold-time on fatigue crack growth behaviors of Waspaloy at elevated temperature," *Materials science and engineering A*, vol. 340, pp. 8-14, 2003.

- [117] Maciejewski, Jouiad and Ghonem, "Dislocation/precipitate interactions in IN100 at 650C," *Materials science and engineering A*, vol. 582, pp. 47-54, 2013.
- [118] Hawk, Jablonski and Sears, "Microstructural evolution in Haynes 282 after high temperature creep exposure," in *TMS annual meeting and exhibition*, San Antonio, Texas, 2013.
- [119] Hide, Henderson and Reed, "Effects of grain and precipitate size variation on creep-fatigue behavior of udimet 720li in both air and vacuum," in *Proceedings of the 9th international symposium on superalloys*, Seven Springs, PA, 2000.
- [120] Tucker, Henderson, Wilkinson and e. al., "High temperature fatigue crack growth in powder processed nickel based superalloy u720li," *Materials science and technology*, vol. 18, pp. 349-353, 2002.
- [121] Hessel, Voice, James and e. al..Patent US Patent 5897718, 1999.
- [122] Reed, Wisbey, Everitt and e. al., in *7th international charles parsons turbine conference*, Glasgo, UK, 2008.
- [123] Pang and Reed, "Microstructure effects on high temperature fatigue crack initiation and short crack growth in turbine disc nickel-base superalloy Udimet 720Li," *Materials Science and Engineering: A*, vol. 448, no. 1-2, pp. 67-79, 2007.
- [124] Pang and Reed, "Microstructure variation and effect on room temperature fatigue threshold and crack propagation in udimet 720Li Ni-base superalloy," *Fatigue fracture and engineering of materials and structures*, vol. 32, pp. 685-701, 2009.
- [125] Chan, "Time-Dependent crack growth threshold of ni-based superalloys," *Metallurgical and materails trancactions A*, vol. 45, no. A, pp. 3454-3466, 2014.
- [126] Zener and Hollomon, "Effect of Strain Rate Upon Plastic Flow of Steel," *Journal*

of applied physics, vol. 15, no. 1, p. 22, 1944.

- [127] King, "Fatigue crack propagation in nickel-base superalloys – effects of microstructure, load ratio, and temperature," *Materials science and technology*, vol. 3, no. 9, p. 750, 1987.
- [128] Peraldi, Monceau and Pieraggi, "The nickel, model material for the high temperature oxidation studies: first steps towards predictive modelling," *Revue de Métallurgie*, vol. 102, no. 2, p. 136, 2005.
- [129] Gordon, Trexler, N. Jr., Sanders and e. al., "Corrosion kinetics of a directionally solidified Ni-base superalloy," *Acta Materialia*, vol. 55, no. 10, p. 3375, 2007.
- [130] Antolovich, Liu and Baur, "Low cycle fatigue behavior of René 80 at elevated temperature," *Metallurgical Transactions A*, vol. 12, no. 3, p. 473, 1981.
- [131] Lerch, "Das Raum-und hochtemperature-ermuedungsverhalten der nickelbasislegierung Nimonic 80A," University of Stuttgart, 1983, 1983.
- [132] Lerch and Gerold, "The low cycle fatigue properties of a gamma prime strengthened superalloy," in *Deformation of multi-phase and particle containing materials: proceedings of the 4th riso international symposium on metallurgy and materials science*, Roskilde, Denmark, Riso national labratory, 1983, pp. 375-80.
- [133] Lerch and Jayaraman, "A study of fatigue damage mechanisms in Waspaloy from 25 to 800C," *Materials Science and Engineering*, vol. 34, p. 275, 1978.
- [134] Lerch, "Microstructural effects on the room and elevated temperature low cycle fatigue behavior of Waspaloy," NASA CR-165497, 1982.
- [135] Antolovich and Liu, "Low cycle fatigue behavior of rene 80 at elevated temperature," *Metallurgical and Materials Transactions A*, vol. 12, p. 473, 1981.

- [136] Xie and Yu, "Motion mechanism of the edge dislocation slipping in the cubic plain of ni₃Al single crystals," *Modelling and simulation in materials science and engineering*, vol. 21, p. 1, 2013.
- [137] Rasmussen, Vegge and e. al., "Simulation of structure and annihilation of screw dislocation dipoles," *Philosophical Magazine A*, vol. 80, no. 5, pp. 1273-1290, 2000.
- [138] Leffers and Pedersen, "The activation energy for the FCC rolling texture transition and the activation energy for cross slip," Riso national laboratory, Roskilde, Denmark, 2002.
- [139] Tippelt, Breitschneider and Haehner, "The Dislocation Microstructure of Cyclically Deformed Nickel Single Crystals at Different Temperatures," *Physica status solidi (a)*, vol. 163, no. 1, pp. 11-26, 1997.
- [140] Weast, Handbook of chemistry and physics, 66th edition, Boca Raton, Fl: CRC press, 1985.
- [141] Sondhi, Dyson and McLean, "Tension–compression creep asymmetry in a turbine disc superalloy: roles of internal stress and thermal ageing," *Acta Materialia*, vol. 52, no. 7, pp. 1761-1772, 2004.
- [142] Swalin and Martin, "Solute diffusion in nickel-base substitutional solid solutions," *Journal of metals*, vol. 8, no. 5, p. 567, 1956.
- [143] Karaunaratne and Reed, "Interdiffusion of the platinum-group metals in nickel at elevated temperatures," *Acta Materialia*, vol. 51, no. 11, p. 2905, 2003.
- [144] Sondhi, Dyson and McLean, "Tension–compression creep asymmetry in a turbine disc superalloy: roles of internal stress and thermal ageing," *Acta Materialia*, vol. 52, no. 7, pp. 1761-1772, 2004.

- [145] Singh and Dohery, "Strengthening in MULTIPHASE(MP35N) alloy: Part II. elevated temperature tensile and creep deformation," *Metallurgical Transactions A*, vol. 23, no. 1, p. 321, 1992.
- [146] Hayes and Hayes, "On the mechanism of delayed discontinuous plastic flow in an age-hardened nickel alloy," *Acta Materialia*, vol. 30, p. 1295, 1982.
- [147] Lloyd and Chung, "Serrated yielding in a superalloy," *acta metallurgica*, vol. 23, p. 93, 1975.
- [148] Chung and Chaturvedi, "The characteristics of the barrier during serrated yielding in the gamma prime precipitation hardened superalloys," *Acta Materialia*, vol. 24, p. 227, 1976.
- [149] Bloom and Kocks, "Deformation behavior of 4 Mo alloys," *Acta Met*, vol. 33, p. 265, 1985.
- [150] Lall and Chin, "The orientation and temperature dependence of the yield stress of Ni₃Al single crystals," *Metallurgical and Materials Transactions A*, vol. 10, p. 1323, 1979.
- [151] Clavel and Levailant, "Influence of micromechanisms of cyclic deformation at elevated temperature on fatigue behavior," in *Creep Fatigue environment interactions*, Warrendale, AIME, 1980, pp. 24-45.
- [152] Sharghi-Moshtaghin and Asgari, "The characteristics of serrated flow in superalloy IN738LC," *Material Science and Engineering A*, vol. 486, p. 376, 2008.
- [153] Ramirez and Liu, "Diffusion Brazing in the Nickel-Boron System," *Supplement to the welding journal*, p. 365, October, 1992.
- [154] Koul and Pickering, "Serrated yielding in Ni₃Fe base superalloys at 700°C,"

Scripta Metallurgica, vol. 16, no. 2, pp. 119-124, 1982.

- [155] Proville and Bako, "Dislocation depinning from ordered nanophases in model FCC crystal: From cutting mechanism to Orowan looping," *Acta Materialia*, vol. 58, p. 5565, 2010.
- [156] Ramirez and Ghoniem, "Ab initio continuum model for the influence of local stress on cross slip of screw dislocations in FCC metals," *Physical Review B*, vol. 86, 2012.
- [157] Rao and Dimiduk, "Calculations of intersection cross slip activation energies in FCC metals using nudged elastic band method," *Acta Materialia*, vol. 59, p. 7135, 2011.
- [158] Kayacan, vol. 39, p. 2171, 2004.
- [159] O. Onofrio, "Fatigue crack growth of Udimet 720 Li superalloy at elevated temperature," *International journal of fatigue*, vol. 23, p. 887, 2001.
- [160] Riemelmsch and Gumbsch, "Dislocation modelling of fatigue cracks: an overview," *Materials transactions*, vol. 42, no. 1, p. 2, 2001.
- [161] Huang and Tong, "A study of fatigue crack tip characteristics using discrete dislocation dynamics," *International journal of plasticity*, vol. 54, p. 229, 2014.
- [162] Bressers and Roth, "Advances in life prediction methods," in *ASME*, New York, NY, 1983.
- [163] Bressers and Verheggen, "The effect of time-dependent processes on the high-temperature LCF life of Waspaloy," *Res Mech Lett*, vol. 1, p. 55, 1981.
- [164] McClintock, "Fatigue crack propagation," *ASTM-STP*, vol. 415, p. 70, 1963.

- [165] McClintock, "On the plasticity of growth of fatigue cracks," in *Fracture of solids*, New York, NY, Wiley, 1967, p. 65.
- [166] Antolovich and Saxena, "A model for fatigue crack propagation," *Eng Fract Mech*, vol. 7, p. 649, 1975.
- [167] Venables, in *Deformation Twinning*, New York, NY, Gordon and Breach, 1963, p. 77.
- [168] Reed and Jackson, "Characterisation and modelling of the precipitation of sigma phase in Udimet 720 and Udimet 720li," *Metallurgical and Materials Transactions A*, vol. 30, p. 521, 1999.
- [169] H. Mollins, "Oxidation effects on the fatigue crack growth behavior of alloy 718 at high temperature," *Acta Mater.*, vol. 45, no. 2, p. 663, 1997.
- [170] Kitagawa, *J. Jap. Soc. Mech. Engrs*, vol. 75, p. 1068, 1972.
- [171] Tanaka and Matsuoka, "A tentative explanation for tow parameters, C and m, in Paris; equation of fatigue crack growth," *Int. J. Fracture*, vol. 13, p. 563, 1977.
- [172] Yokobori and Maekawa, "Fatigue crack propagation of 25MN 5Cr 1Ni austenitic steel," *Fatigue at elevated temperature ASTM STP*, vol. 857, p. 121, 1985.
- [173] Reemsnyder, "Written discussion of: "Tobler, Cheng 'midrange fatigue crack growth data correlations for structural alloys at room and cryogenic temperature'", " *ASTM STP*, vol. 857, p. 3, 1985.
- [174] Cortie and Garret, "On the correlation between the C and m in paris equation for fatigue crack propagation," *Engng Fracture Mech.*, vol. 30, p. 49, 1988.
- [175] Lost, "Temperature dependence of stage II fatigue crack growth rate," *Engineering*

fracture mechanics, vol. 45, no. 6, p. 741, 1993.

- [176] Buckson and Ojo, "Cyclic deformation characteristics and fatigue crack growth behavior of newly developed aerospace superalloy haynes 282," *Materials Science and Engineering A*, vol. 555, p. 63, 2012.
- [177] Merrick, "The low cycle fatigue of three wrought nickel base superalloys," *Met Trans*, vol. 5, pp. 891-897, 1974.
- [178] Dalah, Maciejewski and Ghonem, "Loading frequency and microstructure interaction in intergranular fatigue crack growth in a disk Ni-based superalloy," *International journal of fatigue*, vol. 57, pp. 93-102, 2013.
- [179] Lynch, Radtke and e. al., "Fatigue crack growth in nickel-based superalloys at 500-700C. I: Waspaloy," *Fatigue and fracture of engineering materials and structures*, vol. 17, no. 3, pp. 297-311, 1994.
- [180] Yoon, Park and Saxena, "Elevated temperature fatigue crack growth model for DS-GTD-111," *Strength, Fracture and complexity*, vol. 4, pp. 35-40, 2006.
- [181] Cowles, Warren and Haake, "CR-165123," NASA, July 1980.
- [182] Gabb, Telesman, Kantozs and e. al., in *Superalloys*, warrendal, Pa, 2004.
- [183] Brown, "A dipole model for the cross-slip of screw dislocations in FCC metals," *Philosophical magazine A*, vol. 82, no. 9, pp. 1691-1711, 2002.
- [184] Rao, Dimiduk and e. al., "Atomistic simulations of intersection cross-slip nucleation in L12 Ni3Al," *Scripta materialia*, vol. 66, pp. 410-413, 2012.
- [185] Liu, "Microstructural defects in ferroelectrics and their scientific implications," in *Ferroelectrics - Characterization and modeling*, 2011.

- [186] Miner and Gayda, "Fatigue and creep-fatigue deformation of several nickel-base superalloys at 605C," *Metallurgical Transactions A*, vol. 13, p. 1775, 1982.
- [187] Mughrabi, Ackermann and Herz, "Persistent slip bands in fatigued FCC and BCC cubic metals," in *In Fatigue mechanisms, Special technical publications 675*, Philadelphia, PA, American society for testing and materials, 1979, pp. 69-105.
- [188] Read, *Dislocations in Crystals*, New York, NY: McGraw-Hill, 1953.
- [189] Zhong, Gu and e. al., "Fatigue crack growth behaviour of a newly developed Ni-Co-base superalloy TMW-2 at elevated temperatures," *Material science and engineering A*, vol. 552, pp. 464-471, 2012.
- [190] Venables, "On dislocation pole models for twinning," *Philosophical magazine*, vol. 30, no. 5, p. 1165, 1974.
- [191] Ross, "Rene 100: a sigma-free turbine blade alloy," *Journal of metals*, vol. 19, no. 12, p. 12, 1967.
- [192] Coffin, "The effect of frequency on the cyclic strain and low cycle fatigue behavior of cast Udimet 500," *Metallurgical and Materials Transactions*, vol. 2, p. 3105, 1971.
- [193] Kawazaki and Nakanishi, "Fracture toughness and fatigue crack propagation in high strength steel from room temperature to -180C," *Engineering Fracture Mechanics*, vol. 7, p. 465, 1975.